

2018

System Optimization and Material Development of Solid Oxide Cells for Energy Conversion and Storage

Libin Lei
University of South Carolina

Follow this and additional works at: <https://scholarcommons.sc.edu/etd>

 Part of the [Mechanical Engineering Commons](#)

Recommended Citation

Lei, L. (2018). *System Optimization and Material Development of Solid Oxide Cells for Energy Conversion and Storage*. (Doctoral dissertation). Retrieved from <https://scholarcommons.sc.edu/etd/4623>

This Open Access Dissertation is brought to you by Scholar Commons. It has been accepted for inclusion in Theses and Dissertations by an authorized administrator of Scholar Commons. For more information, please contact dillarda@mailbox.sc.edu.

System Optimization and Material Development of Solid Oxide Cells for Energy Conversion and Storage

by

Libin Lei

Bachelor of Engineering
Guangdong University of Technology, 2010

Master of Engineering
South China University of Technology, 2013

Submitted in Partial Fulfillment of the Requirements

For the Degree of Doctor of Philosophy in

Mechanical Engineering

College of Engineering and Computing

University of South Carolina

2018

Accepted by:

Fanglin (Frank) Chen, Major Professor

Kevin Huang, Committee Member

Xinyu Huang, Committee Member

John R. Regalbuto, Committee Member

Cheryl L. Addy, Vice Provost and Dean of the Graduate School

© Copyright by Libin Lei,2018

All Rights Reserved.

ACKNOWLEDGEMENTS

First, I would like to express my gratitude to my advisor, who has provided his knowledge, experience and insightful guidance during my doctoral study. Not only his encourage but also his critical comments for my study and research are the sources of energy for my progress. I would also like to thank my thesis committee members, Dr. Kevin Huang, Dr. John R. Regalbuto and Dr. Xinyu Huang for their invaluable suggestions and continuous support during my PhD study. Financial supports from the U.S. National Science Foundation (DMR-1210792), the US Department of Energy SECA Core Technology Program (under award number DE-FE0031176) are gratefully acknowledged.

Second, I would like to express my appreciation to my colleagues for their assistance and contributions to my research. It is great to have some encouraging discussions and cooperation with some of my colleagues, namely Dr. Shumin Fang, Dr. Tong Liu, Dr. Yao Wang, Dr. Yu Chen, Dr. Cong Ren, Dr. Zetian Tao, Dr. Xiaoming Wang, Dr. Jing Chen and Mr. Jihao Zhang.

Finally, I am very thankful for my parents, my girlfriend and my family. They support and encourage me when I am following my dream.

ABSTRACT

Solid oxide cells (SOCs) can convert chemical energy to electricity in the fuel cell mode and store electricity to chemicals in the electrolysis mode. However, there are still critical barriers, such as energy efficiency and durability, for the development and commercialization of SOCs. The objective of this dissertation is to apply system optimization and materials design to address the critical barriers for solid oxide cells in energy conversion and energy storage applications. One major focus of the dissertation is related to improve energy efficiency, enhance the cell performance and achieve multifunctionality in solid oxide electrolysis cells (SOECs). In addition, development of robust air electrode and mitigation of Cr poisoning in the air electrode of solid oxide fuel cells (SOFCs) is also pursued.

Electrolysis of steam or carbon dioxide using SOECs is a promising energy storage method that can efficiently convert electrical energy into chemicals. In conventional SOECs, a significant portion of electricity input is consumed to overcome a large oxygen potential gradient between the electrodes. Therefore, to reduce the electricity consumption and improve the system efficiency, a novel and efficient syngas generator, integrating carbon gasification and solid oxide co-electrolysis, is presented and evaluated in the first part of this dissertation. The feasibility of this new system is demonstrated in $\text{La}_{0.9}\text{Sr}_{0.1}\text{Ga}_{0.8}\text{Mg}_{0.2}\text{O}_3$ (LSGM) electrolyte-supported SOECs. Both thermodynamic calculation and experimental results show that the potential barrier for co-electrolysis can

be reduced by about 1 V and the electricity consumption can be reduced by more than 90% upon integration SOECs with carbon gasification. On the anode side, “CO shuttle” between the electrochemical reaction sites and solid carbon is realized through the Boudouard reaction ($C+CO_2=2CO$). Simultaneous production of CO on the anode side and CO/H₂ on the cathode side generates syngas that can serve as fuel for power generation or feedstock for chemical plants. The integration of carbon gasification and SOECs provides a potential pathway for efficient utilization of electricity, coal/biomass, and CO₂ to store electrical energy, produce clean fuel, and achieve a carbon neutral sustainable energy supply.

In the second part of this dissertation, to achieve multifunctionality and regulate product in SOECs, a novel micro-tubular electrochemical reactor is studied, in which high temperature co-electrolysis of H₂O-CO₂ and low temperature methanation processes are synergistically integrated. The temperature gradient along the micro-tubular reactor provides favorable conditions for both the electrolysis and methanation reactions. Moreover, the micro-tubular reactor can provide high volumetric factor for both the electrolysis and methanation processes. When the cathode of the micro-tubular reactor is fed with a stream of 10.7% CO₂, 69.3% H₂ and 20.0% H₂O, an electrolysis current of -0.32 A improves CH₄ yield from 12.3% to 21.1% and CO₂ conversion rate from 64.9% to 87.7%, compared with the operation at open circuit voltage. Furthermore, the effects of the inlet gas composition in the cathode on CO₂ conversion rate and CH₄ yield are systematically investigated. Higher ratio of H:C in the inlet results in higher CO₂ conversion rate. Among all the cases studied, the highest CH₄ yield of 23.1% has been achieved when the inlet gas in the cathode is consisted of 21.3% CO₂, 58.7% H₂ and 20.0% H₂O with an electrolysis current of -0.32 A.

Furthermore, the state-of-the-art SOECs are based on oxygen-ion conducting electrolyte (O-SOECs), but SOECs using proton-conducting electrolyte (H-SOECs) offer the advantages of producing dry and pure hydrogen. However, the development of H-SOECs falls far behind that of O-SOECs, mainly due to technical challenges such as the stability of the electrolyte and electrode in H₂O-containing atmosphere at operating conditions and the fabrication of thin electrolyte layer. Therefore, in the third part of the dissertation, BaZr_{0.8}Y_{0.2}O_{3-δ} (BZY) electrolyte and Sr₂Fe_{1.5}Mo_{0.5}O_{6-δ} (SFM) air electrode, both are stable in H₂O-containing atmosphere at operating conditions, are evaluated in H-SOECs. In addition, in order to improve the performance of H-SOECs, thin BZY electrolyte layer (about 16 μm in thickness) and nano-scaled SFM-BZY air electrode are fabricated successfully, showing excellent SOEC performance (-0.21 A cm⁻² at 600 °C) and achieving faradaic efficiency of 63.6% at intermediate temperature.

Solid oxide fuel cell (SOFC) is the reverse operation of SOEC and can directly convert the chemical energy in fuels to electricity with high efficiency and is fuel flexible. The durability and performance of SOFCs are highly related to the reaction kinetics and stability of the air electrode. To enhance the reaction kinetics of the air electrode, a novel hybrid catalyst consisting of PrNi_{0.5}Mn_{0.5}O₃ and PrO_x is impregnated in the conventional (La_{0.60}Sr_{0.40})_{0.95}Co_{0.20}Fe_{0.80}O_{3-x} (LSCF) air electrode of H-SOFCs for the first time. The effects of this impregnation on the electrochemical performance and durability of H-SOFCs are investigated in the forth part of the dissertation. Single cells with impregnated LSCF cathode and BZY electrolyte yield a maximum power density (MPD) of 0.198 W cm⁻² at 873 K, more than doubled than that with blank LSCF cathode (0.083 W cm⁻²) at the same operating conditions. Electrical conductivity relaxation (ECR) and

electrochemical impedance spectroscopy (EIS) studies reveal that the hybrid catalyst can substantially accelerate the oxygen-ion transfer and oxygen dissociation-absorption processes in the cathode, resulting in significantly lower polarization resistance and higher MPD. In addition, the hybrid catalyst possesses good chemical and microstructural stability at 600 °C. Consequently, the single cells with impregnated LSCF cathode show excellent durability. This study shows that the impregnation of this novel hybrid catalyst in the cathode could be a promising approach to improve the performance and stability of H-SOFCs.

Moreover, the state-of-the-art SOFC air electrode is suffering from chromium-poisoning, leading to high SOFC cell performance degradation. To mitigate the effect of Cr poisoning, placing Cr getter between the air electrode and the Cr sources is an efficient approach. However, the stability of the state-of-the-art Cr getter materials in the SOFC cathodic operation conditions remains challenging. For the first time, SFM is investigated as Cr getter material in the fifth part of the dissertation. The reactivity of SFM, which is stable in an atmosphere containing H₂O and CO₂, with Cr species (Cr₂O₃) is evaluated. Subsequently, the feasibility of SFM as Cr getter material is investigated. The experiment results show that SFM, which is stable in an atmosphere containing H₂O and CO₂, possesses high reactivity and selectivity with Cr species (Cr₂O₃). Consequently, the application of SFM layer can efficiently capture the gaseous Cr species, resulting in significant mitigation of Cr poisoning for the air electrode.

TABLE OF CONTENTS

ACKNOWLEDGEMENTS	iii
ABSTRACT.....	iv
LIST OF TABLES	x
LIST OF FIGURES	xi
CHAPTER 1 INTRODUCTION	1
1.1 BACKGROUND ABOUT SOLID OXIDE ELECTROLYSIS CELLS	1
1.2 THERMODYNAMICS OF ELECTROLYSIS	3
1.3 MATERIALS OF SOCs	6
1.4 CHROMIUM POISONING IN AIR ELECTRODE	11
1.5 OBJECTIVE AND STRUCTURE OF THIS DISSERTATION	14
CHAPTER 2 EFFICIENT SYNGAS GENERATION FOR ELECTRICITY STORAGE THROUGH CARBON GASIFICATION ASSISTED SOLID OXIDE CO- ELECTROLYSIS	17
2.1 BACKGROUND	17
2.2 EXPERIMENTAL.....	19
2.3 RESULTS AND DISCUSSION.....	21
2.4 CONCLUSIONS.....	33
CHAPTER 3 THE CO-ELECTROLYSIS OF CO ₂ -H ₂ O TO METHANE VIA A NOVEL MICRO-TUBULAR ELECTROCHEMICAL REACTOR.....	34
3.1 BACKGROUND	34
3.2 EXPERIMENTAL.....	36

3.3 RESULT AND DISCUSSIONS	37
3.4 CONCLUSIONS.....	49
CHAPTER 4 INTERMEDIATE-TEMPERATURE SOLID OXIDE ELECTROLYSIS CELLS WITH THIN PROTON-CONDUCTING ELECTROLYTE AND ROBUST AIR ELECTRODE	51
4.1 BACKGROUND	51
4. 2 EXPERIMENTAL.....	54
4.3 RESULT AND DISCUSSIONS	57
4.4 CONCLUSIONS.....	68
CHAPTER 5 A HIGHLY ACTIVE HYBRID CATALYST MODIFIED LSCF CATHODE FOR PROTON CONDUCTING SOLID OXIDE FUEL CELLS.....	70
5.1 BACKGROUND	70
5. 2 EXPERIMENTAL.....	72
5.3 RESULT AND DISCUSSIONS	75
5.4 CONCLUSIONS.....	84
CHAPTER 6 AN EFFICIENT AND HIGH-SELECTIVITY CHROMIUM GETTER FOR SOLID OXIDE FUEL CELLS	85
6.1 BACKGROUND	85
6. 2 EXPERIMENTAL.....	87
6.3 RESULT AND DISCUSSIONS	89
6.4 CONCLUSIONS.....	98
FUTURE WORK.....	99
REFERENCES	101

LIST OF TABLES

Table 2.01 Comparison of electricity consumption for 1 mole	32
syngas production in the CG assisted and conventional mode.	32
Table 3.01 Gibbs free energy (kJ/mol) of methanation reactions.....	38
Table 3.02 Direct synthesis of methane in solid oxide electrolysis cells.....	46
Table 3.03 CO ₂ conversion ratio, CH ₄ yield ratio and CH ₄ yield rate.....	46
Table 4.01 Comparison of the performance of typical H-SOFCs with BZY as the electrolyte.....	63
Table 4.02 Comparison of the performance of H-SOECs at 1.3 V	67
Table 5.01 Comparison of the performance of H-SOFCs with BZY as the electrolyte ...	83

LIST OF FIGURES

Figure 1.01 Schematic of O-SOEC and H-SOEC.	2
Figure 1.02 Thermodynamics of H ₂ O and CO ₂ electrolysis[9].	3
Figure 1.03 Schematic of chemical and morphological changes at air electrode-electrolyte interface during electrolysis[22].	9
Figure 1.04 Partial pressure of CrO ₂ (OH) ₂ in wet air (3%H ₂ O) and CrO ₃ in dry air over Cr ₂ O ₃ scale at different temperature[39].	12
Figure 2.01 Schematic illustration of carbon gasification assisted solid oxide co-electrolysis.	21
Figure 2.02 Thermodynamic calculation as function of temperature for co-electrolysis process (a) conventional mode and (b) CG assisted mode.	22
Figure 2.03 Calculated E _{re} and E _{tn} as a function of temperature for co-electrolysis process in the (a) conventional mode, and (b) CG assisted mode.	24
Figure 2.04 The microstructure of single cell (a) SFM-SDC/LSGM/SFM-SDC triple layers ; (b) interface of SFM-SDC and LSGM.	26
Figure 2.05 (a) <i>I-V</i> curves for the electrolysis cells operated in conventional mode and CG assisted mode at 1123K; (b) impedance spectra for electrolysis cells operated in four different conditions.	26
Figure 2.06 (a) Thermodynamic equilibrium calculation results for the reaction of 2 mol O ₂ with 98 mol carbon at different temperatures; (b) TG and DTG of carbon source in air and CO ₂ condition; (c) the exhaust gas composition in the air electrode side.	30
Figure 2.07 <i>I</i> -total energy efficiency curves for the electrolysis cell operated in conventional mode and CG assisted mode at 1123K.	32
Figure 3.01 Schematic of micro-tubular reactor.	37
Figure 3.02 Microstructure of micro-tubular reactor, (a) low magnification SEM image of the electrolysis region; (b) high magnification SEM image of the electrolysis region. ...	39

Figure 3.03 Electrochemical test of the electrolysis region in fuel cell mode with H ₂ as fuel at 1023 K, (a) I-V curve; (b) Electrochemical impedance spectrum under OCV.....	40
Figure 3.04 Electrochemical test of the electrolysis region in the electrolysis mode at 1023 K, (a) I-V curves; (b) impedance spectra under 1.3V. The inlet steam carrier is 15 sccm CO ₂ -H ₂ with 20 vol% humidity.	42
Figure 3.05 Gas composition in the exhaust (a) with the inlet gas composition: 10.7%CO ₂ -69.3%H ₂ -20%H ₂ O; (b) with the inlet gas composition: 21.3%CO ₂ -58.7% H ₂ -20.0% H ₂ O; and (c) with inlet gas composition: 32.0%CO ₂ -48.0%H ₂ -20.0%H ₂ O.....	43
Figure 3.06 Short term stability of the micro-tubular reactor (a) stability of the electrolysis region and (b) the gas composition in the exhaust.....	48
Figure 3.07 SEM images of the Ni-YSZ substrate (a) before the stability test; (b) after the stability test in the methanation region and (c) after the stability test in the electrolysis region.	49
Figure 4.01 Schematic of proton conducting solid oxide electrolysis cell with SFM as the air electrode.....	54
Figure 4.02 XRD patterns showing (a) chemical compatibility between SFM and BZY (b) the stability of SFM in 20%H ₂ O-air at 873 K.....	58
Figure 4.03 The stability of LSCF in 20%H ₂ O-Air at 873 K.	58
Figure 4.04 Electrochemical characterization of symmetrical cell (a) Impedance spectra in wet air (3% H ₂ O) at 873 K and its equilibrium circuit; (b) Arrhenius plot of polarization resistances.	59
Figure 4.05 SEM image (a) the cross section of single cell; (b) the surface of the BZY electrolyte; (c) the microstructure of SFM-BZY electrode at low magnification; (d) the microstructure of SFM-BZY electrode at high magnification.....	60
Figure 4.06 Electrochemical performance of single cells in the fuel cell mode (a) I-V curves at different temperatures; (b) Impedance spectrum under OCV at 873 K.....	62
Figure 4.07 I-V curves of single cell in electrolysis mode (3%H ₂ O-air in air electrode, 90%N ₂ -10%H ₂ in air electrode).....	63
Figure 4.08 Short term stability in electrolysis mode (a) Current vs time; (b) SEM image of SFM-BZY air electrode after the stability test; (c) Hydrogen evolution rate and faradaic efficiency.....	64
Figure 5.01 Schematic illustrations of blank LSCF electrode and PNM-PrO _x impregnated LSCF for H-SOFCs.....	72

Figure 5.02 XRD patterns (a) chemical compatibility between $\text{PrNi}_{0.5}\text{Mn}_{0.5}\text{O}_3$, PrO_x , and BZY; (b) Stability of $\text{PrNi}_{0.5}\text{Mn}_{0.5}\text{O}_3$ and PrO_x	75
Figure 5.03 FESEM images of the single cells. (a) The surface of the BZY electrolyte; (b) The cross-section view of NiO-BZY anode and BZY electrolyte.....	76
Figure 5.04 FESEM image of cathode (a) Microstructure of bare LSCF electrode; (b) Microstructure of LSCF electrode with $\text{PrNi}_{0.5}\text{Mn}_{0.5}\text{O}_3$ and PrO_x ; (c) High magnification of image of LSCF electrode with $\text{PrNi}_{0.5}\text{Mn}_{0.5}\text{O}_3$ and PrO_x	77
Figure 5.05 Electrochemical performance of single cells (a) I-V curves; (b) Maximum powder densities of single cells at various temperature.....	77
Figure 5.06 (a) Impedance spectra Impedance spectra of single cells at 650 °C; (b) Polarization resistance of single cells at various temperatures; (c) Polarization resistance R_H at various temperatures; (d) Polarization resistance R_L at various temperatures.	78
Figure 5.07 (a) Electrical conductivity relaxation as a function of time at 973 K; (b) Plots of the surface exchange coefficients (K_{eff}) as function of temperatures.....	80
Figure 5.08 (a) Stability of single cells at 873 K (a) Operation of single cells at 0.6 V; (b) The microstructure of electrode after 100 h test.	81
Figure 6.01 The schematic of test setup.....	89
Figure 6.02 The XRD patterns of SFM, Cr_2O_3 and mixture (1:1) before treatment.....	90
Figure 6.03 The XRD patterns of SFM after CO_2 and H_2O treatment.	90
Figure 6.04 The XRD patterns of SFM- Cr_2O_3 mixture (1:1) after treatment (a) at 1223 K and 1123 K; (b) at 1023 K and 923 K.....	91
Figure 6.05 The XRD patterns of SFM- Cr_2O_3 mixture (10:1) after treatment at 973 K and 1073K.....	92
Figure 6.06 Impedance spectra of LSCF at 1073 K (a) Blank; (b) with Cr_2O_3 ; (c) with Cr_2O_3 and SFM getter.....	93
Figure 6.07 Equilibrium circuit and fitting results of impedance spectra in Fig. 6.06(b). 95	
Figure 6.08 Microstructure characterization of LSCF (a) blank before test; (b) blank after test; (c) with Cr source; (d) with Cr source and SFM getter.	95
Figure 6.09 XPS spectra (a) Cr 2p; (b) Sr 3d; (c) Fe 2p; (d)Mo 3d.....	97

CHAPTER 1 INTRODUCTION

1.1 BACKGROUND ABOUT SOLID OXIDE ELECTROLYSIS CELLS

Fossil fuels, such as coal, oil and natural gas, are non-renewable energy resources and their ever-increasing consumption has led to excessive emission of greenhouse gases such as CO₂. Therefore, carbon emission reduction needs to be implemented and renewable energy sources have actively been developed globally in the past decades. Renewable energy sources such as wind and solar are now increasingly harvested to generate electricity, but the intermittent nature of these energy sources requires the capacity for large-scale electrical energy storage. Therefore, it's essential to develop efficient electricity storage technologies.

Electrolysis of steam/carbon dioxide by solid oxide electrolysis cells (SOECs) is a promising energy storage method that can efficiently transform electrical energy into non-fossil syngas (a mixture of H₂ and CO) which can be converted to electricity when required[1-3]. Meanwhile, it is an excellent alternative for CO₂ utilization due to its high conversion rate and flexibility[4, 5]. The produced syngas can also be subsequently used as feedstock through the well-established Fischer-Tropsch (F-T) process to produce liquid synthetic fuel that can be easily stored and transported using the existing infrastructure compared with the alternative hydrogen[6]. Compared with low-temperature proton exchange membrane (PEM) electrolyzers and alkaline electrolyzers, high temperature SOECs offer significant advantages. For example, besides hydrogen, syngas can be produced in SOECs; higher reaction rate and lower requirement of electrical energy can be

achieved for its high operation temperature[7]. In the past decade, there have been increasing research interests in SOECs[8].

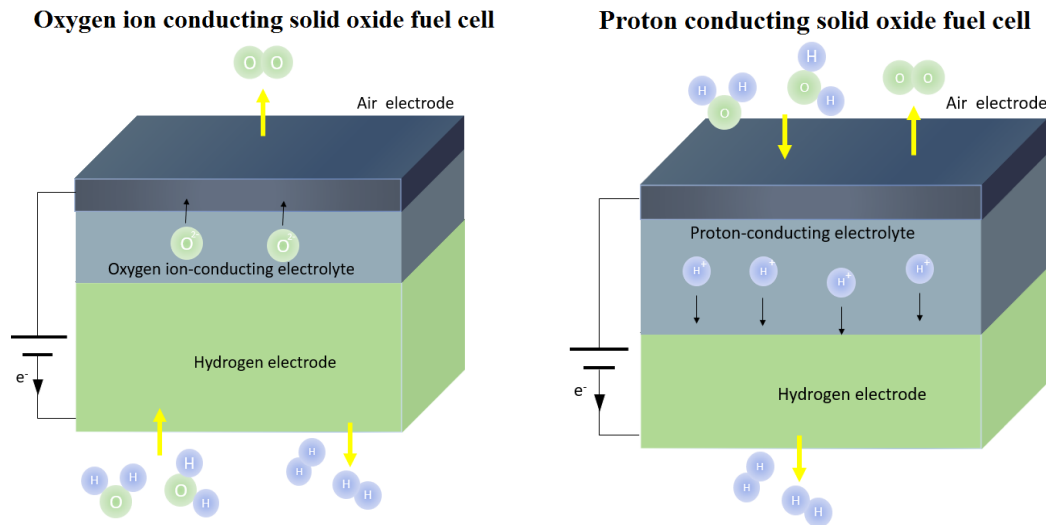
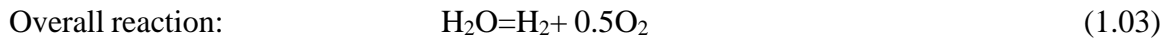
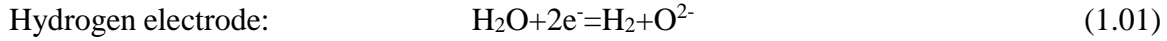
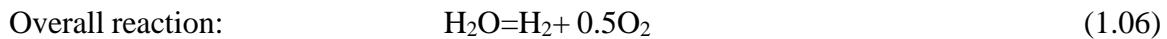
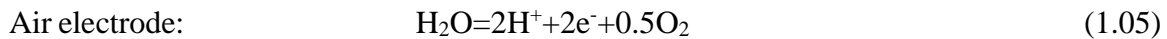
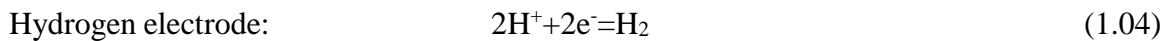


Figure 1.01 Schematic of O-SOEC and H-SOEC.

According to the types of the electrolyte, SOECs can be classified into two kinds, namely oxygen-ion conducting SOECs (O-SOECs) and proton conducting SOECs (H-SOECs), as shown in Fig. 1.01. In O-SOECs, the electrolyte is oxygen ion conductor. Steam is fed to the porous hydrogen electrode side. When the required electrical potential is supplied to the SOECs, water molecules diffuse to the reaction sites and are dissociated to form hydrogen gas and oxygen ions at the triple phase boundaries of the hydrogen electrode. The produced hydrogen gas diffuses to the hydrogen electrode surface and is collected. The oxygen ions are transported through the electrolyte layer to the air electrode. On the air electrode side, the oxygen ions are oxidized to oxygen gas. The reactions in each electrode and overall reaction can be written as:



By contrast, the electrolyte is proton conductor in H-SOECs. Steam is fed to the air electrode side. When the required electrical potential is applied to the H-SOECs, water molecules diffuse to the reaction sites and are dissociated to form protons, oxygen gas and electrons at the triple phase boundaries of the air electrode. The protons are transported through the electrolyte layer to the hydrogen electrode side and then accept electrons to produce hydrogen gas. The reactions in each electrode as well as the overall reaction can be written as:



1.2 THERMODYNAMICS OF ELECTROLYSIS

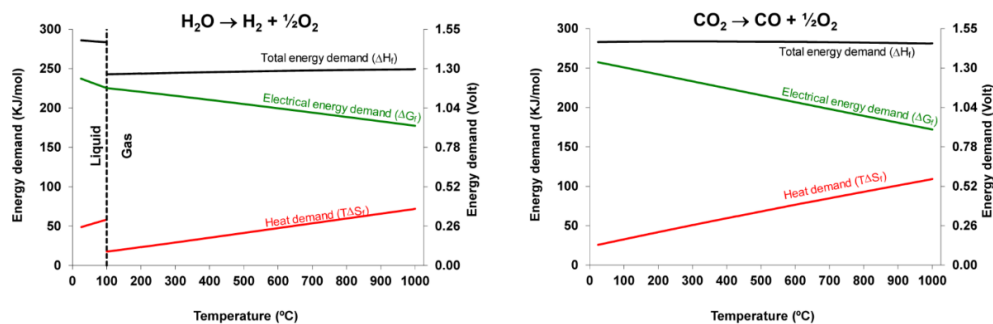


Figure 1.02 Thermodynamics of H_2O and CO_2 electrolysis[9].

Fig. 1.02 shows the thermodynamics of H_2O and CO_2 electrolysis. The total energy demand (ΔH_f) remains almost the same from 373 K (100 °C) to 1273 K (1000°C) for H_2O

and CO₂ electrolysis. The heat demand ($T\Delta S_f$) increases with increasing temperature, while the electrical energy demand (ΔG_f) shows the opposite trend. In other words, at elevated temperature, a significant part of the total energy demand can be provided as heat instead of electricity. In addition, this provides an opportunity to utilize the heat that is inevitably produced when electrical current is passed through the electrolysis cell. Consequently, the overall consumption of electrical energy is reduced and the efficiency for production of H₂ and/or CO can be increased, when the operation temperature of electrolysis is increased. This nature of electrolysis provides advantages to SOECs operated at high temperature, compared with low temperature electrolysis cells.

During the operation of electrolysis, a voltage (E), which is higher than open circuit voltage (reversible voltage E_{re}), is required to be applied to the electrolysis cells. Reversible voltage E_{re} is defined as the minimum voltage required for splitting of either H₂O or CO₂. The thermodynamic definition of E_{re} is as equation (1.07):

$$E_{re} = -\frac{\Delta G}{nF} \quad (1.07)$$

where ΔG is Gibbs free energy of reaction, n is the number of electrons involved in the reaction and F is the Faraday constant.

In addition, thermoneutral voltage E_{tn} is another important parameter in SOECs. It is defined as the voltage at which the generated heat in the electrolysis cell and the heat consumption are equal. The thermodynamic definition of E_{tn} is as equation (1.08)[9]:

$$E_{tn} = -\frac{\Delta H}{nF} \quad (1.08)$$

where ΔH is the molar enthalpy change of reaction. Theoretically speaking, there are three thermodynamic statuses of electrolysis, namely endothermic status ($Q_{re} > Q_{ir}$), exothermic

status ($Q_{re} < Q_{ir}$) and thermoneutral status ($Q_{re} = Q_{ir}$). Where Q_{re} and Q_{ir} are the reversible heat and irreversible heat respectively. When the operating voltage (V_{op}) of electrolysis is between E_{re} and E_{tn} ($E_{re} < V_{op} < E_{tn}$), extra heat input is needed to balance the enthalpy change (endothermic status). In exothermic mode, the operating voltage is higher than the thermoneutral voltage ($V_{op} > E_{tn}$), extra heat, produced from resistance of the electrolysis cell, has to be removed from the system. When operating the electrolysis cell under thermoneutral condition ($V_{op} = E_{tn}$), no extra heating and cooling is needed. Because compared with heat, electricity is a more valuable form of energy, electricity is not desired to transform into heat redundantly. Therefore, the SOECs is preferred to be operated in endothermic status and especially in thermoneutral status.

In practice, the partial pressure of reactants or products is usually not 1. Especially in SOECs, the inlet gas is always a gas mixture. Consequently, equation (1.07) is not enough to predict the OCV of SOECs in practical use. In O-SOECs, equation (1.09), as shown below, is developed for calculation of OCVs:

$$E_{OCV} = \frac{RT}{4F} \ln \frac{P_{O_2,airelectrode}}{P_{O_2,hydrogenelectrode}} \quad (1.09)$$

Where F is the Faraday constant, T the temperature (K), R the gas constant, and, $P_{O_2,airelectrode}$ and $P_{O_2,hydrogenelectrode}$ are the oxygen partial pressure.

In term of H-SOECs, because not only proton but also oxygen ion and electron can transport through the electrolyte, the calculation of OCVs is more complicated, compared with that in O-SOECs. Considering the transport number of different carriers, the OCVs of H-SOECs can be calculated by the following equation[10]:

$$E_{OCV} = t_o E_O + t_H E_H = t_o \frac{RT}{4F} \ln \left(\frac{P_{O_2,air\ electrode}}{P_{O_2,hydrogen\ electrode}} \right) + t_H \frac{RT}{2F} \ln \left(\frac{P_{H_2,hydrogen\ electrode}}{P_{H_2,air\ electrode}} \right)$$

(1.10)

where t_o and t_H are the actual transport numbers of oxygen ions and protons respectively, E_O and E_H are the thermodynamic OCV values of oxygen and hydrogen cells. Equation (1.10) can be presented in another form:

$$E_{OCV} = t_i E_O + t_H E_{H_2O} = t_i \frac{RT}{4F} \ln \left(\frac{P_{O_2,air\ electrode}}{P_{O_2,hydrogen\ electrode}} \right) + t_H \frac{RT}{2F} \ln \left(\frac{P_{H_2O,hydrogen\ electrode}}{P_{H_2O,air\ electrode}} \right)$$

(1.11)

where $t_i = t_o + t_H$ is the actual transport numbers of ions, E_O and E_H are the thermodynamic OCV values of oxygen and hydrogen cells, $P_{H_2O,airelectrode}$ and $P_{H_2O,hydrogenelectrode}$ are the steam partial pressure. If the steam partial pressures are the same in both electrode, equation (1.11) can be greatly simplified.

1.3 MATERIALS OF SOECs

1.3.1 ELECTROLYTE

According to the classification of SOECs, there are two kinds of electrolyte, namely oxygen ion conductor and proton conductor. The most widely used oxygen ion conducting electrolyte is yttria-stabilized zirconia (YSZ), which exhibits high oxygen ion conductivity at high temperature (above 1073 K) and good mechanical strength. However, the typical high operating temperature (above 1073 K) results in high performance degradation rate in the range of 1-4%/1000h and high material cost. Therefore, lowering the operation temperature of SOECs can potentially improve durability, reduce materials issues, increase nanostructure stability, expand heat source choice, reduce BOP cost, and improve system

efficiency. But relatively low oxygen ion conductivity of YSZ at intermediate temperature (below 973 K) limits its application.

For the application at intermediate temperature (below 837K to 973 K), doped lanthanum gallate is alternative electrolyte material for O-SOECs. The doped LaGaO₃ material has been found to have good ionic conductivity. The conductivity of La_{0.9}Sr_{0.1}Ga_{0.8}Mg_{0.2}O₃ (LSGM) has been reported to be 0.17 S/cm at 1073 K, which is much higher than YSZ (0.026S/cm at 1073 K)[7]. However, LSGM is suffering serious reactions with Ni on the hydrogen electrode [7]. This will require modification of the conventional nickel based fuel electrode to avoid the formation of LaNiO₃ and fracture due to thermal expansion coefficient (TEC) mismatch between electrolyte and electrodes.

Similar to LSGM, the doped ceria is considered as a potential intermediate-temperature electrolyte for SOFC because of its high oxygen ions conductivity at a temperature between 773 and 973 K [11]. However, partial reduction of Ce⁴⁺ to Ce³⁺ in reducing environment leads to significant electronic conduction. As a result, a partial internal electronic short-circuit happens in the electrolyte, leading to decrease of the current efficiency and lattice expansion which may lead to mechanical failure[12].

For proton conducting electrolyte, there are mainly two groups, namely proton conducting cerate and zirconate oxides. The electrolyte material is required to be stable in H₂O-containing atmosphere in the operating conditions. However, proton-conducting cerate oxides, which are the most-widely investigated material for proton-conducting solid oxide fuel cells (H-SOFCs), have been shown to be chemically unstable in H₂O-containing atmosphere both thermodynamically[13] and experimentally[14] at typical cell operating conditions. Even partial Zr-doping for cerates cannot completely stabilize the proton

conducting cerate oxide in H₂O-containing atmosphere[15, 16]. On the contrary, proton-conducting zirconate oxides have been proven to be chemically stable in H₂O-containing atmosphere[17, 18], making them the choice electrolyte for H-SOECs.

1.3.2 AIR ELECTRODE MATERIAL

In O-SOECs, the steam is fed to the hydrogen electrode and the air electrode is still exposed to dry air atmosphere, which is the same of O-SOFCs. Therefore, conventional air electrode materials of O-SOFCs can be applied to O-SOECs directly. So far, lanthanum strontium manganate (LSM) is the most widely used air electrode material for O-SOECs [19, 20]. However, it has been reported that LSM air electrode delaminates from YSZ electrolyte during electrolysis due to high internal oxygen pressure near the air electrode-electrolyte interface and the formation of lanthanum zirconate, as shown in Fig. 1.03 [21]. Grave *et al.* have reported that this electrolysis induced degradation can be completely eliminated by reversibly cycling between electrolysis and fuel cell mode [22].

The high internal oxygen pressure near the air electrode-electrolyte interface is due to the low ionic conductivity of LSM ($5.93 \times 10^{-7} \text{ S cm}^{-1}$ at 1073 K). Mixed ionic electronic conducting (MIEC) oxides, such as lanthanum strontium cobalt ferrite (LSCF), have been applied to O-SOECs as air electrode material [23, 24]. In addition, redox stable perovskite materials, such as Sr₂Fe_{1.5}Mo_{0.5}O_{6-δ} (SFM), have also been studied as air electrode material of O-SOEC. SFM processes high oxygen ionic conductivity (0.13 S cm^{-1} at 1073 K in air), reasonable electrical conductivity (14.93 S cm^{-1} at 1023 K in air) and shows excellent electrochemical catalytic activity [25].

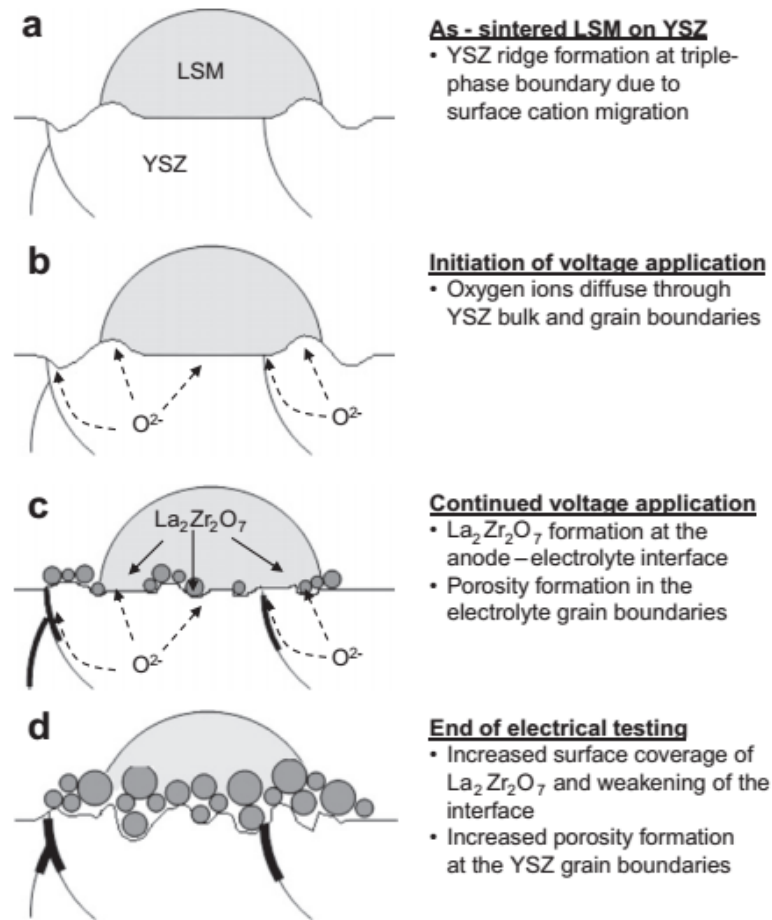


Figure 1.03 Schematic of chemical and morphological changes at air electrode-electrolyte interface during electrolysis[22].

Unlike in O-SOEC, the steam is fed to the air electrode side in H-SOEC, as shown in Fig. 1.01. Therefore, the air electrode material is required to be chemically stable in atmosphere with high humidity. Up to now, most of the air electrode materials in H-SOEC reported are only derived from proton conducting solid oxide fuel cells (H-SOFCs), but the performance of these conventional H-SOFC air electrode materials doesn't meet the requirements of H-SOECs. As an example, LSCF (La_{0.6}Sr_{0.4}Co_{0.2}Fe_{0.8}O_{3-δ}), a conventional air electrode material for H-SOFC, has good electronic and ionic conductivity. However,

its stability in H₂O-containing atmosphere is a serious concern, especially at intermediate temperature range of 873-973 K [26, 27]. Therefore, it is essential to develop new material for the air electrode of H-SOEC.

1.3.3 HYDROGEN ELECTRODE MATERIALS

The potential hydrogen electrode material has to meet the following requirements including (1) good catalytic activity, (2) sufficient electronic conductivity, (3) proper thermal compatibility and (4) good chemical stability. The Ni-based electrode is the most common hydrogen electrode material for SOECs because of its high electrical conductivity, excellent catalytic activity for high temperature steam/CO₂ splitting reaction and low cost[28]. The ionic conductor electrolyte phase such as YSZ or GDC is incorporated in hydrogen electrode to increase the ionic conductivity, match the thermal expansion coefficient (TEC) with the electrolyte and extend the triple phase boundaries (TPBs). SOECs with the Ni-based hydrogen electrode have displayed good electrochemical performance with low polarization resistance and high electrolysis current density [29, 30].

Although the nickel-based cermets are the most common hydrogen electrode material for SOECs, Ni has poor tolerance to impurity poisoning and is susceptible to microstructure changes from thermal or redox cycling, resulting in loss of TPBs and cell performance degradation in long-term operations [25, 31]. Consequently, new ceramic materials such as LaCrO₃, SrTiO₃, SFM, and LaVO₃-based materials have been investigated as alternative and more stable hydrogen electrode materials for SOECs.

Pervoskite LaCrO₃-based materials are stable and conductive in both reducing and oxidizing atmospheres. They are widely used as interconnect material and have been applied as hydrogen electrode candidate for SOECs. LaCrO₃ is a p-type conductor, and the

electronic and ionic conductivity is tunable by adjusting the co-doping of divalent ions such as Sr^{2+} , Ca^{2+} and Mg^{2+} to the A-sites and transition metal ions such as Mn^{2+} , Fe^{2+} and Co^{2+} to the B-sites [32-34].

Perovskite oxide $\text{La}_x\text{Sr}_{1-x}\text{TiO}_{3+\delta}$ (LST) is another alternative ceramic hydrogen electrode material for SOECs. It is a typical n-type semiconductor and can achieve an electrical conductivity as high as 30 S cm^{-1} at intermediate temperature upon reduction in reducing atmosphere. Furthermore, LST is stable in pure H_2 up to 1673 K. Therefore, LST has attracted much attention to be used as hydrogen electrode materials in the SOC [35]. Xie *et al.* have utilized the electronic conductor (LST) and oxygen-ion conductor (GDC) to form LST-GDC composite hydrogen electrode for co-electrolysis application. The electrolyte-supported SOECs with the cell configuration of LST-CGO/YSZ/LSM-GDC functioned well in the electrolysis conditions even without using hydrogen as the reducing gas as typically required in the electrolysis cells using nickel-based hydrogen electrode[36].

Perovskite Sr-doped LaVO_3 (LSV) exhibits high electronic conductivity about 120 S cm^{-1} at 1073 K, and it is also very stable over a wide range of oxygen partial pressure from 10^{-4} to 10^{-22} atm with considerable sulfur tolerance and coking resistance at elevated temperature. Yoon *et al.* [37] have reported the co-electrolysis performance of LSV-YSZ composite materials as hydrogen electrode for electrolyte-supported cells with the configuration of LSV-YSZ/YSZ/LSF-YSZ, which exhibited the cell polarization resistance of $0.89 \Omega \text{ cm}^2$ at 1073 K in the 70% (20% CO -80% CO_2)-30% H_2O atmosphere.

1.4 CHROMIUM POISONING IN AIR ELECTRODE

The reducing operation temperature of SOCs greatly increases the feasibility of using low cost metallic interconnect materials. Compared to the ceramic interconnect materials

such as Sr-doped lanthanum chromite, metallic materials have high electronic and thermal conductivity, negligible ionic conductivity, good machinability and low cost. However, the oxidation and corrosion on metal surface becomes problematic at elevated SOCs operating temperatures, which may lead to substantial increase in the ohmic resistance of SOC stack. High Cr content alloys draw significant attention because of their anti-oxidation property at high temperatures. However, the volatilization of gaseous Cr-species from the alloy surface leads to drastically degradation of air electrode performance which becomes a serious issue in SOC development and commercialization [38]. Cr vaporization is affected by several factors such as the flow rate, flow regime, temperature and humidity. The representative vapor species of Cr are CrO_3 in dry air and $\text{CrO}_2(\text{OH})_2$ in wet air. Fig. 1.04 shows the temperature dependence of the partial pressure of these two main Cr species over Cr_2O_3 scale in wet and dry air, respectively [39]. From Fig. 1.04, it can be seen that the partial pressure of $\text{CrO}_2(\text{OH})_2$ is larger than that of CrO_3 , suggesting that Cr vaporization is more serious in wet air than in dry air. In addition, the partial pressures of $\text{CrO}_2(\text{OH})_2$ and CrO_3 increase with increasing temperature.

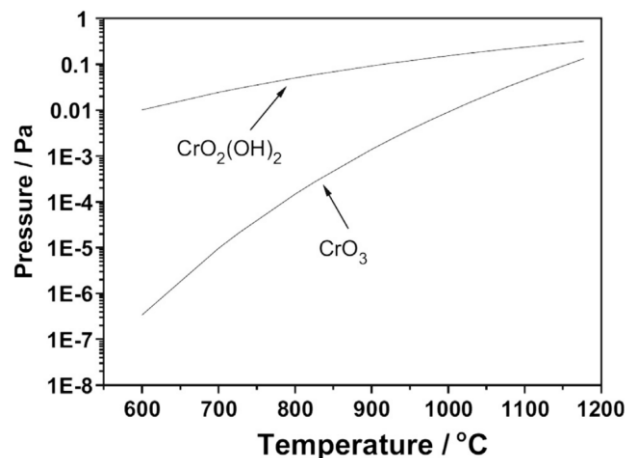


Figure 1.04 Partial pressure of $\text{CrO}_2(\text{OH})_2$ in wet air (3% H_2O) and CrO_3 in dry air over Cr_2O_3 scale at different temperature [39].

Two general pathways have been reported for Cr-poisoning, one is the chemical reaction and the other is the electrochemical reaction. The representative chemical reaction pathway has been demonstrated by Jiang *et al.* [38] who have systematically studied the Cr deposition mechanism in LSM and LSCF air electrode. In LSM, Mn^{2+} was generated during air electrode polarization at high temperature, which served as the nucleation agent for the formation of Cr_2O_3 from Cr-Mn-O nucleus for LSM, as shown in reactions (1.12-1.15):



In LSCF, SrO served as the nucleation agent for LSCF air electrode, as shown in reactions (1.16-1.18):



In the electrochemical reaction pathway, it has been suggested that volatile $CrO_2(OH)_2$ is formed under typical SOFC operating conditions. These gas phase chromium species can deposit on the air electrode forming Cr_2O_3 , while the oxide anions diffuse through the electrolyte, as shown in reaction (1.19):



Whether through chemical or electrochemical pathways, deposition of Cr-containing compounds at the air electrode/electrolyte interface not only reduces the TPBs but also

limits oxygen exchange with the bulk electrolyte, degrading overall fuel cell performance. Considering the electrochemical pathways, a mixed ionic and electronic conducting air electrode is more tolerant to Cr-poisoning due to the expansion of the area available for electrochemical deposition of chromia and the promotion of chromia deposition in less critical areas instead of only to the air electrode/electrolyte interface for a predominantly electronic conducting air electrode. In addition, to reduce the concentration of the volatile chromia species, metallic interconnect surfaces have been subjected to various coatings. The function of the coating is to form a ceramic phase that is electrically conducting but has lower chromia evaporation rates. However, coatings also increase the cost for the metallic interconnects. Complete coverage of the entire metallic surfaces is often difficult due to the complex geometry for most of the metallic interconnect designs. The long-term reliability of the coating is also a concern. Consequently, Cr getter materials have been developed to mitigate the air electrode Cr-poisoning by capturing the volatile Cr-species before they reach the electrochemically active air electrodes[40, 41]. Uddin *et al.* [41] have reported that the application of a Cr getter layer can efficiently prevent Cr poisoning in the bulk air electrode and air electrode-electrolyte interface. However, the stability of Cr getter material in operation condition and the replacement of Cr getter layer in SOC stacks are still problems.

1.5 OBJECTIVE AND STRUCTURE OF THIS DISSERTATION

According to the discussions above, one objective of this proposal is to optimize the system of SOEC to increase energy efficiency. In conventional SOECs, a significant portion of electricity input is consumed to overcome a large oxygen potential gradient between the electrodes. Therefore, in the Chapter 2 of this dissertation, to improve the

system efficiency, a novel and efficient syngas generator, integrating carbon gasification and solid oxide co-electrolysis, is presented. The electrochemical performance and energy efficiency of this novel system have been investigated and compared with those of conventional O-SOECs. Furthermore, in the Chapter 3 of this dissertation, for direct synthesis of methane in co-electrolysis, a novel micro-tubular electrochemical reactor is presented. High temperature co-electrolysis of $\text{H}_2\text{O}-\text{CO}_2$ and low temperature methanation processes are synergistically integrated in this reactor. The performance and stability of this reactor have been studied. The effect of inlet gas composition on the conversion percentage of CO_2 and the yield of CH_4 have also been investigated.

Moreover, another objective of this dissertation is focused on developing robust and high performance air electrode material for proton conducting solid oxide reversible cells (H-SORC). The development of H-SOCs is far behind that of O-SOCs, mainly due to technical challenges such as the stability of the electrolyte and electrode in H_2O -containing atmosphere at operating conditions and the sluggish reaction kinetics in the air electrode. Therefore, in the Chapter 4 of this dissertation, to solve the stability problem, $\text{BaZr}_{0.8}\text{Y}_{0.2}\text{O}_{3-\delta}$ (BZY) electrolyte and $\text{Sr}_2\text{Fe}_{1.5}\text{Mo}_{0.5}\text{O}_{6-\delta}$ (SFM) air electrode, both are stable in H_2O -containing atmosphere at operating conditions, are applied and evaluated H-SOECs. In the Chapter 5 of this dissertation, to enhance the reaction kinetics in the air electrode, a novel hybrid catalyst consisting of $\text{PrNi}_{0.5}\text{Mn}_{0.5}\text{O}_3$ and PrO_x is impregnated in the conventional LSCF air electrode of H-SOFCs for the first time. The effects of this impregnation on the electrochemical performance and durability of H-SOFCs are investigated.

The volatilization of gaseous Cr-species from Cr containing interconnect materials leads to drastically degradation of air electrode performance which becomes a serious issue in SOC development. To mitigate the effect of Cr poisoning, introducing Cr getter between the air electrode and the Cr sources is an efficient approach. However, the stability of the state-of-the-art Cr getter materials in the SOFC cathodic operation conditions remains challenging. For the first time, $\text{Sr}_2\text{Fe}_{1.5}\text{Mo}_{0.5}\text{O}_{6-\delta}$ (SFM) is investigated as Cr getter material in the Chapter 6 of this dissertation. The reactivity of SFM, which is stable in an atmosphere containing H_2O and CO_2 , with Cr species (Cr_2O_3) is evaluated. Subsequently, the feasibility of SFM as Cr getter material is investigated.

CHAPTER 2 EFFICIENT SYNGAS GENERATION FOR ELECTRICITY STORAGE THROUGH CARBON GASIFICATION ASSISTED SOLID OXIDE CO-ELECTROLYSIS

2.1 BACKGROUND

There are some paramount challenges for the large scale deployment of SOECs[8, 30, 42, 43]. One major challenge is that a significant portion of electricity input is consumed to overcome a large oxygen potential gradient (open circuit voltage up to 1 V) in the co-electrolysis process, because the air electrode is often exposed to air with a high oxygen partial pressure[44]. Considering that the electrical consumption is crucial for its commercial competitiveness, it is very desirable to reduce the oxygen partial pressure of the air electrode in order to lower the open circuit voltage (OCV). Furthermore, utilization of oxygen produced in the air electrode is also vital for improving the overall system efficiency. However, there are only very limited reports concerning the reduction of oxygen potential gradient in SOECs. Martinez-Frias et al. reported that natural gas assistance can reduce the OCV of electrolysis and improve the efficiency with heat recovery system[44]. Wang et al. reported that introduction of reducing gases (CH_4 or CO) in the air electrode can decrease the electrochemical potential required for electrolysis [45, 46]. However, in these studies, the utilization of oxygen produced in the air electrode is ignored. In contrast, we have recently demonstrated a strategy that combines partial

oxidation of methane and co-electrolysis, in which the potential barrier is reduced and oxygen (produced in the air electrode) is utilized to partially oxidize methane to produce syngas[47].

Carbon gasification (CG) is a process to transform carbon-containing solids (such as coal and biomass) into gaseous fuels such as CO, H₂, and CH₄. It has emerged as a clean and effective way for the production of gaseous fuels that can be used for power generation or synthesis of chemicals [48, 49]. CG is already a well-developed technology and has been widely applied in Integrated Gasification Combined Cycle (IGCC), production of syngas, and solid oxide fuel cells (SOFCs) [50-62]. Similarly, solid oxide co-electrolysis and CG process can be synergistically combined and an integrated paradigm can be achieved. The production of CO by carbon gasification in the air electrode side can eliminate the uphill potential barrier in SOECs. Furthermore, partial oxidation of carbon in the air electrode is an exothermic reaction that can provide heat for the endothermic electrolysis reaction in the hydrogen electrode. Carbon-based solid oxide steam electrolysis, containing molten silver as the air electrode has been described theoretically [63]. Noticeably, above certain temperature, carbon-based solid oxide steam electrolysis process can occur spontaneously without input of external electricity. The feasibility of steam-carbon solid oxide electrochemical cells for hydrogen production has been reported [64-66]. However, the feasibility of syngas production has not been reported yet for carbon assisted SOECs. Compared with the steam electrolysis (hydrogen production), co-electrolysis of H₂O and CO₂ (syngas production) is not only an energy conversion method but also an effective CO₂ utilization method. Moreover, the behaviour of the CG process and the product in the

air electrode side in CG-assisted SOEC have not been reported, which are critical to assess the energy efficiency of the system.

In this chapter, a novel and efficient syngas generator, in which carbon gasification and solid oxide co-electrolysis process are synergistically combined, is presented, as schematically illustrated in Fig. 2.01. The feasibility of this novel integrated system has been studied in $\text{La}_{0.9}\text{Sr}_{0.1}\text{Ga}_{0.8}\text{Mg}_{0.2}\text{O}_3$ (LSGM) electrolyte-supported SOECs. The carbon gasification process in the air electrode side is investigated by thermogravimetry (TG) and gas chromatography (GC). Based on the electrochemical and GC data, electricity consumption and energy efficiency of this device are calculated to demonstrate its advantages.

2.2 EXPERIMENTAL

2.2.1 THE CHARACTERIZATION OF CARBON POWDERS

The carbon source used in this study is activated carbon with 10 wt.% Fe loading [58]. The gasification behaviours of carbon powder were studied by thermogravimetric analysis (STA 449 F1 Jupiter, Netzsch, Germany) in air and in CO_2 atmosphere, respectively over the temperature range of 323–1273 K. The heating rate was fixed at 5 K min^{-1} . The total flow rate of gases was 60 ml min^{-1} . Thermodynamic calculation was conducted using the HSC 6.0 software.

2.2.2 PREPARATION OF SINGLE CELLS

Dense electrolyte support was prepared by pressing $\text{La}_{0.9}\text{Sr}_{0.1}\text{Ga}_{0.8}\text{Mg}_{0.2}\text{O}_3$ (LSGM) (Fuel Cell Materials, USA) powders into pellets and then sintered at 1723 K for 5 h. After sintering, the LSGM pellet is 10.7 mm in diameter and 0.5 mm in thickness. The electrode ink consisting of 60 wt.% $\text{Sr}_2\text{Fe}_{1.5}\text{Mo}_{0.5}\text{O}_{6-\delta}$ (SFM) and 40 wt.% $\text{Sm}_{0.2}\text{Ce}_{0.8}\text{O}_{1.9}$ (SDC) was

screen-printed on both sides of the LSGM electrolyte and then fired at 1373 K for 2 h. The effective electrode area was about 0.33 cm². Gold paste was used as the current collector.

2.2.3 CELLS CHARACTERIZATION

The prepared SFM-SDC/LSGM/SFM-SDC single cells were sealed between two alumina tubes using silver paste (DAD-87, Shanghai Research Institute of Synthetic Resins, China). High temperature ceramic adhesive (552-1105, Aremco, USA) was then applied outside the sealed cell to minimize gas leaking. 8 ml min⁻¹ CO₂ (16 vol.%), 10 ml min⁻¹ H₂ (20 vol.%), 24 ml min⁻¹ N₂ (48 vol.%) and 8 ml min⁻¹ H₂O (16 vol.% AH) were introduced in the hydrogen electrode side during the electrolysis test. The flow rates of CO₂, H₂ and N₂ were controlled by mass flow controllers (APEX, Schoonover, USA). Steam was generated using a humidifier by heating liquid water to a pre-determined temperature. Heating tape was used to surround gas pipes to avoid condensation. The exact water partial pressure of the inlet gases was continuously measured using a humidity sensor (HMP 337, Vaisala, USA). Carbon source was placed into the upper tube of the air electrode side. The exhaust gas with 5 mL min⁻¹ N₂ as sweep gas from the air electrode side was analysed by a gas chromatograph (7890A, Agilent, USA). Electrochemical characterizations including current density-voltage *I-V* and impedance spectra measurements for the single cells were conducted on an electrochemical test system (Versa STAT 3-400, Princeton Applied Research, USA). The *I-V* curves were recorded from OCV to OCV+1V with a voltage sweeping speed of 0.03 V s⁻¹. Electrochemical impedance spectra (EIS) under both OCV and electrolysis conditions (0.15 mA cm⁻²) were recorded with a voltage amplitude of 30 mV.

2.3 RESULTS AND DISCUSSION

2.3.1 THE PRINCIPLE AND THERMODYNAMIC CALCULATION OF CONVENTIONAL AND CG ASSISTED CO-ELECTROLYSIS

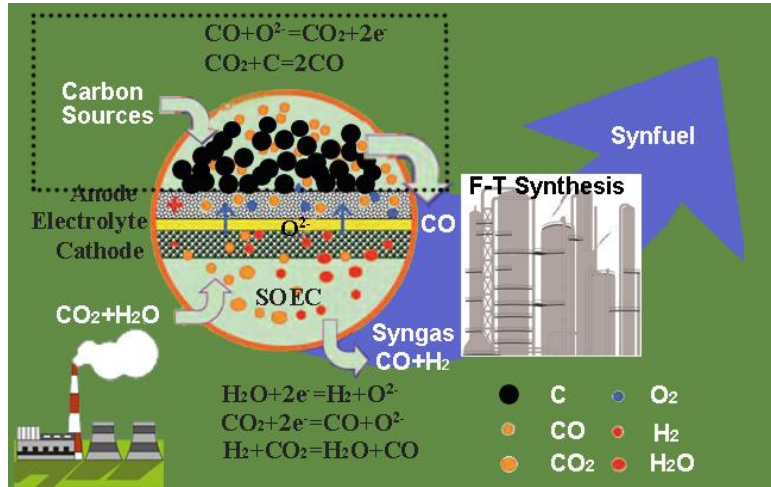


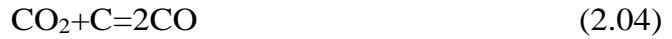
Figure 2.01 Schematic illustration of carbon gasification assisted solid oxide co-electrolysis.

Fig. 2.01 illustrates the working principle of the CG assisted co-electrolysis, which is the same as the conventional co-electrolysis in the hydrogen electrode side. In both modes, a feed stream consisting of H_2O and CO_2 is introduced to the hydrogen electrode side, where H_2O and CO_2 accept electrons from an external circuit to produce H_2 , CO and oxygen ion O^{2-} , as described in reactions (2.01) and (2.02). Reverse water gas shift reaction (RWGSR) also takes place in the hydrogen electrode side, as described in reaction (2.03).



Compared with the conventional co-electrolysis, the significant distinction of the CG assisted co-electrolysis is that carbon source is introduced in the air electrode

side, as shown in Fig. 2.01 (within the dotted rectangle). Through the Boudouard reaction (reaction (2.04)), carbon reacts with CO₂ to produce CO. The produced CO diffuses to the triple phase boundary (TPB) sites of the air electrode to react with O²⁻ to form CO₂, releasing electrons at the same time, as described in reaction (2.05). Consequently, a sustainable cycle is realized due to the diffusion of CO gases and the related reactions (2.04)-(2.05), similar to the “CO shuttle mechanism” in direct carbon solid oxide fuel cells (DC-SOFCs) [60].



The overall reaction of the CG assisted co-electrolysis is shown in reaction (2.06):

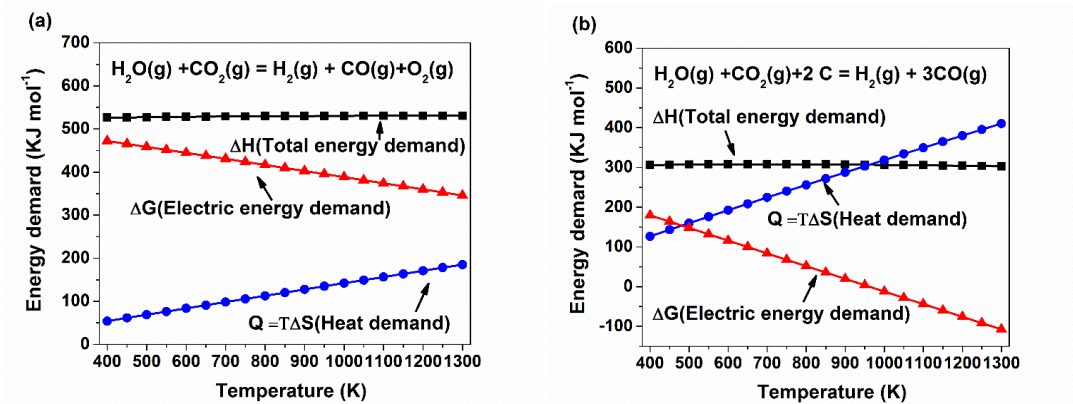
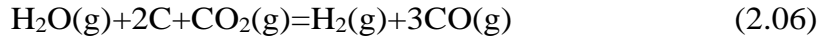


Figure 2.02 Thermodynamic calculation as function of temperature for co-electrolysis process (a) conventional mode and (b) CG assisted mode.

Fig. 2.02 shows the thermodynamic calculation results for the co-electrolysis in different modes. When operated in the conventional mode, the process requires a total amount of energy (ΔH) about 528 kJ mol⁻¹ in the temperature range from 400 to 1300 K. Although the electrical energy demand shown in Fig. 2.02(a) decreases

at higher temperature with the significantly increase of heat due to the positive entropy change (ΔS), even at 1300 K, the ΔG still maintains at a high positive value above 300 kJ mol^{-1} . Since electricity is much more valuable than joule heat which may be readily available in the typical industrial processes or from solar heating, this inevitably high electrical input definitely degrades the competitiveness of the conventional solid oxide co-electrolysis technique.

When the co-electrolysis process is performed in the CG assisted mode as described in reaction (2.06), the total energy decreases 41% from the conventional mode of 528 to 310 kJ mol^{-1} . Moreover, it is noticeable that the electrical energy demand ΔG reduces dramatically with temperature. When the temperature reaches 1000 K , the ΔG becomes a negative value, suggesting that the CG assisted co-electrolysis reaction can occur spontaneously without any external electrical input.

Furthermore, compared with the conventional mode, operational voltage window of the system is much broader in the CG assisted mode, because the gap between thermal neutral voltage (E_{tn}) and reversible voltage (E_{re}) is larger in the CG assisted mode. Larger gap between E_{tn} and E_{re} makes electrolysis more flexible and efficient. The thermal neutral voltage E_{tn} and the reversible voltage E_{re} in different modes are shown in Fig. 2.03. It can be seen that in both modes, E_{tn} has a small dependence on temperature, while E_{re} decreases considerably with increasing temperature, leading to larger values of $E_{tn} - E_{re}$ at higher temperatures. Compared with the conventional mode, E_{re} is much smaller in the CG assisted mode, resulting in larger gap between E_{tn} and E_{re} . Consequently, the operational window of electrolysis ($E_{tn} - E_{re}$) is wider in the CG assisted mode. For instance, at 1123 K , the

E_{tn} is 1.374 V in the conventional co-electrolysis mode, which is larger than that of the CG assisted mode (0.791 V). However, the E_{re} of CG assisted mode (-0.133V) is much smaller than that of the conventional mode (0.961 V). As a result, the value of $E_{tn} - E_{re}$ in the CG assisted mode (0.924 V) is larger than that in the conventional mode (0.583 V), leading to larger operational window in the CG assisted mode.

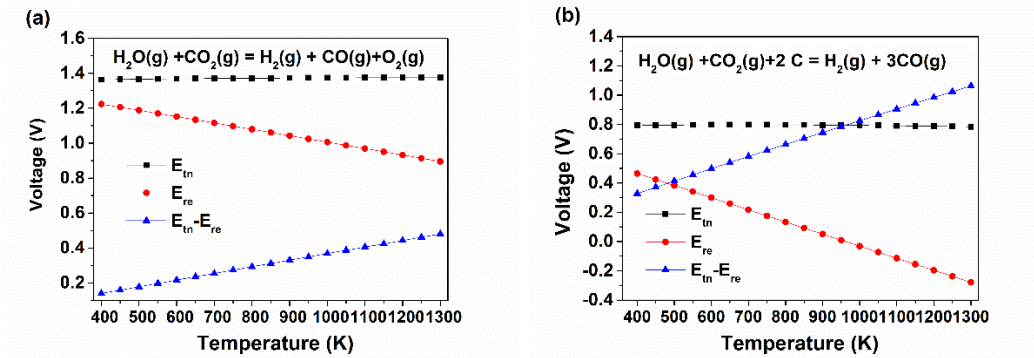


Figure 2.03 Calculated E_{re} and E_{tn} as a function of temperature for co-electrolysis process in the (a) conventional mode, and (b) CG assisted mode.

In thermodynamic term, the CG-assisted electrolysis reaction is identical to carbon gasification using steam and CO_2 as gasifying agents. However, there are several unique merits when it is performed in SOECs. The key point is that it is an electrical energy to chemical energy conversion on a solid oxide cell, which can also be directly used to generate electricity when operating in fuel cell mode. Thus the solid oxide cell can serve as load levelling and energy storage between electricity and fuel. Moreover, in the CG assisted electrolysis cell, the reaction and conversion rate of the gasification reaction can be controlled and managed by the applied current density. In addition, the design of the CG assisted electrolysis cell is flexible. It can be implemented as distributed syngas generation device under atmospheric pressure, while carbon gasification generally operates as large chemical plants in pressurized

operation. The CG assisted electrolysis cell can also be implemented in large scale chemical plants or coal-based power plants. Lastly, because of the separation of carbon and gas agent in the CG assisted electrolysis cell, clean and pure syngas without contaminants such as H_2S and N_xO_y can be produced in the hydrogen electrode so that dirty fuels such as coal can be potentially converted to green and clean fuels.

2.3.2 ELECTROCHEMICAL TEST OF THE CONVENTIONAL AND CG ASSISTED CO-ELECTROLYSIS

To evaluate the feasibility of CG assisted co-electrolysis technique, symmetrical cells, SFM-SDC/LSGM/SFM-SDC, that can work in both the conventional mode and the CG assisted mode are fabricated and investigated to exclude the influence of material composition and microstructure of cell components from different cells. SFM is chosen for its good electrical properties and excellent redox stability [67]. It has been used as symmetrical electrode material in SOFC mode and SOE mode [68-70]. SDC is incorporated to increase the electrode ionic conductivity, and consequently improve the cell performance due to enlarged active reaction sites [71, 72]. Shown in Fig. 2.04 (a) is the cross section microstructure image of the electrolysis cell, with symmetrical tri-layers structure. The LSGM electrolyte support layer, after sintered at 1723 K for 5h, is relatively dense. Fig. 2.04 (b) displays that the porous SDC-SFM electrode is well adhered to the electrolyte after sintering at 1373 K for 2 h.

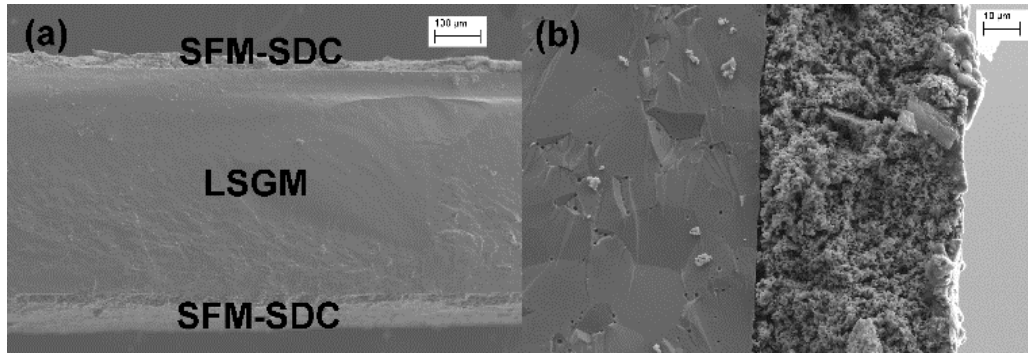


Figure 2.04 The microstructure of single cell (a) SFM-SDC/LSGM/SFM-SDC triple layers; (b) interface of SFM-SDC and LSGM.

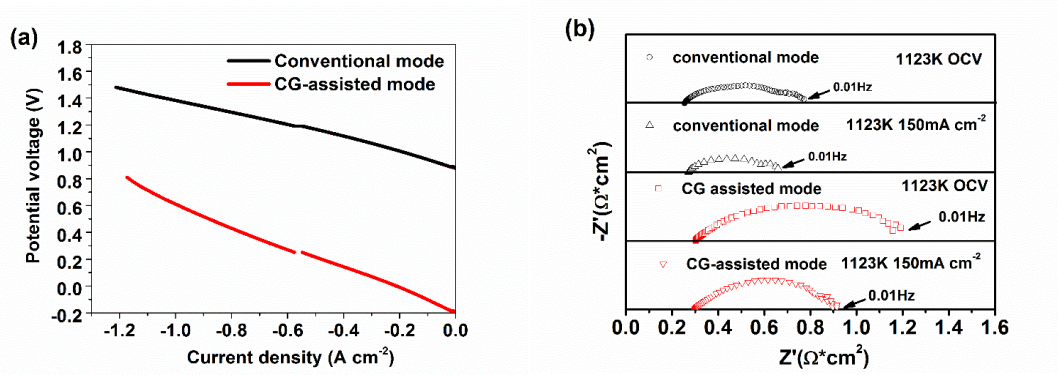


Figure 2.05 (a) I - V curves for the electrolysis cells operated in conventional mode and CG assisted mode at 1123K; (b) impedance spectra for electrolysis cells operated in four different conditions.

The I - V curves of the CG assisted mode and the conventional mode are shown in Fig. 2.05 (a). It can be seen that at 1123 K, the OCV of the CG-assisted mode is -0.202 V, indicating that electrolysis in the CG-assisted mode is spontaneous (i.e., it is generating electricity), while the voltage needed for the electrolysis process of the conventional mode is 0.877 V. It is noted that in order to enhance the electrode kinetics and have relatively high electrolysis current density in practical applications, an external electricity input is needed for the CG assisted mode even at an operating temperature higher than 1123 K. However, it can be seen that the I - V curve measured under the CG assisted mode totally

stays below the one measured under the conventional mode, indicating that a much lower voltage is required to produce the same electrolysis current density. For example, the cell voltage to produce electrolysis current density of 0.4 A cm^{-2} is 0.9 V for the conventional mode; while the required voltage has been decreased dramatically by nearly one order of magnitude to 0.14 V when the cell is operated under the CG-assisted mode. Lower OCV means lesser potential barrier to split H_2O or CO_2 in the CG-assisted mode.

Electrochemical impedance spectra are measured in four different conditions, as shown in Fig. 2.05 (b). The intercept of the real axis at high-frequency corresponds to ohmic resistance of the cell, while the real axis range covered by the arc at lower frequency region represents the overall electrode polarization resistance, including both the air electrode and hydrogen electrode polarization resistances. The total resistance is the sum of the ohmic resistance and the polarization resistance. As to the ohmic resistance of a cell, it is the sum of the ohmic resistances of the air electrode, the electrolyte layer, the hydrogen electrode, and the contact resistance between each two adjacent layers. From Fig. 2.05 (b), it can be seen that the intercept of the real axis is very similar in four different measurement conditions, indicating that the cell ohmic resistance is almost the same. Since the ohmic resistance is mainly determined by the condition of the electrolyte in electrolyte-supported cells, the similar ohmic resistances can be explained by the identical fabrication process of the LSGM electrolyte in all cells tested.

In the conventional mode, the polarization resistance under 150 mA cm^{-2} ($0.389 \Omega \text{ cm}^2$) is smaller than that under OCV ($0.517 \Omega \text{ cm}^2$), suggesting that the reaction rate can be enhanced with applied current. Comparing the polarization resistance under OCV in the conventional mode and the CG assisted mode, the former ($0.517 \Omega \text{ cm}^2$) is smaller than the

latter ($0.890 \Omega \text{ cm}^2$), which is possibly due to the introduction of the CG process in the air electrode side (The major gas component in the air electrode side is found to be CO as shown in Fig. 2.06). In the air electrode side of CG assisted mode, the produced O^{2-} is consumed by reacting with CO to form CO_2 ($\text{O}^{2-} + \text{CO} = \text{CO}_2 + 2\text{e}^-$). The larger polarization resistance may be caused by the sluggish electrochemical reactivity of CO or the slow rate of “CO shuttle”. Similar to the conventional mode, in the CG assisted mode, the polarization resistance reduces to $0.71 \Omega \text{ cm}^2$ when 150 mA cm^{-2} is applied. The larger polarization resistance of the CG assisted mode indicates a larger polarization loss. However, since the significant decrease in the open circuit voltage (i.e., a significant reduction of potential barrier), a much lower overall electrolysis voltage is still achieved for the CG assisted mode for the same current density compared with the conventional mode. Consequently, the consumption of electrical energy can be reduced in the CG assisted mode.

2.3.3 THE ANALYSIS OF CARBON GASIFICATION PROCESSSS IN THE AIR ELECTRODE SIDE

As shown in Fig.2.01, in the air electrode side of the CG assisted mode, carbon source is introduced. Assuming that the amount of carbon is much larger than that of O_2 , the gas atmosphere in the air electrode side under thermodynamic equilibrium condition can be calculated by HSC 6.0 software, as displayed in Fig.2.06 (a). Between 600 and 800 K, CO_2 is the major product, while between 973 K and 1173 K (operation temperature of the CG assisted co-electrolysis in this study), CO becomes the predominant product, suggesting that CO can be obtained in the air electrode side of this system.

Besides the thermodynamic factors, the kinetics of carbon gasification should also be taken into consideration, because it is crucial for the rate of “CO shuttle” between the solid carbon and the air electrode, which influences the performance of SOEC. Consequently, the kinetics of carbon gasification in air and CO₂ were studied by thermogravimetric analysis, as shown in Fig. 2.06 (b). From the TG and DTG curves, it can be seen that weight loss of carbon starts at approximately 600 K in the air, while weight loss only starts at about 850 K in CO₂, indicating that carbon has higher reactivity with O₂ than with CO₂. This result also reveals that below 850 K, the major product of O₂ and carbon is CO₂, consistent with the thermodynamic calculation analysis.

Above 1000 K, the DTG curve (carbon in CO₂) shows that the reactivity of carbon with CO₂ increases greatly with increasing temperature and reaches the maximum at 1200 K. Therefore, at 1123 K (the operating temperature of SOEC in this study), the reactivity of carbon with CO₂ is not at the fastest condition. The sluggish reaction could be one of the reasons for the larger polarization resistance of the CG assisted co-electrolysis than that of the conventional co-electrolysis observed in Fig. 2.05 (b). As the reaction rate increases with increasing temperature, the polarization resistance of the CG assisted co-electrolysis can be reduced by further increasing the operation temperature.

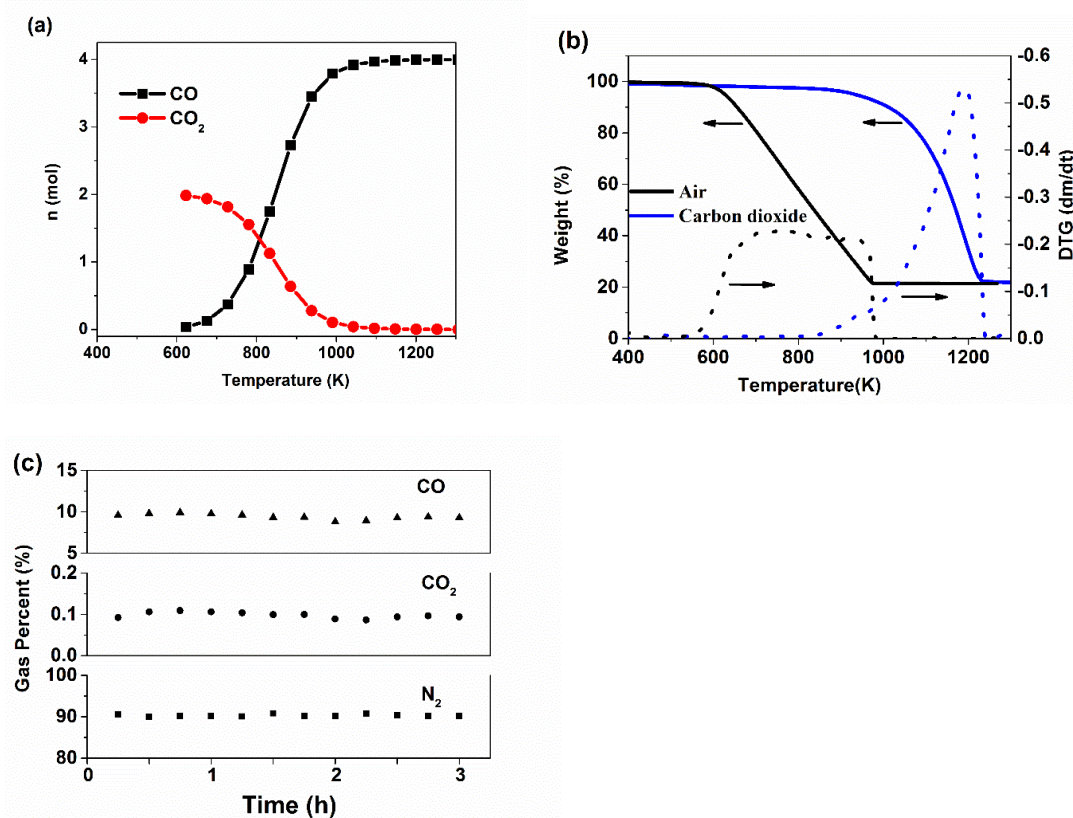


Figure 2.06 (a) Thermodynamic equilibrium calculation results for the reaction of 2 mol O₂ with 98 mol carbon at different temperatures; (b) TG and DTG of carbon source in air and CO₂ condition; (c) the exhaust gas composition in the air electrode side.

Fig. 2.06 (c) presents the exhaust gas composition in the air electrode side analyzed by GC with 5 ml min⁻¹ N₂ as sweep gas when the device is operated with a constant current density of 300 mA cm⁻². Besides N₂ from the sweep gas, the exhaust gas contains ~10% CO and very small amount of CO₂ (about 0.1%). Thus the gas generated in the air electrode side is predominantly CO at the operating temperature (1123 K), which is consistent with the results from thermodynamic calculation. It also demonstrates that “CO shuttle” works continuously in the air electrode side.

2.3.4 ELECTRICITY CONSUMPTION AND ENERGY EFFICIENCY

Compared with heat and carbon sources, electricity is a more valuable energy form. When the electrolysis cell is operated at thermoneutral voltage, only a small amount of extra heat (4% of total energy input) is needed [1]. Furthermore, carbon sources (coal and biomass) are typically cheap and abundant. Since electricity cost is the major contributor for the production cost of syngas, the electrical efficiency plays a decisive role in determining the economic competitiveness of this system.

Electricity input per unit of syngas production when the electrolysis cell is operated at -0.4 A cm^{-2} is compared in different mode in Table. 2.01. In the CG assisted mode, the total electrical energy needed is 13.8 kJ, which is even smaller than 1/15 of the conventional mode (216 kJ). This substantial reduction in electricity consumption is due to two reasons. On one hand, the portion of electrical energy for overcoming the potential barrier is much smaller in the CG assisted mode compared with that in the conventional mode. On the other hand, CO can be produced in the air electrode side of the CG assisted mode. Consequently, more CO can be produced in the CG assisted mode for the same amount of electricity consumed.

Although it has been shown that the introduction of carbon gasification in the air electrode side can reduce the potential barrier and electricity consumption of SOECs, the introduction of carbon source increases the input energy and the CG process may lead to useful energy losses since some portion of the chemical energy from carbon is converted into heat instead of electricity or chemical energy stored in the syngas. Consequently, it is also necessary to evaluate the energy efficiency

defined as how much energy is converted to the desirable product [73-75]. The energy efficiency can be evaluated by the ratio of energy output and energy input.

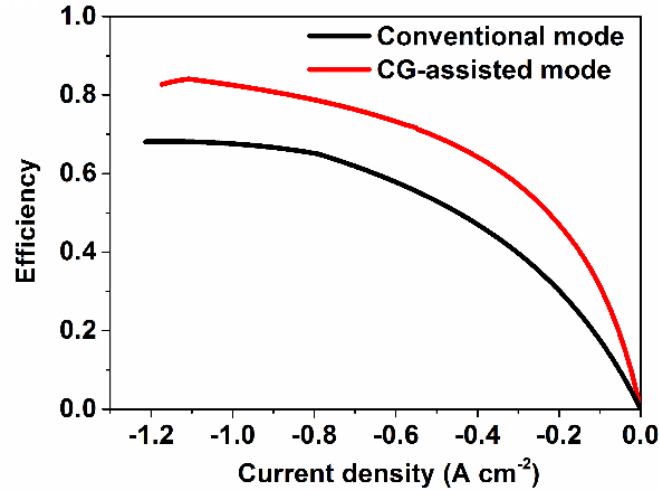


Figure 2.07 *I*-total energy efficiency curves for the electrolysis cell operated in conventional mode and CG assisted mode at 1123K.

Table 2.01 Comparison of electricity consumption for 1 mole syngas production in the CG assisted and conventional mode.

	Conventional mode	CG assisted mode
Current density (A cm ⁻²)		-0.4
Applied voltage (V)	1.12	0.143
Electrical power (W)	0.448	0.0572
Electrical energy (kJ)	216	13.8

The results of efficiency calculation for both modes are shown in Fig.2.07. The efficiency of the conventional mode increases significantly below 0.4 A cm⁻² and rises steadily when the current density exceeds about 0.8 A cm⁻². This trend is similar to that in the solid oxide steam electrolysis cells [73]. The efficiency curve of the CG assisted mode

displays a similar trend, but it is always above the one in the conventional mode. For instance, at an electrolysis current of -0.4 A cm^{-2} , the efficiency of the CG assisted mode (0.64) is 36% higher than that in the conventional mode (0.47). This demonstrates that the introduction of carbon gasification in the air electrode side significantly improves the total energy efficiency of the co-electrolysis.

2.4 CONCLUSIONS

In summary, we have demonstrated the feasibility of a novel and efficient syngas generator (CG assisted co-electrolysis), in which the carbon gasification and the co-electrolysis are synergistically combined. Compared with the conventional SOECs, the significant distinction of the CG assisted co-electrolysis is the introduction of carbon gasification process in the air electrode side which can reduce the potential barrier by about 1 V. The most significant point is that the consumption of electrical energy is substantially reduced and the total electrical energy efficiency is significantly increased. Moreover, the operational voltage window is larger in the CG assisted mode. Therefore, CG assisted co-electrolysis shows great promise for eco-friendly and efficient utilization of coal/biomass and CO_2 to store energy and reduce the emission of CO_2 .

CHAPTER 3 THE CO-ELECTROLYSIS OF CO₂-H₂O TO METHANE VIA A NOVEL MICRO-TUBULAR ELECTROCHEMICAL REACTOR

3.1 BACKGROUND

Co-electrolysis of steam and CO₂ in SOECs is a promising solution to convert CO₂ and H₂O to syngas for energy storage [1, 31, 43, 76-79]. The produced syngas can be subsequently used as feedstock through the well-established Fischer-Tropsch (F-T) process to produce hydrocarbons [1, 80]. In recent years, two-step system which separates the SOECs and conventional F-T reactor has been studied extensively. Graves *et al.*[81] has compared many possible technological pathways for recycling CO₂ into fuels using renewable or nuclear energy and concluded that SOEC is one of the most promising and feasible routes to use CO₂ and H₂O to produce syngas, followed by converting syngas to gasoline in F-T reactor. Becker *et al.* [82] has developed a model for syngas production by SOEC and subsequent conversion to liquid fuels by a F-T process, predicting up to 54.8% higher heating value (HHV) overall system efficiency for liquid hydrocarbon fuels. However, the above-mentioned design of two separated steps has an inherent limitation: long gas transport networks connecting two separated processes leads to extra cost and large heat dissipation losses [83]. Therefore, integration of SOEC and F-T processes in a single unit can potentially reduce the investment and increase the energy efficiency of combined system. However, effective integration of these two processes meets significant

technical challenges due to the difference in operating conditions. The typical operating temperature of SOEC is from 873 K to 1273 K [7, 8], while F-T process is often conducted at 473~673 K [84].

Xie *et al.* [36] have reported that co-electrolysis of H₂O-CO₂ and *in situ* F-T synthesis can be combined in an electrolyte-supported planar SOEC, but the CH₄ yield is very low (0.2%) due to the insufficient electrocatalytic reaction area and inadequate reaction condition for the methanation. A similar CH₄ yield of 0.286% was reported with hydrogen electrode supported planar SOEC by Li *et al.*[85]. Although the feasibility of direct synthesis of hydrocarbons through integration of H₂O-CO₂ co-electrolysis and methanation process has been proven in these studies, CH₄ yield is significantly low and it has to be greatly improved for practical application. Recently, we have integrated SOEC and methanation processes in a single tubular unit with 0.42 cm outer diameter and 0.35 cm inner diameter, in which these two processes are realized due to the existence of temperature gradient, resulting in a significant enhancement in CH₄ yield of 11.84% [86]. Based on the above design, a 2D model has recently been developed to optimize the operating condition of the system, such as ratio of H₂-CO in the inlet gas stream, electrolysis voltage, and operating temperature [83]. However, the influence of the diameter of tubular SOEC on the device performance has yet to be investigated.

Micro-tubular solid oxide electrolysis cells (MT-SOECs) have recently been extensively studied for H₂O electrolysis, CO₂ electrolysis and H₂O-CO₂ co-electrolysis[83, 87-92]. Compared with conventional tubular SOEC, MT-SOECs with outer diameter smaller than 2 mm can provide greater thermal shock resistance, larger electrode area per unit volume and higher volumetric factor. Therefore, in this chapter, integration of co-

electrolysis and methanation process in a single micro-tubular reactor has been implemented for the first time to further enhance the CH₄ yield. The electrochemical behaviour of the electrolysis process and catalytic behaviour of the methanation process are evaluated. The effect of the inlet gas composition on the CH₄ yield and CO₂ conversion rate is also studied.

3.2 EXPERIMENTAL

3.2.1 FABRICATION OF MICROTUBULAR REACTORS

Nickel oxide-yttria-stabilized zirconia (NiO-YSZ) hollow fibers were fabricated via a combined extrusion and phase-inversion method [93, 94]. NiO (JT Baker, USA) and YSZ (8 mol% yttria-stabilized zirconia, Tosoh Corporation, Japan) powders were used in this study. The prepared hollow fibers were pre-sintered at 1373 K for 2h. YSZ film was then coated on the pre-fired NiO-YSZ hollow fibers by a dip-coating method [95] and then co-sintered at 1723 K for 5 h with a heating and cooling rate of 2 K min⁻¹. YSZ-LSM ((La_{0.8}Sr_{0.2})_{0.95}MnO_{3-δ}, Fuel Cell Materials Inc., USA) electrode was subsequently coated on the surface of the YSZ electrolyte by brush painting, followed by firing at 1373 K for 2 h. The active YSZ-LSM electrode area is 1.0 cm². A silver grid was printed on the surface of the LSM-YSZ electrode as current collector, and silver wires were used as current leads.

3.2.2 CHARACTERIZATION

The microstructure of the micro-tubular reactor was examined using a scanning electron microscope (SEM, Zeiss Ultra Plus FESEM, Germany). The cell performance evaluation was carried out in a home-built high-temperature micro-tubular reactor setup, as schematically shown in Fig. 3.01. For testing in the fuel cell mode, humidified H₂ (3 vol.% H₂O) was introduced to the Ni-YSZ electrode side. For testing in the co-electrolysis

mode, H₂, CO₂ and H₂O were fed to the Ni-YSZ electrode side. The cell polarization characteristics, i.e., current-voltage (i-V) curves, and the cell electrochemical impedance spectra (EIS) were recorded on an electrochemical test system (Versa STAT 3-400, Princeton Applied Research, USA). For the EIS measurement, the frequency range was from 1 MHz to 0.01 Hz with the AC amplitude of 30 mV. The exhaust gas from the Ni-YSZ electrode side was analyzed by a gas chromatograph (7890A, Agilent, USA).

3.3 RESULT AND DISCUSSIONS

3.3.1 WORKING PRINCIPLE AND CHARACTERIZATION

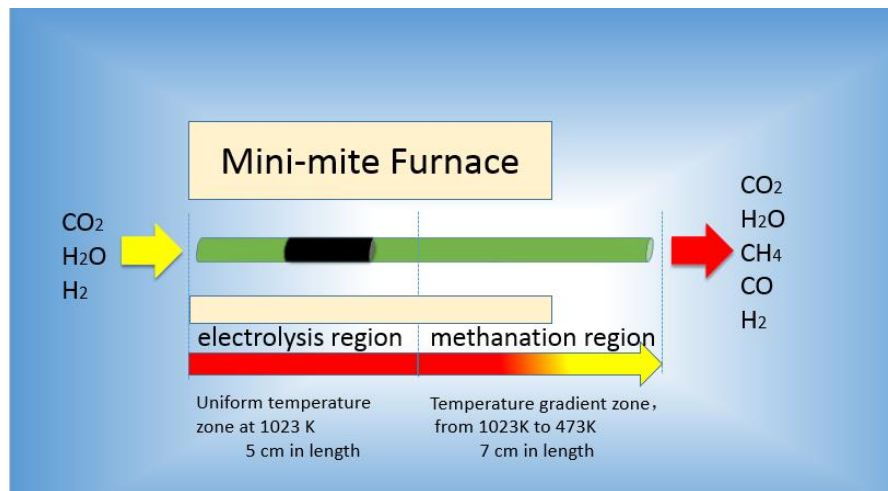
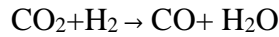


Figure 3.01 Schematic of micro-tubular reactor.

Fig. 3.01 schematically shows the micro-tubular reactor adopted in this study. There are mainly two regions of the micro-tubular reactor: the electrolysis region and the methanation region. A mini-mite furnace is used to provide uniform temperature zone for the electrolysis region. Meanwhile the micro-tubular reactor is extended to the outside of the furnace, where a gradient temperature zone from 573 to 473 K will be formed for the methanation process. In experiment, the temperature in the region of methanation process

is monitored by thermocouples. This design is capable of conducting various reactions as following:

Reverse water gas shift reaction (RWGSR):



(3.01)

Co-electrolysis process:



And methanation:



Reaction (3.04) and (3.05) are known as the Sabatier process and the reverse methane steam reforming, respectively. Table 3.01 shows the Gibbs free energies of both reactions at different temperatures. It can be seen that the Gibbs free energies of both reactions are all negative, indicating that methanation process can take place spontaneously. From 473 K to 673 K, the Gibbs free energies of the reverse methane steam reforming are more negative than those of the Sabatier process, suggesting that the reverse methane steam reforming is thermodynamically more favorable. Therefore, electrolyzing CO₂ to CO is beneficial for the methanation process.

Table 3.01 Gibbs free energy (kJ/mol) of methanation reactions.

T (K)	CO ₂ + 4H ₂ = CH ₄ + 2H ₂ O (Sabatier process)	CO + 3H ₂ = CH ₄ + H ₂ O (reverse methane steam reforming)
473	-81.029	-102.498
573	-61.158	-78.776
673	-40.596	-54.523

In Fig. 3.02(a), a cross-sectional SEM image of the electrolysis region is shown. The outer diameter of the electrolysis region is about 1.88 mm. It can be seen from Fig. 3.02(b) that the electrolysis region contains three layers, namely: porous Ni-YSZ electrode, dense YSZ electrolyte film and porous LSM-YSZ electrode. The thickness of Ni-YSZ electrode, YSZ electrolyte, and LSM-YSZ electrode are 140 μm , 13 μm , and 30 μm , respectively. The Ni-YSZ support shows sandwich-like microstructure, with finger-like macrovoids near the lumen and outer sides and less porous layer in the middle, which is similar to our previous study [94].

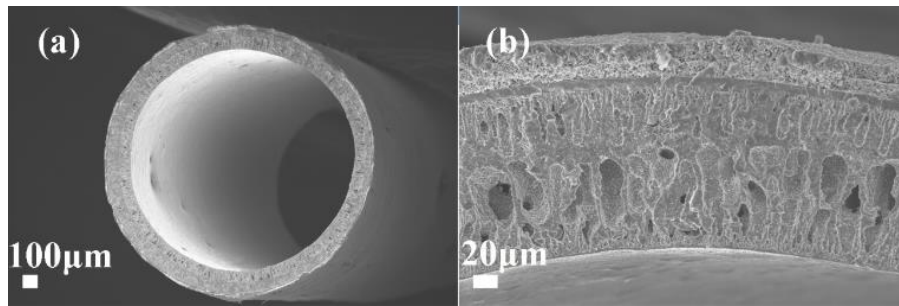


Figure 3.02 Microstructure of micro-tubular reactor, (a) low magnification SEM image of the electrolysis region; (b) high magnification SEM image of the electrolysis region.

3.3.2 ELECTROCHEMICAL TEST

The electrochemical behavior of the micro-tubular reactor in the fuel cell mode is studied, as shown in Fig. 3.03. Fig. 3.03(a) exhibits the voltage-current density relationship recorded at 1023 K. The open circuit voltage (OCV) is larger than 1 V, indicating that the electrolyte layer is reasonably dense, which is consistent with SEM image result shown in Fig. 3.02(b). The maximum power density is about 350 mW cm^{-2} . The impedance spectrum under OCV is shown in Fig. 3.03 (b). The ohmic resistance (R_{Ω}) is about 0.31 $\Omega \text{ cm}^2$, while the polarization resistance (R_p), mainly from the resistance of gas diffusion and gas conversion in the air electrode and hydrogen electrode, is 0.76 $\Omega \text{ cm}^2$, which is more

than twice of R_{Ω} , suggesting that the R_p is the performance-limiting factor. The reason for the large R_p may be due to the sandwich-like microstructure of the Ni-YSZ substrates used in this study. Because of the existence of sponge-like layer in the center of the Ni-YSZ support, as shown in Fig. 3.02 (a) and (b), gas diffusion may be hindered, leading to large gas diffusion resistance. Moreover, the finger-like macro-voids adjacent to the interface between the hydrogen electrode support and electrolyte film may reduce the effective electrochemical reaction sites, i.e., triple phase boundaries (TPBs), resulting in large resistance of gas conversion and increased polarization resistance, consistent with our previous studies [93, 96]. However, the hydrogen electrode support with this sandwich-like microstructure possesses relatively high mechanical strength and excellent thermal shock resistance [94], which is beneficial for mechanical robustness of the micro-tubular reactors for the integrated electrolysis and methanation process, especially in the zone of temperature gradient.

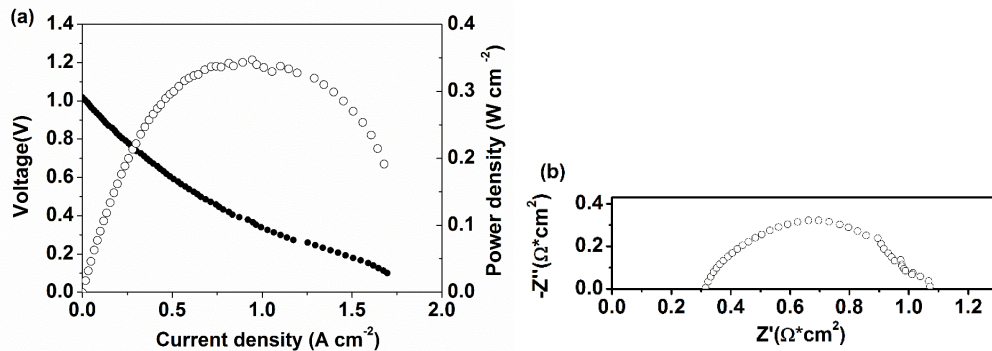


Figure 3.03 Electrochemical test of the electrolysis region in fuel cell mode with H_2 as fuel at 1023 K, (a) I-V curve; (b) Electrochemical impedance spectrum under OCV.

The electrochemical behavior of the micro-tubular reactor in the electrolysis mode is recorded and shown in Fig. 3.04. The flow rate in all cases is 18.75 sccm. In Fig. 3.04 (a), the I-V curves of the co-electrolysis with different ratio of H_2 : CO_2 in the inlet are

presented. It can be found that the absolute current densities increase with the increase of the applied voltage and increasing the concentration of CO₂ in the inlet can improve the electrolysis performance. For example, to obtain a current density of -0.32 A cm⁻², 1.42 V is required in the case of 10.7% CO₂-69.3% H₂-20% H₂O while the required voltage drops to 1.34 V in the case of 32% CO₂-48% H₂-20% H₂O. This can be explained by the more sufficient supply of reactants for electrolysis with higher concentration of CO₂. It has been reported that in the H₂O-CO₂ co-electrolysis, H₂O electrolysis is the dominant process due to the higher adsorption rate of H₂O compared with that of CO₂ and the generation of CO is mainly from the RWGSR [97-99]. However, it has also been reported [25] that the contribution of RWGSR to CO production depends on the operating temperature and inlet gas composition from modeling the co-electrolysis of H₂O and CO₂. Therefore, when the voltage higher than the OCV is applied, H₂O or CO₂ will be electrochemically split to generate H₂ or CO.

The impedance spectra at 1.3 V are shown in Fig. 3.04 (b). In these three conditions, the R_Ω values under 1.3 V are the same (about 0.31 Ω cm²) and also similar to that in the fuel cell mode. Among these three conditions, the R_p of 10.7% CO₂-69.3% H₂-20.0% H₂O is the largest (0.95 Ω cm²), while the R_p of 32.0% CO₂-48.0% H₂-20.0% H₂O is the smallest (0.57 Ω cm²), which is consistent with the trend of the i-V curves, indicating that increasing the CO₂ concentration can decrease the R_p of the electrolysis cell and improve the electrolysis performance.

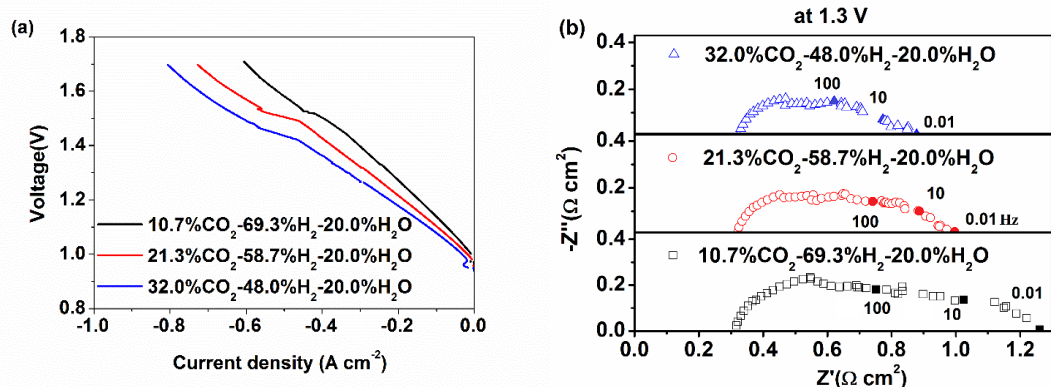


Figure 3.04 Electrochemical test of the electrolysis region in the electrolysis mode at 1023 K, (a) I-V curves; (b) impedance spectra under 1.3V. The inlet steam carrier is 15 sccm CO₂-H₂ with 20 vol% humidity.

3.3.3 ANALYSIS OF GAS COMPOSITION AND STABILITY

The exhaust gases of the micro tubular reactor during different operation condition were analyzed by GC and the results are shown in Fig. 3.05. Because the thermal conductivity detector (TCD) in GC cannot analyze water, the produced water in the exit gas stream in the system was condensed into a container before the exhaust gas stream is fed to GC. Fig. 3.05 (a) shows the gas composition of the exhaust when the inlet gas composition is 10.7%CO₂, 69.3% H₂ and 20.0% H₂O. When the micro-tubular reactor is operated under OCV (a.1), the feed gas flows through the electrolysis region directly without any electrochemical reaction. Subsequently, in the methanation region containing Ni catalyst which is located on the inner wall of micro-tubular unit, H₂ will react with CO or CO₂ to generate CH₄ through the methanation process (Eq.3.04 and 3.05). From the pie chart in Fig. 3.05 (a.1), it can be seen that the percentage of CH₄ is about 12.3±0.3%, while the percentage of CO₂ and CO are 7.1±0.1% and 1.0±0.1% respectively. Besides CH₄, CO₂ and CO, the remaining component of the exhaust is H₂ (79.6±0.6%).

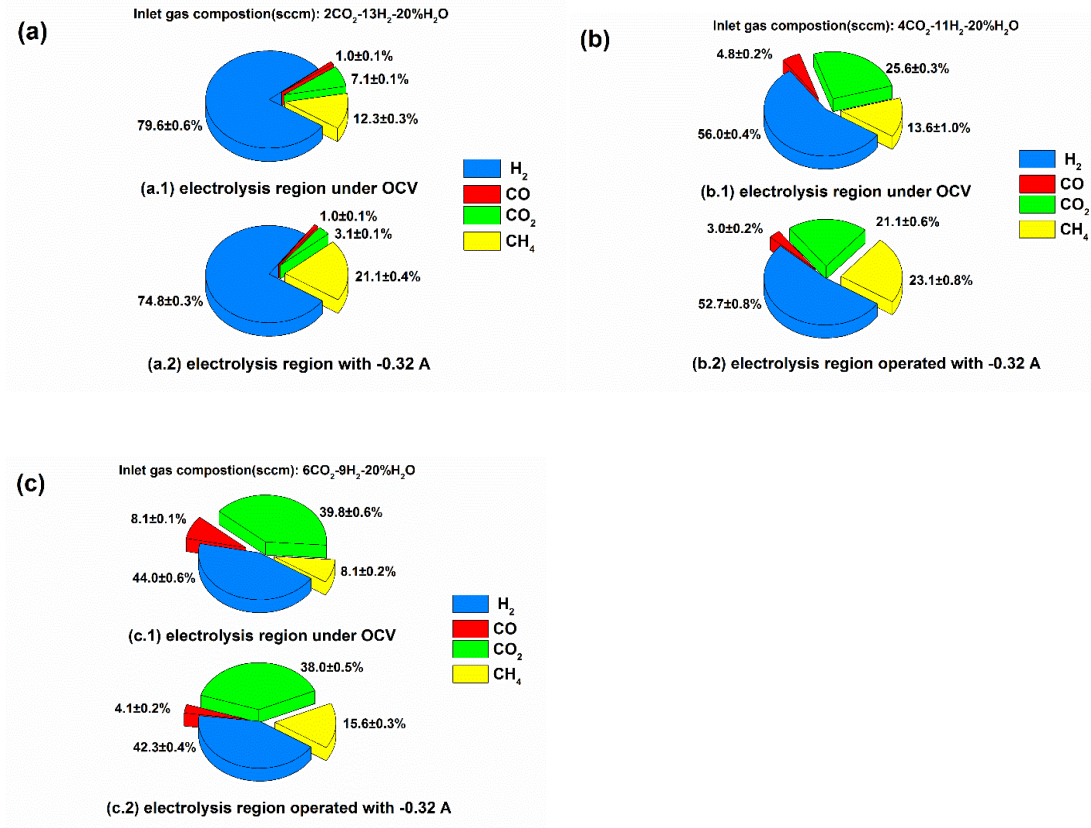


Figure 3.05 Gas composition in the exhaust (a) with the inlet gas composition: 10.7% CO₂-69.3% H₂-20% H₂O; (b) with the inlet gas composition: 21.3% CO₂-58.7% H₂-20.0% H₂O; and (c) with inlet gas composition: 32.0% CO₂-48.0% H₂-20.0% H₂O.

From Fig. 3.05 (a.2), it can be seen that when the micro-tubular reactor is operated under -0.32 A, the CH₄ yield in the exhaust stream increases to 21.1±0.4%, while the CO₂ concentration decreases to 3.1±0.1% and CO concentration remains stable at 1.0±0.1%. During the operation, the feed stream flows through the micro-tubular reactor where electrochemically splitting of H₂O and/or CO₂ and correspondingly generation of H₂ and/or CO take place in the electrolysis region. According to the Faraday's law, assuming 100% current efficiency, a current of -0.32 A will consume 2.23 sccm of H₂O or CO₂ and generate 2.23 sccm of H₂ or CO. Consequently, in the methanation region, the gas in the micro-

tubular reactor will contain more H₂ and CO under a current of -0.32 A, compared with the operation under OCV. The reaction rates (R_{RMSR}) of the reverse methane steam reforming (reaction (3.05)) can be calculated by equation (I) [100]:

$$R_{RMSR} = K_{rf} \left(\frac{p_{CO} p_{H_2}^3}{K_{PR}} - p_{CH_4} p_{H_2O} \right) \quad (I)$$

where K_{rf} and K_{PR} are the reaction constants, p_x is the partial pressure of gas. From equation (I), it can be found that the reaction rate is strongly related to the partial pressure of H₂/CO and less to the partial pressure of H₂O/CH₄. Therefore, compared with the OCV condition, the operation of the electrolysis region under -0.32 A can increase the partial pressure of H₂/CO and decrease the partial pressure of H₂O, resulting in higher CH₄ yield.

Operation condition of the electrolysis region and the CH₄ yield in different studies are compared in Table 3.02. It can be seen that the methane yields in tubular and micro-tubular SOEC (11.84% and 21.1%) are much higher than those in planar cells (0.2%-0.286%), which is attributed to the efficient integration of high temperature co-electrolysis and low temperature methanation processes. Moreover, under the similar applied current (-0.33 A at 1.3V [86] and -0.32 A at 1.42 V in this study), the same inlet gas composition and flow rate (18.75 sccm), the CH₄ yield in micro-tubular reactor (21.1%) is almost twice of that in tubular SOEC (11.84%), which is possibly due to the application of micro-tubular reactor using tubes with smaller diameter. For a tubular unit, the volume of reactant gas inside a tube can be calculated by equation (II):

$$V_{reactant} = \frac{1}{4} \pi d^2 l \quad (II)$$

where d is the inner diameter of the tube, and l is the length of the tube. The catalyst for the methanation reaction is metal Ni in this study, which is located on the surface of the

inner wall of the tube. The catalyst surface area in a tube is proportional to the inner surface area of a tube and can be calculated by equation (III):

$$S_{cata} = \pi d l C \quad (III)$$

where C is a constant related to the surface area of the catalyst and microstructure and thickness of the Ni-YSZ electrode. Therefore, the ratio between S_{cata} and $V_{reactant}$ is equal to $\frac{4}{d}C$. Assuming that the surface area of the catalyst as well as the microstructure and thickness for different Ni-YSZ electrode are similar (i.e., similar C), a smaller d will result in a larger ratio between S_{cata} and $V_{reactant}$, implying more catalyst surface area for a specific volume of reactant. Therefore, the micro-tubular reactor adopted in this study, with small inner diameter (d) micro-tube, provides large catalyst area for the methanation process, resulting in a remarkable enhancement in CH₄ yield rate. Furthermore, according to the definition of space velocity for a reactor (the quotient of the volumetric flow rate of the reactants divided by the reactor volume), the space velocity of micro tubular reactor in this study is 56.3 min⁻¹, which is larger than that in our previous study (16.9 min⁻¹). This indicates that micro-reactor is able to process more reactants in unit time, which is contributed by high volumetric factor of micro-tubular reactor.

To investigate the effect of the inlet gas composition on the CH₄ yield, the ratio of H:C in the inlet is changed from 16.69:1 (10.7%CO₂-69.3%H₂-20%H₂O) to 7.39:1 (21.3%CO₂-58.7%H₂-20.0%H₂O). In Fig. 3.05(b.1), when the inlet gas composition is 21.3%CO₂-58.7% H₂-20.0% H₂O and the electrolysis region is under OCV, the percentage of CH₄ and CO₂ are 13.6±1.0% and 25.6±0.3% respectively. Fig. 3.05(b.2) shows that the operation of the electrolysis region with -0.32 A increases the proportion of CH₄ to 23.1±0.8% and decreases the proportion of CO₂ to 21.1±0.6%.

Table 3.02 Direct synthesis of methane in solid oxide electrolysis cells

Configuration of electrolysis cell	Inlet gas composition (vol.)	Methane yield (%)	Ref.
Planar cell, La _{0.8} Sr _{0.2} TiO _{3+δ} /YSZ/ (La _{0.8} Sr _{0.2}) _{0.95} MnO _{3-δ}	66.7% CO ₂ ,33.3% H ₂ O	0.2	[36]
Planar cell, Ni-ScSZ /ScSZ/ LSM- ScSZ	14.3% CO ₂ ,28.6% H ₂ O, 14.3% H ₂ , 42.8% Ar	0.286	[85]
Tubular cell, Ni-YSZ /YSZ/ LSM- YSZ	11.4% CO ₂ ,68.6% H ₂ , 20.0% H ₂ O	11.84	[101]
Micro tubular cell, Ni-YSZ /YSZ/ LSM- YSZ	10.7% CO ₂ ,69.3% H ₂ , 20.0% H ₂ O	21.1	This study

Table 3.03 CO₂ conversion ratio, CH₄ yield ratio and CH₄ yield rate

Inlet gas composition (sccm)	10.7% CO ₂ , 69.3% H ₂ , 20.0% H ₂ O	21.3% CO ₂ , 58.7% H ₂ , 20.0% H ₂ O	32.0% CO ₂ , 48.0% H ₂ , 20.0% H ₂ O
Operation condition of SOEC	OCV -0.32 A	OCV -0.32 A	OCV -0.32 A
CO ₂ conversion ratio (%)	64.9 87.7	41.9 55.3	28.9 34.2
CH ₄ yield ratio (%)	60.3 83.7	30.9 49.0	14.4 27.0
CH ₄ yield rate (sccm)	1.21 1.67	1.24 1.96	0.87 1.62

In the third condition, the ratio of H:C is reduced to 4.25:1 (32% CO₂-48% H₂-20% H₂O) and the results are displayed in Fig. 3.05 (c). When the electrolysis region is under OCV, CH₄ consists only 8.1±0.2% of the exhaust and CO₂ accounts for 39.8±0.6% of the exhaust.

In Fig. 3.05(c.2), it is found that compared with the electrolysis region under OCV, the operation of electrolysis region with -0.32 A, the proportion of CH₄ in the exhaust almost doubles (15.6±0.3%), but the proportion of CO₂ is only slightly reduced to 38.0±0.5%.

According to the results shown in Fig. 3.05, CH₄ yield and CO₂ conversion ratio are calculated. The CH₄ yield ratio can be calculated by equation (IV):

$$CH_4 \text{ yield ratio} = \frac{[CH_4]}{[CH_4]+[CO]+[CO_2]} \quad (IV)$$

And the CO₂ conversion ratio can be calculated by equation (V):

$$CO_2 \text{ conversion ratio} = \frac{[CH_4]+[CO]}{[CH_4]+[CO]+[CO_2]} \quad (V)$$

And the CH₄ yield rate (sccm) can be calculated by equation (VI):

$$CH_4 \text{ yield rate} = \frac{[CH_4]}{[CH_4]+[CO]+[CO_2]} \times V_{CO_2} \quad (VI)$$

where, [X] (X=CH₄, CO, CO₂) is the percentage of gas and V_{CO₂} is the flow rate of CO₂ in the inlet, respectively.

The calculated results under different operation conditions are compared in Table 3.03. In all the cases, it is clear that compared with the electrolysis region under OCV, the operation of electrolysis region with -0.32 A can improve the CO₂ conversion ratio, the CH₄ yield ratio and the CH₄ yield rate. The maximum CO₂ conversion ratio (87.7%) and CH₄ yield ratio (83.7%) are achieved in the case of 10.7%CO₂-69.3%H₂-20.0% H₂O and -0.32 A. However, increasing the concentration of CO₂ results in a decline of the CO₂ conversion ratio as well as the CH₄ yield ratio. In terms of the CH₄ yield rate, with an applied current of -0.32A, 1.67 sccm and 1.62 sccm of CH₄ are produced in the case of 10.7%CO₂-69.3%H₂-20.0%H₂O and 32.0%CO₂-48.0%H₂-20.0%H₂O, respectively, which are smaller than that (1.96 sccm) of 21.3%CO₂-58.7% H₂-20.0% H₂O. When the H:C ratio

is decreased from 16.69:1 to 7.39:1 and then to 4.25:1, CH₄ yield rate increases with the decrease in the H:C ratio, reaching a maximum, and then decreases with further decrease in the H:C ratio. This trend is consistent with the modeling results [100], which can be explain by the “CO starvation” in the methanation section at high ratio of H:C and “H₂ starvation” in the methanation section at low ratio of H:C.

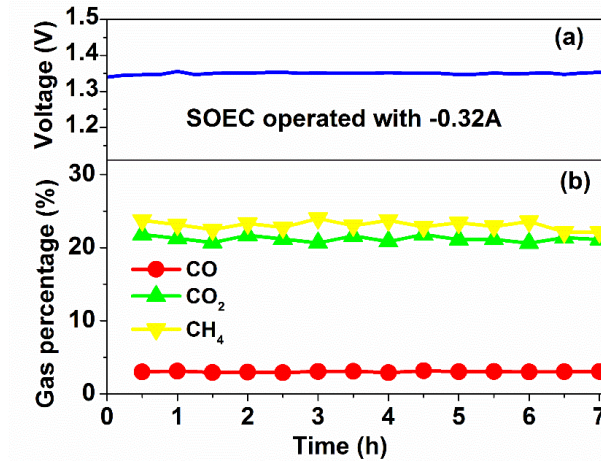


Figure 3.06 Short term stability of the micro-tubular reactor (a) stability of the electrolysis region and (b) the gas composition in the exhaust.

Fig. 3.06 shows the short-term stability of the micro-tubular reactor in the case of the inlet gas stream of 21.3%CO₂-58.7% H₂-20.0% H₂O under an electrolysis current of -0.32 A. When the constant current of -0.32 A is applied, the cell is relatively stable at 1.35 V during the operation. From Fig. 3.06 (b), it can be seen that the percentage of CH₄ in the exhaust stream is stable at about 23.1% and the proportion of CO₂ and CO is relatively stable at 21.1% and 3.0%, respectively.

To check whether there is any coking problem of the Ni-YSZ substrate in the methanation region and the electrolysis region, microstructure of the Ni-YSZ substrate before and after the stability test is characterized by SEM, as shown in Fig. 3.07. The

morphology of the Ni-YSZ substrate is unchanged before and after the stability test. Furthermore, as shown in Fig. 3.07(b) and 3.07(c), there are no observable deposition of amorphous carbon or fiber carbon on the surface of the Ni-YSZ substrate, suggesting that coking is not an issue for the Ni-YSZ substrate in both the methanation region and the electrolysis region. This is consistent with stable CH_4 yield in Fig. 3.06 (b).

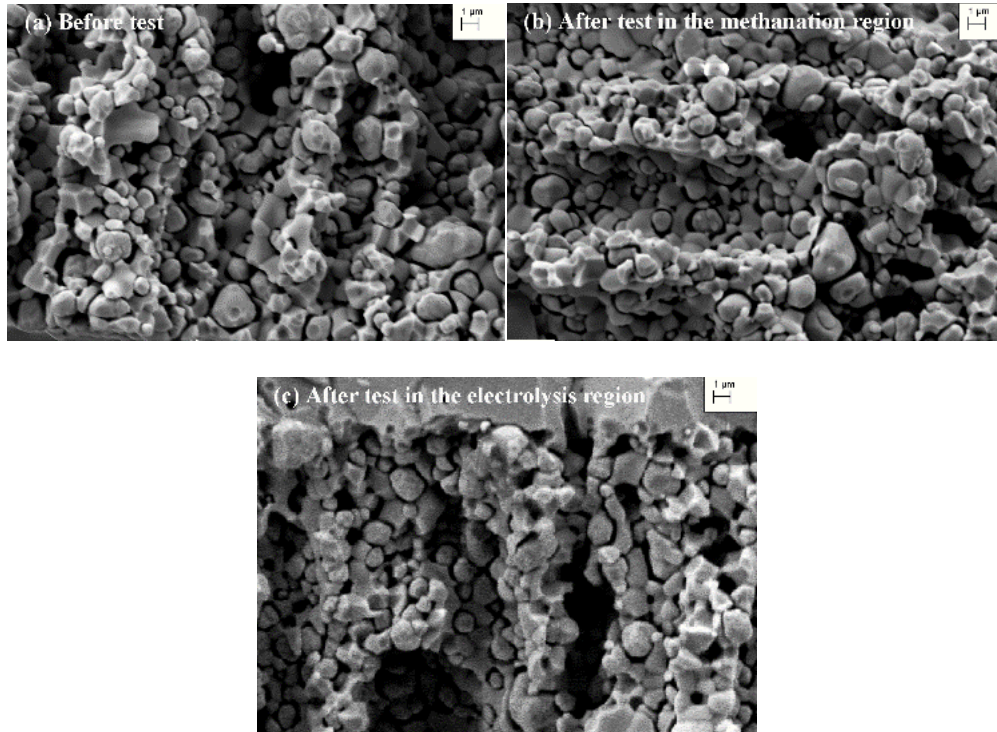


Figure 3.07 SEM images of the Ni-YSZ substrate (a) before the stability test; (b) after the stability test in the methanation region and (c) after the stability test in the electrolysis region.

3.4 CONCLUSIONS

In this work, high temperature co-electrolysis and low temperature methanation processes are successfully combined into a single micro-tubular reactor. Direct synthesis of CH_4 is realized from electrolysis of CO_2 - H_2O . Because the micro-tubular reactor can provide large catalyst area for specific volume of the reactant gas, a remarkably enhanced CH_4 yield, up to 21.1%, can be achieved, along with CO_2

conversion ratio of 87.7%, when the inlet gas stream is 10.7% CO₂-69.3% H₂-20.0% H₂O and the electrolysis region is operated with a current of -0.32 A. This novel design provides an alternative way for CO₂ utilization and energy storage. Furthermore, it is found that decreasing the ratio of H:C in the inlet gas stream leads to a decline in the CO₂ conversion ratio and the CH₄ yield ratio, respectively. Among the conditions studied in the work, the highest CH₄ yield rate (1.96 sccm) is obtained when the inlet gas stream is 21.3% CO₂-58.7% H₂-20.0% H₂O and the electrolysis region is operated with -0.32 A, which is due to the proper ratio of reactants for the methanation reaction.

CHAPTER 4 INTERMEDIATE-TEMPERATURE SOLID OXIDE ELECTROLYSIS CELLS WITH THIN PROTON-CONDUCTING ELECTROLYTE AND ROBUST AIR ELECTRODE

4.1 BACKGROUND

Renewable and clean energy supplies, such as solar, wind, tidal and hydropower, are developed rapidly around the world. However, the site-specific and intermittent nature of these renewable and clean energy sources do not always meet the market needs. In order to maintain a continuous and sustainable energy supply to match with consumers' demand, durable and affordable large scale electricity storage is indispensable[18]. One efficient way for electricity storage is to convert electricity to fuel (energy carriers) such as hydrogen, through electrolysis. Solid oxide electrolysis cells (SOECs) at elevated temperatures are attracting the highest attention because they can benefit from reduced electricity consumption and do not need noble metal catalysts[7, 9, 17, 25, 79, 102, 103].

The state-of-the-art SOECs are the reversed operation of solid oxide fuel cells (SOFCs), comprising of an oxygen-ion conducting electrolyte of YSZ (yttria-stabilized zirconia), a hydrogen electrode of YSZ-Ni cermet, and an air electrode of mixed ionic and electronic conducting (MIEC) oxides[102, 104]. However, the typical high operating temperature of 1023-1273 K results in high performance degradation rate in the range of 1-4%/1000h and high material cost. Furthermore, the Ni-based fuel electrolyte tends to be oxidized by steam in oxygen-ion-conducting SOECs (O-SOECs), leading to cell

performance degradation[105, 106]. Most significantly, the air electrode has been observed to delaminate due to elevated oxygen pressures at the electrolyte/air electrode interface[21]. The intermediate temperature (IT) SOECs (773-973 K) have gained much attention recently since they can potentially improve durability, reduce materials issues, increase nanostructure stability, expand heat source choice, reduce BOP cost, and improve system efficiency. The well-known IT oxygen-ion conducting electrolytes of doped CeO_2 and $\text{La}_{0.9}\text{Sr}_{0.1}\text{Ga}_{0.8}\text{Mg}_{0.2}\text{O}_{3-\delta}$ (LSGM) have been tested for IT-SOECs. However, LSGM is suffering serious reactions with both Ni on the fuel electrode and MIEC oxide on the air electrode[7]. The doped CeO_2 is suffering high electronic leakage due to the reduction of Ce^{4+} to Ce^{3+} at high electrolysis potential[7]. Compared with oxygen ion conductors, proton-conducting electrolytes, typically ABO_3 (A=Ba, Sr; B=Ce, Zr) perovskite-type oxides[7, 9, 18] offer some unique advantages for SOECs. First, proton conductor shows higher ionic conductivity than that of ceria-based oxygen ion conductor in the intermediate temperature range[107]. Lowering the operation temperature of SOECs can reduce the manufacture and materials cost of the SOEC system, have wider material choices for interconnects and seals, and mitigate the stability issues caused by the high operation temperature[108]. Second, since hydrogen is evolved from the fuel electrode while the electrolyte/fuel electrode is typically co-sintered and has a strong interface, this helps mitigate the electrolyte/electrode delamination problems often found for O-SOECs. Third, from a system perspective, the O-SOECs with the oxygen-conducting electrolyte are further challenged by the fact that the primary H_2 product must be subsequently separated from water/ H_2 mix that flows from the fuel electrode exhaust. However, in proton-conducting SOECs (H-SOECs) with proton-conducting electrolyte, steam is fed from the

air electrode side while pure and dry hydrogen is produced at the fuel electrode side. Thus, the gas separation step is not needed, which can simplify the system and reduce the cost of operation[109].

Although H-SOECs have the above-mentioned unique merits over O-SOECs, the development of H-SOECs is far behind that of O-SOECs, due to some critical technical challenges. The electrolyte material is required to be stable in H₂O-containing atmosphere in the operating conditions. However, proton-conducting cerate oxides, which are the most-widely investigated material for proton-conducting solid oxide fuel cells (H-SOFCs), have been shown to be chemically unstable in H₂O-containing atmosphere both thermodynamically[13] and experimentally[14] at typical cell operating conditions. Even partial Zr-doping for cerates cannot completely stabilize the proton conducting cerates in H₂O-containing atmosphere[15, 16]. On the contrary, proton-conducting zirconate oxides have been proven to be chemically stable in H₂O-containing atmosphere[17, 18], making them the choice electrolyte for H-SOECs. However, the high grain boundary resistance and the poor sinterability of proton-conducting zirconate oxides constrain their development[16, 110-113].

To the best of our knowledge, there have been very limited studies on H-SOECs with zirconate proton conducting electrolyte. Recently, Bi et al.[17] have reported that H-SOECs with BZY (BaZr_{0.8}Y_{0.2}O_{3-δ}) thin electrolyte and LSCF (La_{0.6}Sr_{0.4}Co_{0.2}Fe_{0.8}O_{3-δ})-BZY air electrode show promising electrolysis performance. However, LSCF is the conventional air electrode material for SOFC and its stability in H₂O-containing atmosphere is a serious concern, especially at intermediate temperature range of 773-973 K[27, 114].

$\text{Sr}_2\text{Fe}_{1.5}\text{Mo}_{0.5}\text{O}_{6-\delta}$ (SFM), a redox stable perovskite[67] has been evaluated as symmetrical electrode material in O-SOECs for H_2O electrolysis and $\text{H}_2\text{O}-\text{CO}_2$ co-electrolysis[67, 70, 79, 115] and shown stable and promising cell performance. Therefore, in this chapter, H-SOECs, with robust SFM-BZY air electrode, thin BZY electrolyte and Ni-BZY fuel electrode, are fabricated and characterized, as shown in Fig. 4.01. 1wt.% NiO is added to the thin BZY electrolyte as sintering aid to improve the sinterability of BZY.

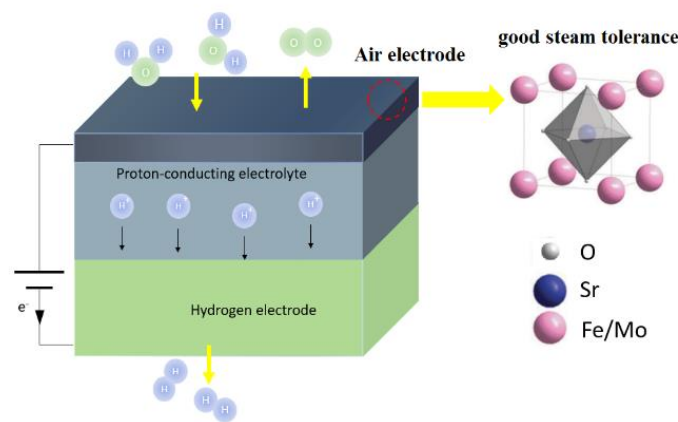


Figure 4.01 Schematic of proton conducting solid oxide electrolysis cell with SFM as the air electrode.

4. 2 EXPERIMENTAL

4.2.1 SYNTHESIS AND CHARACTERIZATION OF MATERIALS

The SFM powders were synthesized by a glycine and citric acid assisted combustion method[67]. Stoichiometric amounts of salt solution precursors $\text{Sr}(\text{NO}_3)_2$ (Alfa Aesar 99%), $\text{Fe}(\text{NO}_3)_3$ (Alfa Aesar 99%) and $(\text{NH}_4)_6\text{Mo}_7\text{O}_{24}\cdot 4\text{H}_2\text{O}$ (Alfa Aesar 99.9%) were mixed together. Glycine and citric acid were added to the solution as the chelating agent and combustion-assisting chemicals. The precursor solution was subsequently heated on a hot plate until self-combustion occurred. The as-prepared ash was heat-treated at 1323 K for 5 h to form the perovskite structure.

The BZY powders were synthesized by a combined EDTA-citric acid method[116]. Metal nitrate precursors $\text{Ba}(\text{NO}_3)_2$ (Alfa Aesar 99%), $\text{ZrO}(\text{NO}_3)_2 \cdot x\text{H}_2\text{O}$ (Alfa Aesar 99.9%) and $\text{Y}(\text{NO}_3)_3 \cdot 6\text{H}_2\text{O}$ (Alfa Aesar 99.9%) were dissolved in deionized water and titrated by ethylenediaminetetraacetic acid (EDTA). Stoichiometric amounts of metal nitrate solutions were mixed in a beaker and heated at 353 K under stirring. EDTA and citric acid were added to the solution as the chelating agent, with the molar ratio of EDTA/citric acid/ total metal cations at 1:1.5:1. The pH value of the solution was adjusted by ammonia additions to a value of approximately 8. An appropriate amount of ammonium nitrate was then added to trigger combustion. The precursor solution was subsequently heated on a hot plate until self-combustion occurred. The as-prepared ash was heat-treated at 1373 K for 10 h to form the perovskite structure.

To evaluate the chemical compatibility between SFM and BZY and chemical stability of SFM in 20% H_2O -air, X-ray diffraction (Rigaku MiniFlex II, with $\text{Cu K}\alpha$ radiation and a D/teX silicon strip detector) was used to identify the crystal structures of the samples after each heat treatment.

4.2.2 FABRICATION AND CHARACTERIZATION

To study the electrochemical performance of SFM-BZY air electrode, symmetrical cells were fabricated using BZY electrolyte. BZY powders and NiO powders (JT-Baker, USA) were mixed with weight ratio of 100:1. The mixed powders were used to prepare dense BZY pellets (10.3 mm in diameter and 0.5 mm in thickness) by dry-pressing and then sintering at 1723 K for 5 h. The SFM-BZY (6:4 in weight ratio) composite electrode with an effective area of 0.33 cm^2 was applied onto both sides of the BZY pellets by brush-painting SFM-BZY paste and then heat-treated at 1373 K for 2 h.

NiO-BZY fuel electrode supported cells with thin BZY electrolyte and SFM-BZY air electrode were fabricated by dry-pressing, drop-coating and brush-painting method. NiO powders, BZY powders and carbon black (average particle size: 1 μm) were mixed with weight ratio of 5.5:4.5:2. The mixed powders were used to prepare the NiO-BZY electrode substrates (10.4 mm in diameter and 0.3 mm in thickness after sintering at 1723 K) by dry-pressing and then firing at 873 K for 2 h.

The BZY electrolyte slurry was prepared by mixing and ball milling BZY powders and NiO powders (1.0 wt.% of BZY), using ethanol as solvent, TEA as dispersant, Polyvinylbutyral (PVB) as polymer binder, Dibutyl phthalate (DBP) and (polyethylene glycol-600) PEG-600 as plasticizers[117, 118]. BZY electrolyte layer was then deposited on the NiO-BZY substrates by a drop-coating method, followed by sintering at 1723 K for 5 h. The SFM-BZY composite electrode with an effective area of 0.33 cm^2 was applied onto the surface of the BZY electrolyte by brush-painting SFM-BZY paste and then sintering at 1373 K for 2 h.

The SFM-BZY/BZY/SFM-BZY symmetrical cells were placed in a cell fixture and then tested in an atmosphere furnace. Wet air (3% H_2O) was fed to the furnace. Electrochemical impedance spectra (EIS) of the symmetrical cells were recorded from 737 K to 973 K with an amplitude of 30 mV.

Schematic of the experimental apparatus for the single cell electrochemical performance measurement was shown in our previous study[119]. The prepared single cells were attached onto one end of an alumina tube using an electrical conductive paste (DAD-87, Shanghai Research Institute of Synthetic Resins, China) and high temperature ceramic adhesives (552-1105, Aremco, USA) as joining and sealing material, respectively.

4 ml min⁻¹ H₂ (10 vol.%) and 36 ml min⁻¹ N₂ (90 vol.%) were introduced to the hydrogen electrode side, while 30 ml min⁻¹ air (3% H₂O) was introduced to the air electrode side. The flow rates of air, H₂ and N₂ were controlled by mass flow controllers (APEX, Schoonover, USA). Electrochemical characterizations for the single cells were conducted on an electrochemical test system (Versa STAT 3-400, Princeton Applied Research, USA). The *I-V* curves were recorded with a voltage sweep speed of 0.03 V s⁻¹. The exhaust gas from the Ni-BZY electrode side was analyzed by a gas chromatograph (7890A, Agilent, USA).

Microstructures of the single cells before and after the electrochemical test were examined by scanning electron microscope (SEM, Zeiss Ultra Plus FESEM).

4.3 RESULT AND DISCUSSIONS

The chemical compatibility of SFM with BZY has been investigated, as shown in Fig. 4.02 (a). The XRD patterns of SFM and BZY reveal perovskite structure without any secondary phase, suggesting that single phase SFM and BZY have been synthesized successfully. SFM and BZY powders were then mixed with weight ratio of 1:1 and heat treated at 1373 K for 5 h. The XRD pattern of the mixture reveals only SFM and BZY phases, demonstrating that SFM and BZY is chemically compatible at 1373 K.

The chemical stability of the air electrode material for H-SOECs in atmosphere containing high humidity is indispensable for durable electrolysis performance. Therefore, the chemical stability of SFM in 20% H₂O-80% air was evaluated at 873 K for 50 h, and XRD patterns of SFM before and after the exposure in high steam content are shown in Fig. 4.02 (b), revealing no obvious change after steam treatment, indicating that SFM is stable in atmosphere containing high humidity. By contrast, the chemical stability of LSCF

is also studied in 20% H₂O-80% air at 873 K for 50 h, and the corresponding results are presented in Fig. 4.03. It is obvious that XRD peaks corresponding to Sr(OH)₂ are detected after steam treatment. The formation of Sr(OH)₂ may block the active surface of LSCF, leading to degradation of the electrolysis performance. The degradation of performance of LSCF in 10% H₂O-air at 973 K has also been reported by Liu *et al.*[114].

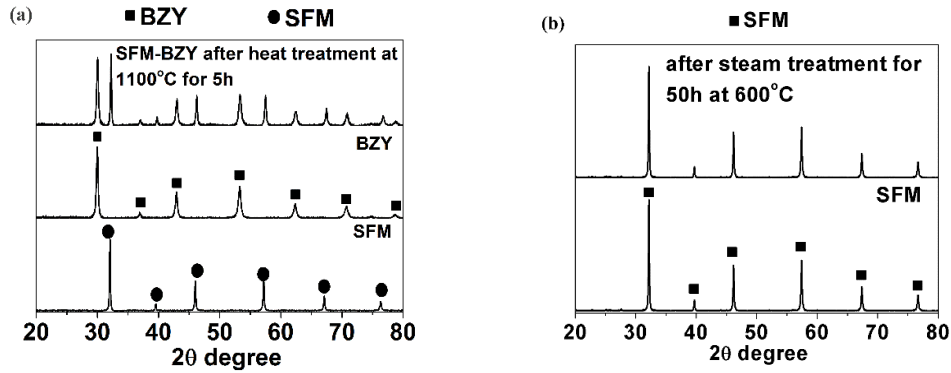


Figure 4.02 XRD patterns showing (a) chemical compatibility between SFM and BZY (b) the stability of SFM in 20%H₂O-air at 873 K.

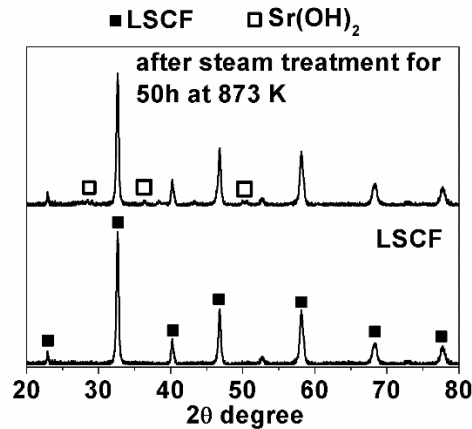


Figure 4.03 The stability of LSCF in 20%H₂O-Air at 873 K.

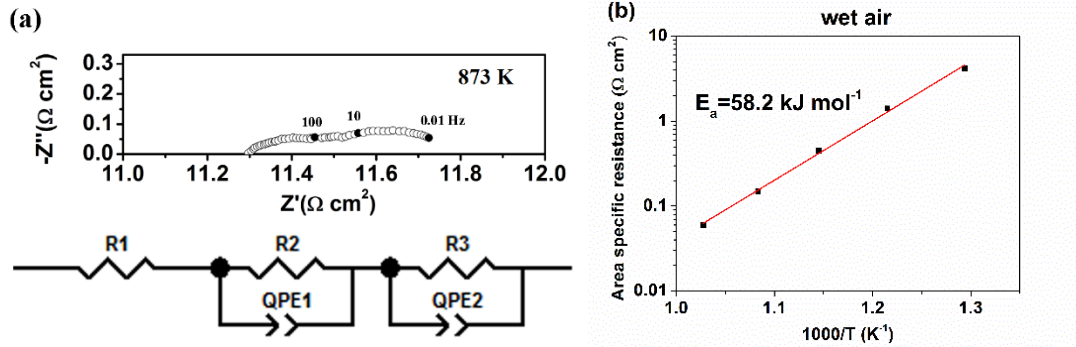


Figure 4.04 Electrochemical characterization of symmetrical cell (a) Impedance spectra in wet air (3% H₂O) at 873 K and its equilibrium circuit; (b) Arrhenius plot of polarization resistances.

To evaluate the electrochemical performance of SFM-BZY electrode, the impedance spectra of symmetrical cells with SFM-BZY electrode were recorded in wet air (3% H₂O), as shown Fig.4.04. In Fig. 4.04 (a), the impedance spectrum at 873 K and its corresponding equilibrium circuit are presented. The R₁, R₂ and R₃ in the equilibrium circuit are the electrolyte ohmic resistance, and the electrode polarization resistance at high and low frequency, respectively. Zhao et al.[120] reported an area-specific resistance (ASR) of 1.668 Ω cm² at 873 K for composite air electrode PrBaCo₂O_{5-δ}-BaZr_{0.1}Ce_{0.7}Y_{0.2}O_{3-δ} for H-SOFC, while another composite air electrode of Sm_{0.8}Sr_{0.2}CoO_{3-δ}-BaCe_{0.8}Sm_{0.2}O_{3-δ} with an ASR of 0.67 Ω cm² at 873 K was reported by Wu *et al.*[121]. In this study, the ASR of SFM-BZY is only 0.48 Ω cm² at 873 K, suggesting that this air electrode has good catalytic activity for the H-SOEC. Fig. 4.04 (b) shows the ASRs versus reciprocal temperature for SFM-BZY electrode in wet air. The activation energy of SFM-BZY is 58.2 kJ mol⁻¹, which is lower than PrBaCo₂O_{5-δ}-BaZr_{0.1}Ce_{0.7}Y_{0.2}O_{3-δ} (82.3 kJ mol⁻¹) in our previous study[120]. This relatively small activation energy shows that SFM-BZY can potentially be a promising air electrode material for H-SOEC in intermediate temperature range.

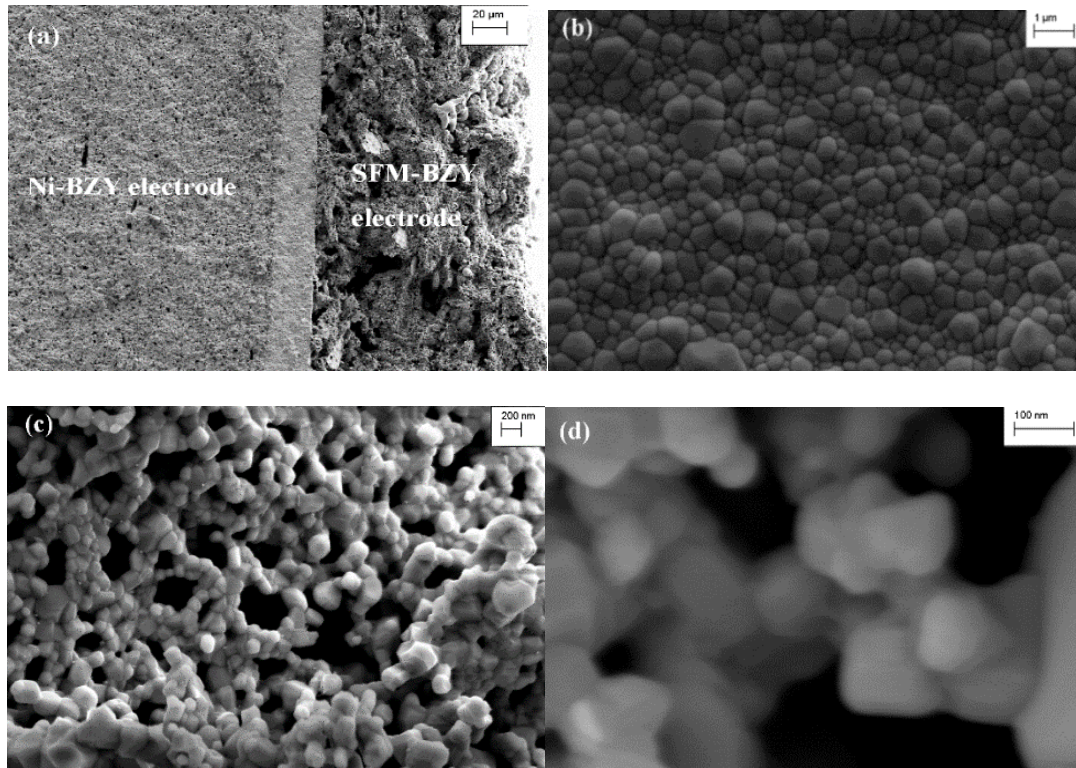


Figure 4.05 SEM image (a) the cross section of single cell; (b) the surface of the BZY electrolyte; (c) the microstructure of SFM-BZY electrode at low magnification; (d) the microstructure of SFM-BZY electrode at high magnification.

Fig. 4.05 shows the microstructure of Ni-BZY electrode supported cell with thin BZY electrolyte, porous Ni-BZY fuel electrode, and porous SFM-BZY air electrode. From Fig. 4.05 (a), it can be seen that the Ni-BZY fuel electrode and SFM-BZY air electrode show sponge-like porous microstructure, while BZY electrolyte between these two porous electrodes is relatively dense and about 16 μm in thickness. The microstructure of the surface of the BZY electrolyte, fabricated by drop-coating method [117, 118, 122, 123] with 1.0 wt.% NiO as sintering aid [124, 125], is displayed in Fig. 4.05 (b). The BZY grains are tightly packed without any obvious pores, indicating that the electrolyte is sufficiently dense to separate the gas at one electrode side from the other electrode side. Compared with thick electrolyte in electrolyte-supported cells [126], this thin electrolyte can

effectively reduce the ohmic resistance of the cells, enabling the electrolysis cells to be operated at lower temperatures.

The microstructure of SFM-BZY electrode was also characterized by SEM, as shown in Fig. 4.05 (c) and (d). The SFM-BZY air electrode is relatively porous, which is beneficial to the gas diffusion in the electrode. In addition, the particles form connected network, which provides pathway for the transportation of ions and electrons. At high magnification, it can be seen that the size of the SFM-BZY grains is very small (less than 100 nm). This small grain size of SFM-BZY air electrode can provide large specific surface area (reaction sites) for gas conversion reaction. Therefore, this unique nano-sized microstructure has resulted in low ASR value and small activation energy of SFM-BZY air electrode shown in Fig. 4.04.

The electrochemical performance of single cell in the fuel cell mode is shown in Fig. 4.06. The OCVs of single cells are above 0.9 V in all tested conditions, indicating that the electrolyte layer is reasonably dense, which is consistent with the SEM images in Fig. 4.05. The single cell shows reasonable performance in the fuel cell mode. At 873 K, the ohmic resistance is $1.03 \Omega \text{ cm}^2$, which is larger than the polarization resistance of $0.65 \Omega \text{ cm}^2$, suggesting that the main limiting factor for the performance of single cells is the ohmic resistance. The electrochemical performance of single cells in this study is compared with those using the traditional LSCF air electrode in the literature [127, 128]. From Table 4.01, it can be seen that the polarization resistance of single cells with SFM-BZY electrode in this study is $0.65 \Omega \text{ cm}^2$, which is smaller than those with the traditional LSCF air electrode reported in the literature ($3.18 \Omega \text{ cm}^2$ and $1.19 \Omega \text{ cm}^2$) at similar testing conditions. Consequently, single cells with SFM-BZY air electrode have smaller polarization

resistance and higher maximum powder density than those with the traditional LSCF, as shown in Table 4.01. According to the above comparison of the electrochemical performance and stability test in Fig. 4.02 (b) and Fig. 4.06, SFM is a better candidate than the traditional LSCF as the air electrode material of proton conducting solid oxide fuel cells and solid oxide electrolysis cells.

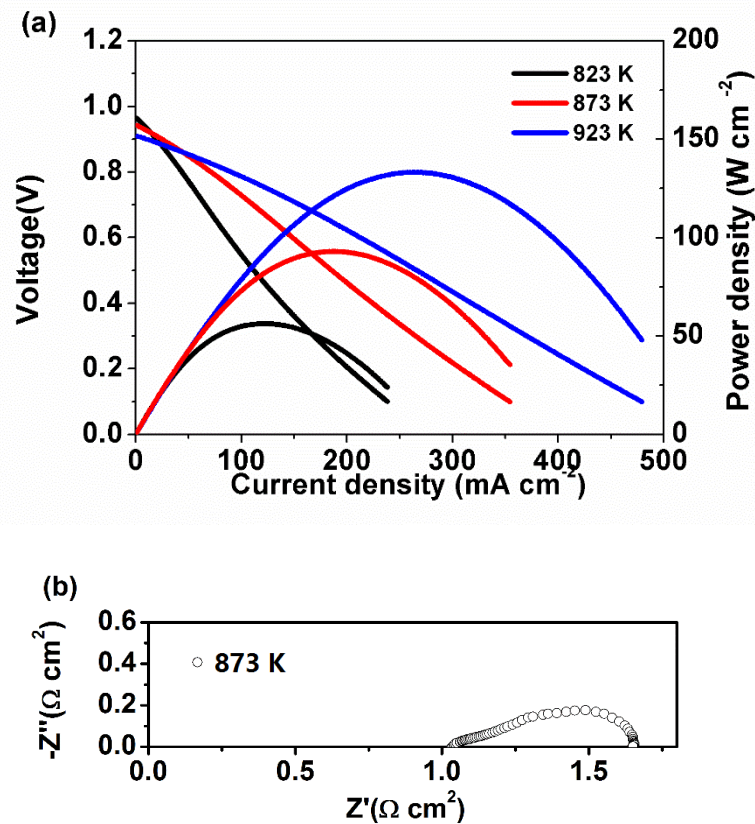


Figure 4.06 Electrochemical performance of single cells in the fuel cell mode (a) I-V curves at different temperatures; (b) Impedance spectrum under OCV at 873 K.

In the electrolysis mode, the I-V curves of the single cells with SFM-BZY electrode are recorded, as shown in Fig. 4.07. It can be found that the absolute current densities increase with the increase of the applied voltage and temperature. For example, when the

applied voltage is 1.3 V, the current densities are -100 mA cm^{-2} , -210 mA cm^{-2} and -310 mA cm^{-2} at 823 K, 873 K and 923 K respectively.

Table 4.01 Comparison of the performance of typical H-SOFCs with BZY as the electrolyte

Configuration of electrolysis cell	Operation temperature (K)	Polarization resistance ($\Omega \text{ cm}^2$)	Maximum Power Density (W cm^{-2})	Ref. (year)
LSCF -BZYP ($\text{BaZr}_{0.7}\text{Y}_{0.2}\text{Pr}_{0.1}\text{O}_{3-\delta}$)/ BZY20 (30 μm)/Ni-BZY	873	3.18	0.050	[128] 2011
LSCF /BZY20 (5 μm) /Ni-YSZ	873	1.19	0.080	[127] 2015
SFM-BZY /BZY20 (16 μm) /Ni-BZY	873	0.65	0.094	This study

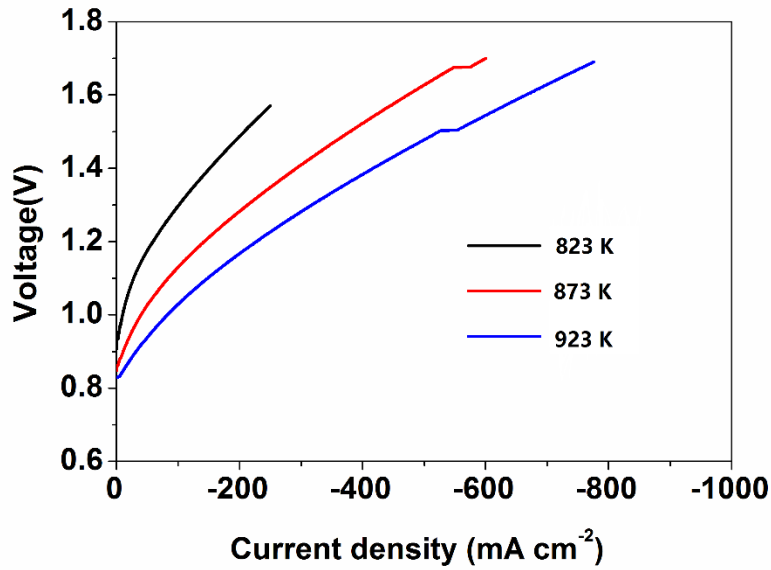


Figure 4.07 I-V curves of single cell in electrolysis mode (3% H_2O -air in air electrode, 90% N_2 -10% H_2 in air electrode).

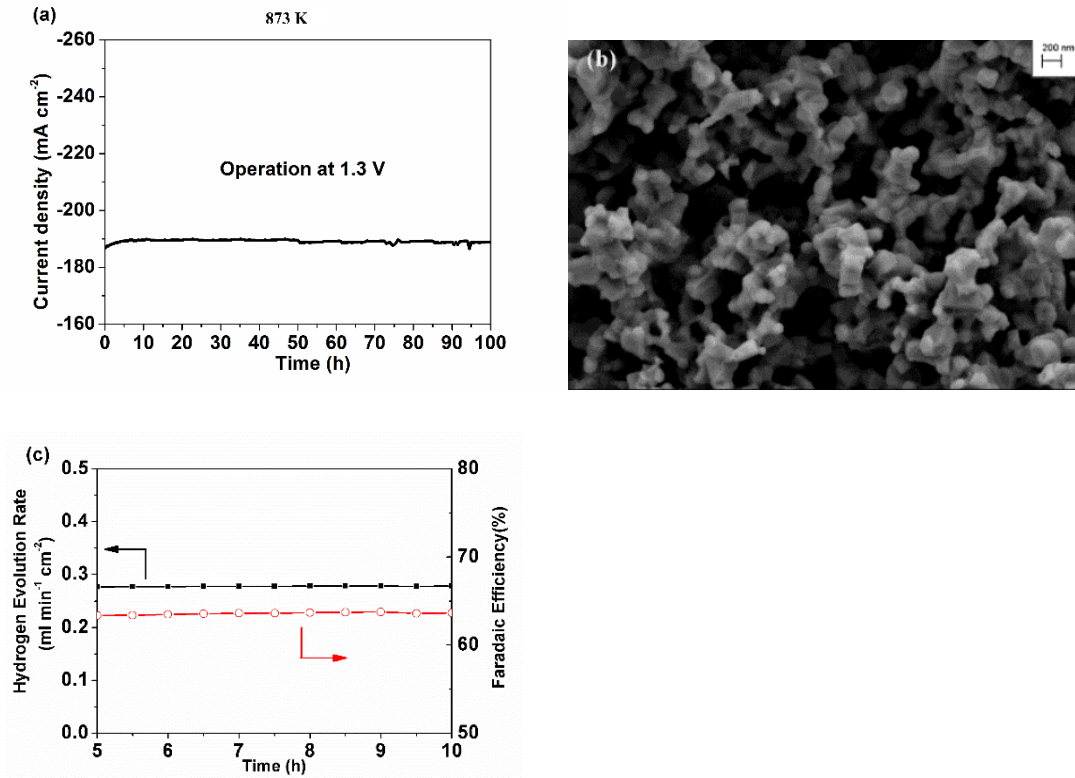


Figure 4.08 Short term stability in electrolysis mode (a) Current vs time; (b) SEM image of SFM-BZY air electrode after the stability test; (c) Hydrogen evolution rate and faradaic efficiency.

To investigate the stability of the H-SOECs with SFM-BZY air electrode, the H-SOECs were operated at 1.3 V for 100 h, as shown in Fig. 4.08 (a). The reason why 1.3 V is selected as the operating condition is that 1.3 V is close to the thermal neutral voltage of steam electrolysis (1.28 V at 873 K). During the stability test, the current density is slightly increased initially and then becomes stable at about -190 mA cm^{-2} . The current density at steady state is slightly smaller than that at transient state recorded by the I-V curves (-210 mA cm^{-2} as shown from Fig. 4.07). This difference is probably due to the fact that the influence of gas diffusion is different at transient state and at steady state. Fig. 4.08 (b) shows the microstructure of the SFM-BZY air electrode after the stability test. The SFM-BZY air electrode is still very porous and no obvious grain growth is observable,

suggesting that the nano-structured SFM-BZY air electrode is stable during the electrolysis operation at 873 K. To date, the reports concerning the stability of H-SOECs are very few, which may be due to the instability of the electrolyte or the air electrode material. Iwahara et al. [129] and Gan et al.[77] have reported stability test of H-SOECs, however the test time is less than 10 h. Bi et al. [17] have reported the durability of H-SOECs with LSCF as the air electrode, but the chemical stability of LSCF in steam shows serious issue.

To measure the actual hydrogen evolution rate during the stability test, the exhaust in the hydrogen electrode side was analyzed by GC, as shown in Fig. 4.08 (c). After the electrolysis current was stable after 5 h, the actual hydrogen evolution rate is stable at $0.278 \text{ ml min}^{-1} \text{ cm}^{-2}$. In theory, -190 mA cm^{-2} would generate $0.437 \text{ ml min}^{-1} \text{ H}_2$, when the faradaic efficiency of the electrolysis is 100%. Therefore, the actual faradaic efficiency of electrolysis during the stability test equals to $0.278/0.437=63.6\%$, indicating that the main conducting carrier of electrolysis current in BZY electrolyte layer is proton instead of hole.

Iwahara *et. al* [129-131] first reported steam electrolysis in H-SOECs during the 1980s, however, the test was conducted at high operating temperatures (1073 -1273 K) due to the use of thick electrolyte. In recent years, steam electrolysis in H-SOECs operating at intermediate temperatures (823-973 K) has been extensively pursued. Table 4.02 summarizes the performance of H-SOECs in the literature as well as the results from this study. H-SOECs with thick $\text{BaCe}_{0.9}\text{Y}_{0.1}\text{O}_{3-\delta}$ electrolyte ($450 \mu\text{m}$) were reported by Stuart et al.[132] in 2008. However, electrolysis current density is very low (12 mA cm^{-2} at 1.3 V and 873 K), due to the large ohmic resistance of the electrolyte. To reduce the ohmic resistance of the electrolyte, thin electrolyte layers have been fabricated on Ni based electrode supports, resulting in significant improvement of the electrolysis performance[10,

77, 133]. For example, electrolysis current density of $\sim 190 \text{ mA cm}^{-2}$ was achieved at 1.3 V and 873 K, when the thickness of the $\text{BaCe}_{0.5}\text{Zr}_{0.3}\text{Y}_{0.2}\text{O}_{3-\delta}$ electrolyte is reduced to $20 \mu\text{m}$ [133]. Besides large ohmic resistance of the electrolyte, the stability of the electrolyte material in H_2O -containing atmosphere is another issue for the development of H-SOECs. Except for the work of Bi *et al.* [109], cerate proton-conducting electrolyte was mainly used in the previous studies [10, 77, 126, 133-135]. As mentioned above, partial substitution of Ce by Zr cannot make cerate proton-conducting oxides fully stable in H_2O -containing atmosphere [15, 16]. Even though the single cells with $\text{BaCe}_{0.5}\text{Zr}_{0.3}\text{Y}_{0.16}\text{Zn}_{0.04}\text{O}_{3-\delta}$ electrolyte ($75 \mu\text{m}$) show the highest cell performance (960 mA cm^{-2}) at 973 K, the stability of the cells with cerates electrolyte is still a serious concern.

For H-SOECs using zirconate proton-conducting electrolyte, the current density using SFM-BZY air electrode in this study (210 mA cm^{-2}) is about four times of that with LSCF-BZY air electrode (53 mA cm^{-2}). The main difference between these two studies is the air electrode. Therefore, the excellent performance in this study is attributed to the application of the SFM-BZY air electrode. High porosity of the SFM-BZY air electrode is beneficial to gas diffusion in the electrode and the nano-scaled grains (less than 100 nm) offer increased triple phase boundaries for the reduction of H_2O in the air electrode, resulting in small polarization resistances, as shown in Fig. 4.04.

Table 4.02 Comparison of the performance of H-SOECs at 1.3 V

Configuration of electrolysis cell	Operation temperature (K)	Inlet gas composition in the air electrode	Absolute Current density (mA cm ⁻²)	Ref. (year)
Pt/BaCe _{0.9} Y _{0.1} O _{3-δ} (450 μm)/Pt	873	air	12	[126] 2008
SSC-BCZY/ BaCe _{0.5} Zr _{0.3} Y _{0.2} O _{3-δ} (20 μm)/Ni-BCZY	873	50% H ₂ O, 50% Air	~190	[133] 2010
LSC-BZCYbCo/ BaCe _{0.48} Zr _{0.4} Yb _{0.1} Co _{0.02} O _{3-δ} (45 μm)/Ni-BCZYbCo	873	3% H ₂ O, 19.4% O ₂ , 77.6% He	16	[134] 2011
LSCM-BZCZY/ BaCe _{0.5} Zr _{0.3} Y _{0.16} Zn _{0.04} O _{3-δ} (75 μm)/Ni-BCZY	973	3% H ₂ O, 97% N ₂	960	[77] 2012
LSCF-BZCZY/ BaCe _{0.5} Zr _{0.3} Y _{0.16} Zn _{0.04} O _{3-δ} (2000 μm)/ Ni-BCZY	1073	3% H ₂ O, 97% Air	26	[135] 2013
LSCF-BZY/ BZY(15 μm)/Ni-BZY	873	3% H ₂ O, 97% Air	53	[17] 2015
LNF/LN-BCZD/ BaCe _{0.5} Zr _{0.3} Dy _{0.2} O _{3-δ} (30 μm)/Ni-BCZD	873	3% H ₂ O, 97% Air	~170	[10] 2016
SFM-BZY/ BZY(16 μm)/Ni-BZY	873	3% H ₂ O, 97% Air	210	This study

Moreover, considering the Faradaic efficiency of electrolysis is important when the electrochemical performance is compared. The OCV at 873 K in this study (0.86 V) and that in literature (0.85 V) are lower than the theoretical one (1.048 V), indicating that there may be electronic conductivity in the electrolytes and the Faradaic efficiencies of electrolysis can't reach 100% in both studies. In this study, the actual faradaic efficiency

of electrolysis is 63.6%, when the electrolysis current is 190 mA cm^{-2} , as shown in Fig. 4.08 (c). Similarly, Iwahara *et al.*[131] have reported that for proton conductor, the current efficiency for hydrogen evolution ranges from 50%-95%. The current efficiency of electrolysis is closely related to the ion transport number (t_i) and the electron transport number (t_e) of the electrolyte material. Assuming that the partial pressures of H_2O are the same in both electrode sides, these transport numbers can be determined by the following equations[10, 136]:

$$E = t_i \frac{RT}{4F} \ln\left(\frac{p'O_2}{p''O_2}\right) \quad (4.01)$$

$$t_i = \frac{E}{E_0} \quad (4.02)$$

$$t_i + t_e = 1 \quad (4.03)$$

where E and E_0 are the actual OCV and theoretical OCV of oxygen concentration cells respectively, R is the universal gas constant, T is the absolute temperature (K), F is the Faraday constant and $p'O_2$ and $p''O_2$ are the oxygen partial pressure of the air electrode and the fuel electrode, respectively. According to Equations (4.02) and (4.03), the transport numbers (t_i and t_e) of the BZY electrolyte in this study and in the literature with LSCF-BZY air electrode should be similar because of the similar OCVs in both studies. Therefore, it is reasonable to assume that the Faradaic efficiency of electrolysis is very close in both studies. Consequently, the actual performance of H-SOECs using the SFM-BZY air electrode in this study is still better than those using the LSCF-BZY air electrode in the literature[17].

4.4 CONCLUSIONS

In this work, stable H-SOECs are successfully fabricated. BZY, with good chemical stability in H_2O -containing atmosphere, is employed as the electrolyte material. Thin and

dense BZY electrolyte (16 μm) is fabricated using drop-coating method with 1wt.% NiO addition as the sintering aid. SFM, which is also chemically stable in H_2O -containing atmosphere, is applied as the air electrode material of H-SOECs for the first time. Highly porous SFM-BZY with nano-structured particles provides sufficient pores and channels for the gas transportation and large specific surface area for the gas conversion. Consequently, the H-SOECs with Ni-BZY fuel electrode support, thin BZY electrolyte and robust SFM-BZY air electrode, show stable and excellent performance for steam electrolysis with 63.6% faradaic efficiency.

CHAPTER 5 A HIGHLY ACTIVE HYBRID CATALYST MODIFIED LSCF CATHODE FOR PROTON CONDUCTING SOLID OXIDE FUEL CELLS

5.1 BACKGROUND

Solid oxide fuel cell (SOFC) has received increasing attention in recent years owing to its high energy-conversion efficiency, broad application range and fuel flexibility [137]. However, the high operation temperature (1073-1273 K) of traditional SOFCs hinders their commercialization and deployment both in portable devices and stationary applications. Therefore, considerable efforts have been devoted to developing intermediate temperature (673-923 K) SOFCs in the past ten years [138-141]. Proton-conducting SOFC (H-SOFC) has gradually attracted significant research attention for its reduced operation temperature, relatively low activation energy and high energy efficiency [142-145].

As one of the state-of-the-art electrolytes for H-SOFC, $\text{BaZr}_{1-x}\text{Y}_x\text{O}_3$ (BZY) has garnered particular attention because of its high chemical stability and high bulk proton conductivity [113, 124, 146-149]. However, there are still a number of technical challenges for BZY electrolyte. The sluggish rate of oxygen reduction reaction (ORR) in the cathode, and consequently high cathode polarization resistance, is one of the crucial factors influencing the performance of the H-SOFC [107, 150]. Among the cathode materials developed for H-SOFCs, $\text{La}_x\text{Sr}_{1-x}\text{Co}_y\text{Fe}_{1-y}\text{O}_3$ (LSCF) cathode, which has been widely studied in oxygen-ion conducting SOFC (O-SOFC), has also been applied in H-SOFCs for

its high electronic and ionic conductivities [151]. However, the relatively slow kinetics of oxygen dissociation-absorption process limits the performance of LSCF as cathode material for H-SOFCs [152]. To date, the highest maximum power density of H-SOFC with BZY as electrolyte material and LSCF as cathode material is only 0.11 W cm^{-2} at 600°C [153]. Moreover, Sr segregation near surfaces or interfaces of LSCF causes significant degradation of the electrochemical performance and affects its long-term operational life [151].

One effective way to solve the above problems is to modify the surface of LSCF through impregnation with coating of stable and catalytically-active nanoparticles [154]. Ding *et al.* [155] have reported that the electro-catalysis and stability of LSCF cathode in O-SOFCs can be substantially enhanced by coating the more active Mn-based catalyst. Recently, Chen *et al.* [156] have reported that the electrochemical performance and stability of LSCF in O-SOFCs could be drastically improved by forming a thin layer of $\text{PrNi}_{0.5}\text{Mn}_{0.5}\text{O}_3$ (PNM) and PrO_x nanoparticles on the LSCF surface through impregnation of $\text{Pr}_2\text{Ni}_{0.5}\text{Mn}_{0.5}\text{O}_4$ solution. However, the above studies have been conducted in O-SOFCs but not in H-SOFCs. Unlike the O-SOFCs, protons (H^+) are transported and water is formed at the cathode side of H-SOFCs, making cathode reactions fundamentally different from that of the O-SOFCs, resulting in more sluggish ORR [157, 158]. Unfortunately, there have been very limited reports concerning the modification of LSCF cathode by impregnation for H-SOFCs. Although $\text{Y}_{0.25}\text{Bi}_{0.75}\text{O}_{1.5}$, $\text{Gd}_{0.1}\text{Ce}_{0.9}\text{O}_{1.95}$ (GDC) and Ag have been impregnated in the LSCF cathode, these studies have been mainly focused on improving electro-catalytic performance and the effect of the nanoparticle catalyst on the LSCF cathode stability has not been reported yet [152, 159, 160].

In order not only to enhance the electro-catalysis but also to improve the stability of LSCF cathode in H-SOFCs based on BZY electrolyte, hybrid catalyst consisting of PNM and PrO_x has been impregnated to the LSCF cathode in this study, as shown in Fig. 5.01. Microstructure characterization shows that the nano-structured modification on the LSCF cathode is obtained. Experimental results demonstrate that the hybrid catalyst on the LSCF surface can significantly enhance the oxygen adsorption and dissociation process of ORR, resulting in substantial reduction in the polarization resistance of the LSFC cathode and enhancement of the H-SOFC cell performance. In addition, the hybrid catalyst can potentially suppress Sr segregation and consequently improve the H-SOFC long-term performance stability.

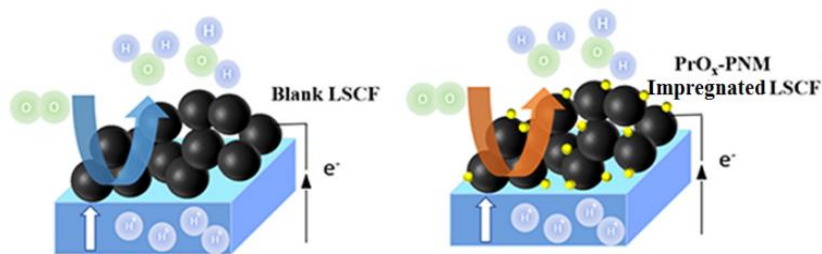


Figure 5.01 Schematic illustrations of blank LSCF electrode and PNM- PrO_x impregnated LSCF for H-SOFCs.

5. 2 EXPERIMENTAL

5.2.1 SYNTHESIS AND CHARACTERIZATION OF MATERIALS

The BZY powders were synthesized by a combined EDTA-citric acid method[116]. The PNM powders were synthesized by a wet chemical method. $\text{Pr}(\text{NO}_3)_3 \cdot 6\text{H}_2\text{O}$ (Alfa Aesar 99.9%), $\text{Ni}(\text{NO}_3)_2 \cdot 6\text{H}_2\text{O}$ and $\text{Mn}(\text{NO}_3)_3 \cdot 6\text{H}_2\text{O}$ were used as the raw materials while citric acid was added as the complexing agent. Other procedures were similar to the above

and the fired temperature of the as-prepared ash was controlled at 1073 K for 1 h to obtain the final powders.

To evaluate the chemical compatibility between PNM and BZY and chemical stability of SFM in 20% H_2O -air, X-ray diffraction (Rigaku MiniFlex II, with $\text{Cu K}\alpha$ radiation and a D/teX silicon strip detector) was used to identify the crystal structures of the samples after each heat treatment.

5.2.2 FABRICATION AND CHARACTERIZATION OF SINGLE CELLS

NiO-BZY electrode supported cells with thin BZY electrolyte layer were fabricated by dry-pressing and drop-coating. NiO powders (JT-Baker, USA), BZY powders and carbon black (average particle size: 1 μm) were mixed with weight ratio of 5.5:4.5:2. The mixed powders were used to prepare the NiO-BZY electrode substrates (10.3 mm in diameter and 0.3 mm in thickness after sintering at 1450 $^\circ\text{C}$) by dry-pressing and then firing at 873 K for 2 h.

The BZY electrolyte slurry was prepared by mixing and ball milling BZY powders, NiO powders (1.0 wt.% of BZY) as sintering aid, ethanol as solvent, TEA as dispersant, Polyvinylbutyral (PVB) as polymer binder, Dibutyl phthalate (DBP) and (polyethylene glycol-600) PEG-600 as plasticizers [117, 118]. BZY electrolyte layer was then deposited on the NiO-BZY substrates by drop-coating method, followed by sintering at 1723 K for 5 h.

The $(\text{La}_{0.60}\text{Sr}_{0.40})_{0.95}\text{Co}_{0.20}\text{Fe}_{0.80}\text{O}_{3-x}$ (LSCF, Fuel Cell material, USA) electrode with an effective area of 0.33 cm^2 was applied onto the surface of the BZY electrolyte layer by using LSCF ink and brush painting method and then sintering at 1273 K for 2 h.

Impregnation procedure. The hybrid catalyst solution used for impregnation was prepared by dissolving $\text{Pr}(\text{NO}_3)_3 \cdot 6\text{H}_2\text{O}$, $\text{Ni}(\text{NO}_3)_2$ and $\text{Mn}(\text{NO}_3)_2 \cdot 6\text{H}_2\text{O}$ in molar ratio of 4:1:1 in appropriate amount of deionized water, and then adding glycine as a chelating agent under stirring to form 0.1M $\text{Pr}_2\text{Ni}_{0.5}\text{Mn}_{0.5}\text{O}_{4+\delta}$ solution. In order to improve the permeability of the solution, ethanol was added and the impregnation process was operated in the vacuum impregnation machine (Struers CitoVac). The hybrid solution was carefully impregnated 6 μL on the surface of the LSCF cathode. After that, the assembled cells were fired at 1073 K for 1 h, allowing decomposition of nitrate and formation of PNM nanoparticles. Finally, 15 wt.% impregnation loading with respect to the weight of LSCF cathode layer is achieved.

The prepared single cells were attached to one end of an alumina tube using an electrical conductive paste (DAD-87, Shanghai Research Institute of Synthetic Resins, China). High temperature ceramic adhesives (552-1105, Aremco, USA) were then applied outside the attached cells to avoid gas leaking. 30 ml min^{-1} H_2 was fed to the hydrogen electrode side during the test. Hydrogen flow rate was controlled by mass flow controllers (APEX, Schoonover, USA). Electrochemical characterizations including current density-voltage (I - V) and impedance spectra measurements for the single cells were conducted on an electrochemical test system (Versa STAT 3-400, Princeton Applied Research, USA). The I - V curves were recorded with a voltage sweeping speed of 0.03 V s^{-1} . For the EIS measurement, the frequency range was from 1 MHz to 0.01 Hz with the AC amplitude of 30 mV.

Microstructures of the single cells before and after the electrochemical test were examined by scanning electron microscope (SEM, Zeiss Ultra Plus FESEM).

5.3 RESULT AND DISCUSSIONS

XRD patterns of BZY and hybrid catalyst are shown in Fig. 5.02 (a). It can be seen that the hybrid catalyst is consisted of PrO_x phase and $\text{PrNi}_{0.5}\text{Mn}_{0.5}\text{O}_{4+\delta}$ phase, consistent with the literature [156]. BZY shows cubic perovskite structure without any secondary phase. The hybrid catalyst and BZY powders were then mixed with weight ratio of 1:1 and heat treated at 1073 K for 5 h. The XRD pattern of the mixture after heat-treatment reveals only hybrid catalyst and BZY phases, demonstrating that the hybrid catalyst and BZY are chemically compatible at 1073 K. Moreover, the phase stability of the hybrid catalyst is essential for the durability of the cell electrochemical performance. Thus, the phase stability of the hybrid catalyst is investigated, as shown in Fig. 5.02 (b). It can be seen that the hybrid catalyst has showed excellent chemical stability at 873 K for 100 h in air.

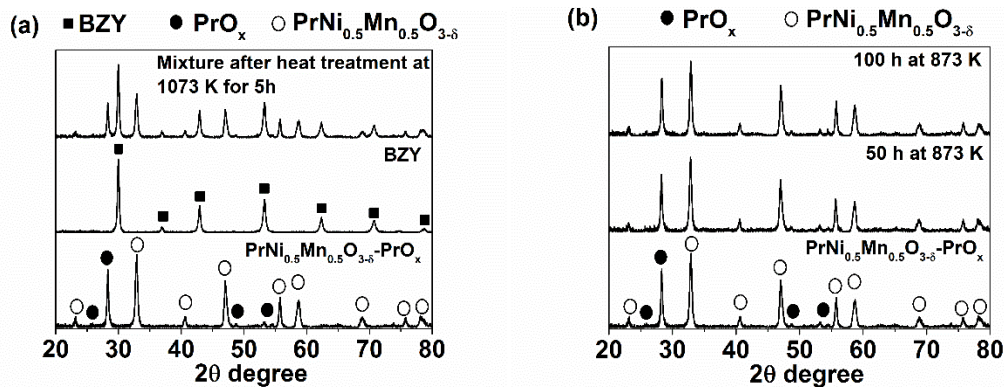


Figure 5.02 XRD patterns (a) chemical compatibility between $\text{PrNi}_{0.5}\text{Mn}_{0.5}\text{O}_3$, PrO_x , and BZY; (b) Stability of $\text{PrNi}_{0.5}\text{Mn}_{0.5}\text{O}_3$ and PrO_x .

The microstructures of porous NiO-BZY electrode support and dense BZY electrolyte layer are shown in Fig. 5.03. The surface microstructure of the BZY electrolyte layer, fabricated by drop-coating method [117, 118, 123, 161, 162] with 1.0 wt.% NiO addition as the sintering aid [124, 125], is shown in Fig. 5.03 (a). After sintering at 1723 K for 5 h, the BZY electrolyte layer is relatively dense without any obvious pores, suggesting that the

electrolyte layer can sufficiently separate the gas between electrodes. From Fig. 5.03 (b), it can be observed that the pores in the NiO-BZY electrode support are distributed evenly and the BZY electrolyte layer, with thickness of 15 μm , is well attached to the NiO-BZY electrode support.

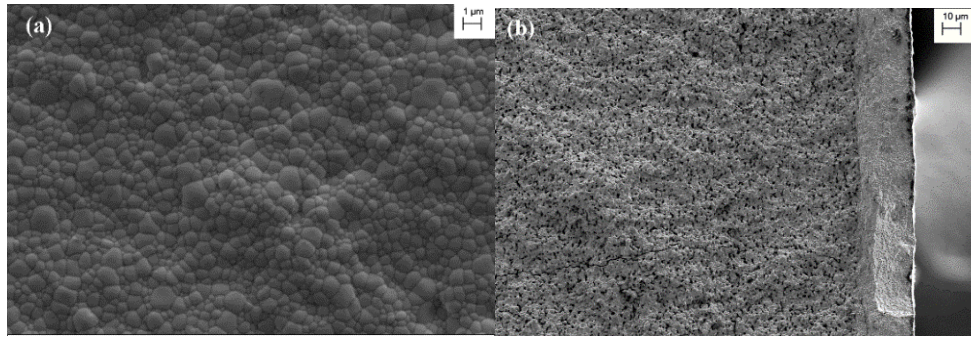


Figure 5.03 FESEM images of the single cells. (a) The surface of the BZY electrolyte; (b) The cross-section view of NiO-BZY anode and BZY electrolyte.

The microstructures of LSCF cathode before and after impregnation of the hybrid catalyst are shown in Fig. 5.04. Fig. 5.04 (a) is the typical cross-section micrograph of blank LSCF cathode. The blank LSCF cathode is well sintered with particle sizes ranging from 0.1 to 1 μm . Fig. 5.04 (b) and (c) present the micrographs of LSCF cathode with impregnation of the hybrid catalyst. Compared with the relatively smooth surface of blank LSCF particles in Fig. 5.04 (a), the surface of LSCF particles becomes rough and discrete nanoparticles are uniformly distributed on the LSCF surface, as shown in Fig. 5.04 (b). At higher magnification in Fig. 5.04 (c), it is clear that the nanoparticles are less than 20 nm, which could increase the specific surface area of the LSCF cathode. According to Chen *et al.*'s work [156], impregnation of hybrid catalyst in LSCF cathode will form a conformal PNM thin film with exsolved PrO_x nanoparticles. Therefore, the change of the roughness of the LSCF surface is probably caused by the formation of conformal PNM thin film.

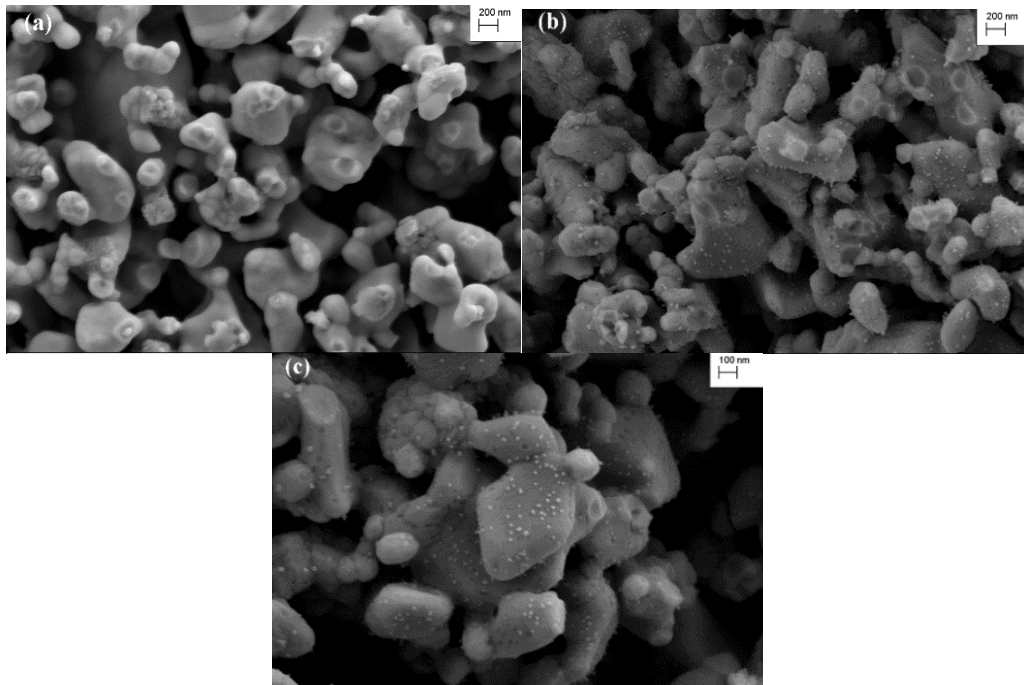


Figure 5.04 FESEM image of cathode (a) Microstructure of bare LSCF electrode; (b) Microstructure of LSCF electrode with $\text{PrNi}_{0.5}\text{Mn}_{0.5}\text{O}_3$ and PrO_x ; (c) High magnification of image of LSCF electrode with $\text{PrNi}_{0.5}\text{Mn}_{0.5}\text{O}_3$ and PrO_x .

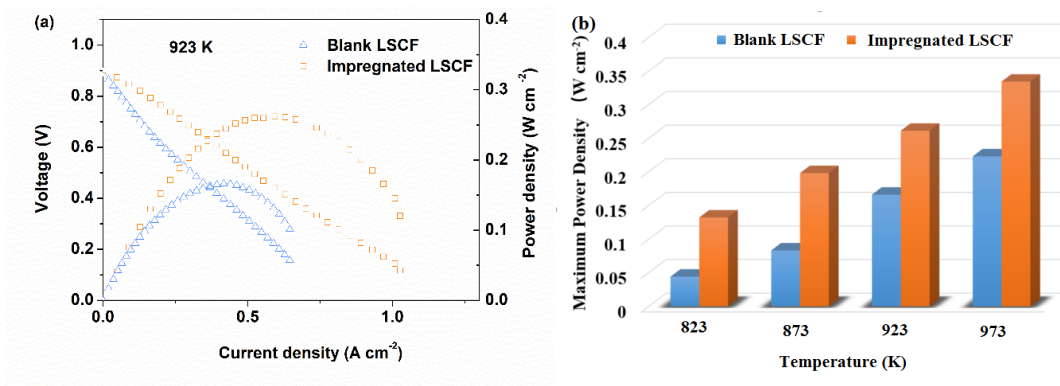


Figure 5.05 Electrochemical performance of single cells (a) I-V curves; (b) Maximum powder densities of single cells at various temperature.

To study the effect of impregnation of hybrid catalyst on the electrochemical performance of single cells, single cells with and without impregnation were tested. Fig. 5.05 (a) shows the I-V curves of single cells at 923 K. Single cells with impregnated LSCF

cathode show much better performance than those with only blank LSCF cathode. The maximum power densities (MPDs) of single cells with and without impregnation are 0.262 W cm^{-2} and 0.166 W cm^{-2} at 923 K , respectively, showing 58% performance enhancement by the impregnation. The MPDs of single cells at 823 K , 873 K , 923 K and 973 K are summarized in Fig. 5.05 (b). In this temperature range, single cells with impregnated LSCF all yielded higher MPD than that with only blank LSCF. For example, at 823 K , the MPD is raised by 200%, from 0.044 W cm^{-2} to 0.132 W cm^{-2} , through impregnation.

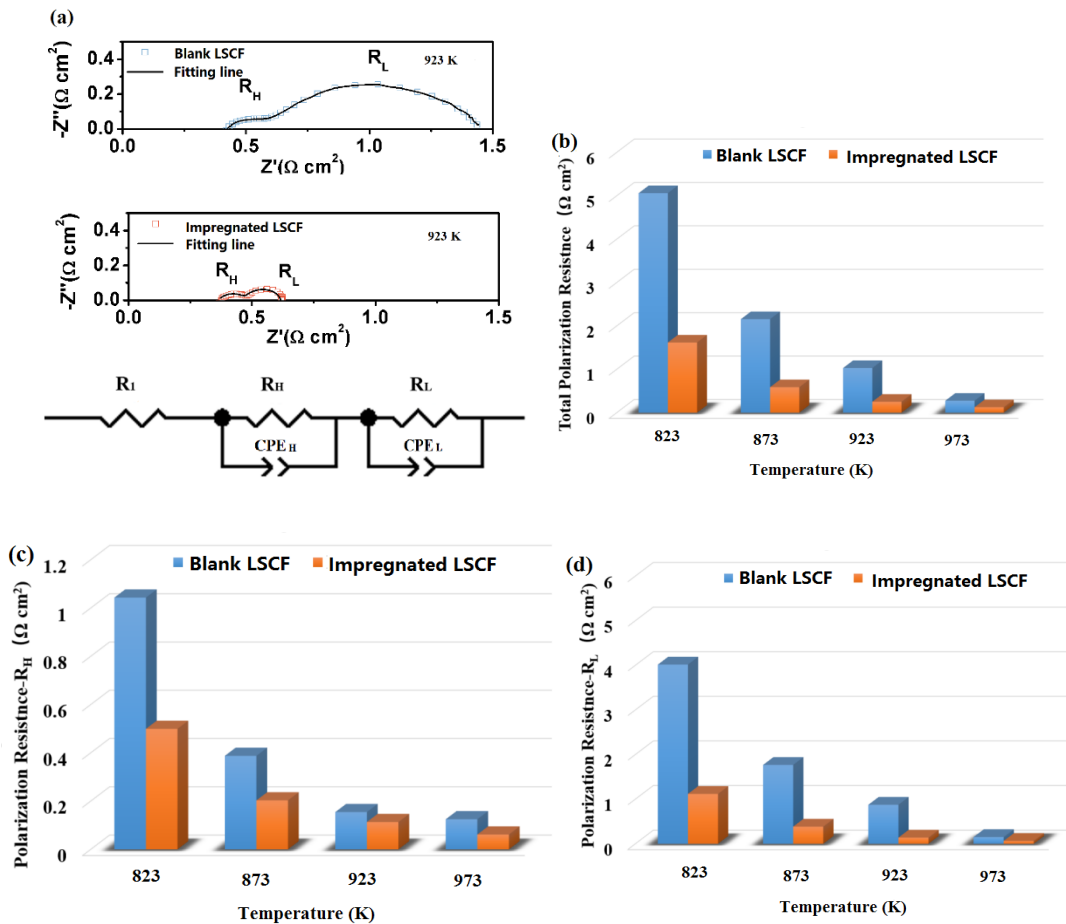


Figure 5.06 (a) Impedance spectra of single cells at $650 \text{ }^\circ\text{C}$; (b) Polarization resistance of single cells at various temperatures; (c) Polarization resistance R_H at various temperatures; (d) Polarization resistance R_L at various temperatures.

Impedance spectra of single cells with and without impregnation are measured under the OCV condition, as shown in Fig. 5.06. The intercept of the impedance spectra with the real axis represents the overall electrode polarization resistance (R_p). In Fig. 5.06 (a), the R_p of single cell is reduced from $1.03 \Omega \text{ cm}^2$ to $0.26 \Omega \text{ cm}^2$ at 923 K by the impregnation of hybrid catalyst, suggesting significant enhancement of catalytic activity of the LSCF cathode by the impregnation. This is consistent with the results of the I-V curves. Similar to the result at 923 K, R_p values are greatly reduced by impregnation of the hybrid catalyst in the LSCF cathode at various temperatures, as shown in Fig. 5.06 (b). For example, at 873 K, the R_p is reduced from $2.17 \Omega \text{ cm}^2$ to $0.58 \Omega \text{ cm}^2$ through impregnation. Furthermore, two arcs (R_H and R_L) can be clearly observed in the impedance spectra of both single cells in Fig.6 (a), implying that there are at least two rate-limiting steps. Equivalent circuit $R_1(R_H\text{CPE}_H)(R_L\text{CPE}_L)$ is applied to fit the spectra using Zview program, where R represents the resistance, CPE is the constant phase element and the subscripts H and L correspond to the high and low-frequency arc, respectively. Good agreement is obtained between the fitting curves and the experimental data, as shown in Fig. 5.06 (a). As the fabrication conditions of Ni-BZY anode and the BZY electrolyte are identical, the differences of R_H and R_L between these two types of single cells are consequently caused by the differences in the cathode. It has been reported that when oxygen-ion conducting phase is used as cathode material in H-SOFCs, oxygen ion transfer and oxygen dissociation-absorption processes are the two-main rate-limiting factors for the ORR. Moreover, the oxygen-ion transfer process generally corresponds to the ($R_H\text{CPE}_H$) component in the impedance spectra, while the oxygen dissociation-absorption process normally corresponds to the ($R_L\text{CPE}_L$) component [152, 157, 158, 163].

R_H and R_L of these two types of single cells are compared in Fig. 5.06 (c) and (d). It can be noticed that in the single cells with blank LSCF, R_L is the dominating resistance in R_p , especially at low temperatures, suggesting that oxygen dissociation-absorption process is the most sluggish step in the ORR for the blank LSCF. After impregnation of the hybrid catalyst, both R_H and R_L , especially R_L , are reduced. For example, R_L is reduced by 72%, from $4.02 \Omega \text{ cm}^2$ to $1.12 \Omega \text{ cm}^2$ at 823 K, suggesting that the acceleration of the oxygen dissociation-absorption process by the impregnation of the hybrid catalyst makes significant contribution for the improvement of electrochemical performance of the single cells. By using periodic density functional theory (DFT), XAS and XPS, Chen *et al.* [156] have demonstrated that the PNM phase in the hybrid catalyst facilitates rapid oxygen-ion transport while the exsolved PrO_x in the hybrid catalyst has low adsorption energy of O_2 (-1.19 eV) and oxygen vacancy formation energy (1.04 eV), which are beneficial for the oxygen dissociation-absorption process in ORR. Therefore, impregnation of hybrid catalyst in this study could improve not only the kinetics of oxygen-ion transfer but also oxygen dissociation-absorption process in the LSCF cathode, resulting in significant reduction of R_p , R_H and R_L .

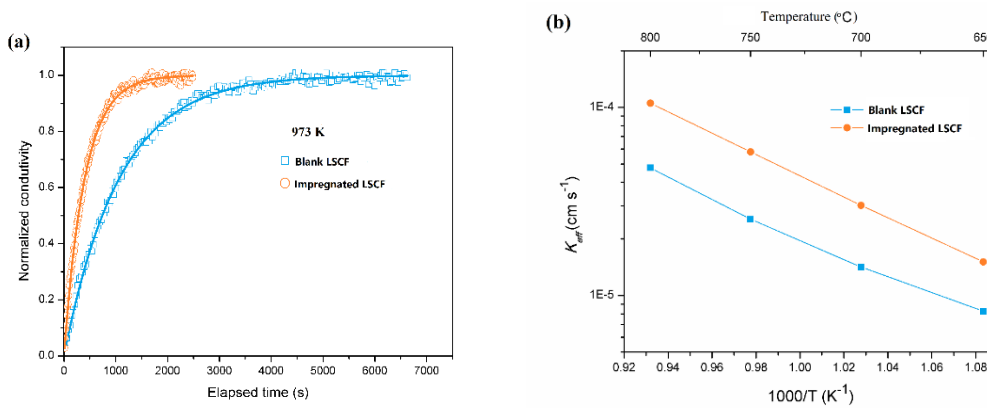


Figure 5.07 (a) Electrical conductivity relaxation as a function of time at 973 K; (b) Plots of the surface exchange coefficients (K_{eff}) as function of temperatures.

To further demonstrate the above hypothesis, the surface exchange kinetics of these cathodes was also investigated by measuring the electrical conductivity relaxation (ECR), as shown in Fig. 5.07. Fig. 5.07 (a) displays the electrical conductivity relaxation for blank LSCF and the impregnated LSCF samples as a function of time. The K_{eff} values calculated from the test are plotted as a function of $1000/T$ in Fig. 5.07 (b). It can be seen that the K_{eff} values of impregnated LSCF are always higher than those of blank LSCF at various temperatures. For example, at 923 K, the surface exchange coefficient (K_{eff}) of LSCF is increased from $7.26 \times 10^{-6} \text{ cm s}^{-1}$ to $1.51 \times 10^{-5} \text{ cm s}^{-1}$ by impregnation of the hybrid catalyst, indicating that the oxygen dissociation-absorption process (oxygen surface exchange) is substantially accelerated.

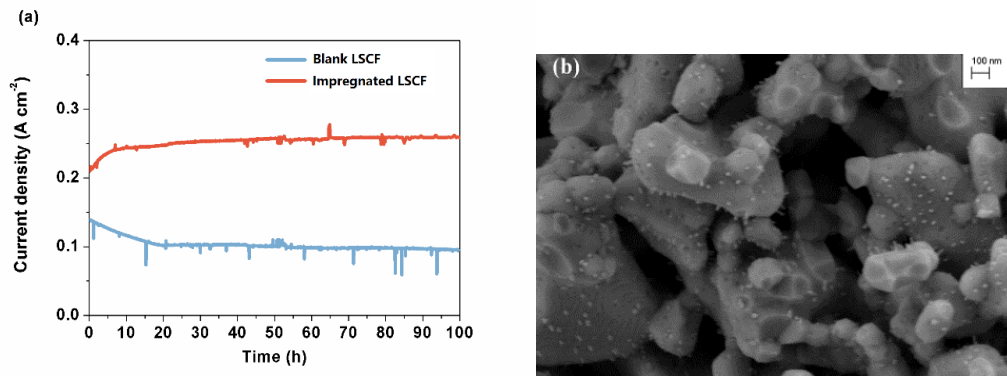


Figure 5.08 (a) Stability of single cells at 873 K (a) Operation of single cells at 0.6 V; (b) The microstructure of electrode after 100 h test.

To study the durability, single cells with and without impregnation are operated at 0.6 V and 873 K for 100h, as displayed in Fig. 5.08. In Fig. 5.08 (a), the current density of single cells with blank LSCF dropped from 0.14 A cm^{-2} to 0.10 A cm^{-2} in the first 20 h and then decreased slowly to about 0.09 A cm^{-2} in the last 80 h. The decrease of current density is most likely due to the degradation of blank the LSCF cathode. It has been reported that Sr segregation near surface is considered to contribute significantly to the degradation of

the electrochemical activity of LSCF based electrode for ORR [151]. By contrast, single cells with impregnated LSCF cathode clearly show improved and more stable performance than that with blank LSCF cathode. For example, the current density increased from 0.21 A cm⁻² to 0.24 A cm⁻² in the first 10 h and then increased moderately to 0.26 A cm⁻² in the last 90 h. The gradual increase of the cell performance may be due to the effect of the cathode activation. Moreover, the Sr segregation can be mitigated by the formation of the conformal PNM coating on LSCF. The relatively high oxygen vacancy formation energy of PNM can suppress the oxygen vacancy concentration at the LSCF/PNM interface, consequently reducing the driving force for Sr segregation [156]. The nano-structured morphology of hybrid catalyst after 100 h cell testing (Fig. 5.08 (b)) is similar to that before the test (Fig. 5.04), indicating excellent stability of the impregnated phases.

The performance of single cells in this study is compared with those of H-SOFCs using BZY electrolyte in the literature as shown in Table 5.01. It can be found that the MPDs of single cells with blank LSCF as cathode range from 0.050 W cm⁻² to 0.11 W cm⁻² in the literature [127, 128, 153], which is close to the one with the blank LSCF (0.083 W cm⁻²) measured in this study. Besides LSCF, Sm_{0.5}Sr_{0.5}CoO_{3-δ}-Ce_{0.8}Sm_{0.2}O_{2-δ} (SSC-SDC) has also been studied as cathode for H-SOFCs [111, 122, 164] and the cell performance of single cells with the SSC is typically lower than that of the LSCF cathode. The performance of single cells with impregnated LSCF is better than the reported H-SOFCs with the blank LSCF cathode [127, 128, 153]. It can be seen that among all studies in the table, single cells with impregnated LSCF show the second highest MPD, only lower to a novel mixed protonic, oxide ionic and electronic conducting BaCo_{0.4}Fe_{0.4}Zr_{0.2}Y_{0.1}O_{3-δ} (BCFZY)

cathode. These comparisons indicate that hybrid catalyst impregnated LSCF is a promising cathode candidate for H-SOFCs.

Table 5.01 Comparison of the performance of H-SOFCs with BZY as the electrolyte

Configuration of single cells	Operation temperature (K)	MPD (W cm ⁻²)	Ref. (year)
PrBaCo ₂ O _{5+δ} -BZYP/BZY20(20 μm) /Ni-BZY	873	0.169	[165] 2011
LSCF-BCYb (BaCe _{0.9} Yb _{0.1} O _{3-δ})/BZY20 (4 μm) /Ni-BZY	873	0.11	[153] 2010
Sm _{0.5} Sr _{0.5} CoO _{3-r} -Ce _{0.8} Sm _{0.2} O _{2-δ} (SSC-SDC) /BZY20(20 μm) /Ni-BZCY	873	0.062	[111] 2010
LSCF -BZYP/BZY20(30 μm) /Ni-BZY	873	0.050	[128] 2011
SSC-SDC/BZY20(25 μm) /Ni-BZCY	873	0.055	[122] 2012
BCFZY (BaCo _{0.4} Fe _{0.4} Zr _{0.2} Y _{0.1} O _{3-δ}) /BZY20/Ni-BZY	873	0.49	[16] 2015
LSCF /BZY20(5 μm)/Ni-BZY	873	0.080	[127] 2015
SSC-SDC/BZY20(16 μm) /Ni-BZCY	873	0.035	[164] 2016
Impregnated-LSCF / BZY20(16 μm) /Ni-BZY	873	0.198	This study
LSCF /BZY20(16 μm) /Ni-BZY	873	0.083	This study

5.4 CONCLUSIONS

In conclusion, H-SOFCs with NiO-BZY anode support, BZY thin electrolyte and LSCF cathode have been successfully fabricated. To enhance the ORR reaction kinetics, LSCF cathode is modified by impregnation of hybrid catalyst consisting of $\text{PrNi}_{0.5}\text{Mn}_{0.5}\text{O}_3$ and PrO_x . The electrochemical tests show that the cell performance is greatly increased by the impregnation of hybrid catalyst to the LSCF cathode. At 923 K, single cells with hybrid catalyst impregnated LSCF cathode show a polarization resistance of $0.25 \Omega \text{ cm}^2$, about one fifth of that the cells with the blank LSCF cathode ($1.03 \Omega \text{ cm}^2$). EIS and ECR analysis shows that the oxygen-ion transfer and oxygen dissociation-absorption processes in the LSCF cathode can be substantially accelerated by the impregnation of hybrid catalyst, resulting in significantly lower polarization resistance and larger MPD. In addition, the hybrid catalyst shows good chemical and microstructural stability at 873 K. Consequently, single cells with impregnated LSCF show excellent durability. This study demonstrates that impregnation of hybrid catalyst is a promising approach to improve the performance and durability of LSCF cathode for H-SOFCs.

CHAPTER 6 AN EFFICIENT AND HIGH-SELECTIVITY CHROMIUM GETTER FOR SOLID OXIDE FUEL CELLS

6.1 BACKGROUND

Solid oxide fuel cell (SOFC), as a promising technology for electricity generation, has received significant attention in recent decades thanks to its high energy-conversion efficiency, its status as being environmental friendly, wide application range and fuel flexibility [137]. Traditional SOFCs are usually operated at a high temperature (850°C-1000°C). However, the high operating temperature means that the components of stack need to be mainly ceramic and high temperature metal alloys, which increases the cost of the system and hinders their broad commercialization. Therefore, significant costs have been paid to reduce the operating temperature of SOFCs to 500°C-750°C [140, 166-168]. In this temperature range, low cost metallic interconnect materials, instead of ceramic and high temperature metal alloys, can be applied in SOFC stack. To date, promising candidates for metallic interconnects are all Cr-containing alloys [38, 169].

However, the volatilization of gaseous Cr-species from the Cr-containing alloys leads to the Cr poisoning and performance degradation in the cathode of SOFC, which becomes a serious issue in SOFC development [170]. The Cr poisoning mechanisms in different cathode materials, such as LSCF and LSM, have been summarized by Jiang et al. [171]. In LSM, Mn^{2+} ions are generated during cathode polarization at high temperature, which serve as the nucleation agent to react with gaseous Cr-species. While in LSCF, SrO,

segregated from LSCF crystal, serves as the nucleation agent to react with gaseous Cr-species [171].

Several approaches have been proposed and evaluated in order to mitigate or avoid the effect of Cr poisoning on the cathode. One of these approaches is modifying the composition of cathode material to improve the structural stability and reduce the surface segregation. It has been reported that replacing Sr with Ba in LSCF could improve the Cr tolerability[172]. However, the formation of SrCrO_4 , BaCrO_4 and MnCrO_4 is thermodynamically favorable above 973 K [173], so the effect of replacing Sr with Ba in LSCF is still unknown in the long term. To completely avoid Cr poisoning, Sr, Mn, Ba-free cathode materials, such as $\text{LaNi}_{0.6}\text{Fe}_{0.4}\text{O}_3$, have been developed. Komatsu *et al.* have reported that the chemical reaction between $\text{LaNi}_{0.6}\text{Fe}_{0.4}\text{O}_3$ and Cr_2O_3 can be neglected in 1000 h, suggesting the excellent Cr tolerance of $\text{LaNi}_{0.6}\text{Fe}_{0.4}\text{O}_3$ [174]. However, the electrochemical performance of $\text{LaNi}_{0.6}\text{Fe}_{0.4}\text{O}_3$ is a concern below 973K. Another approach of mitigating Cr poisoning is surface modification of cathode by impregnation. Zhao *et al.* have reported that impregnation of $\text{Gd}_{0.1}\text{Ce}_{0.9}\text{O}_{1.95}$ (GDC) can improve the Cr-tolerance of LSCF, because GDC coating could act as a buffer layer to avoid the direct contact between the SrO nucleus and Cr species[27]. Moreover, it has also been reported that the impregnation of BaO in LSCF can inhibit the formation of SrCrO_4 by forming thermodynamically stable and conductive BaCrO_4 [175]. Beside the modification of composition or surface of cathode, adding a protective layer on the surface of metallic alloy is also an effective method to inhibit the evaporation/migration of Cr-species to the cathode [169, 176].

Recently, mitigating Cr poisoning by introducing “chromium getter” has been proposed and investigated [40, 41, 177]. The chromium getter materials can capture (react) the Cr species before the interaction of Cr species and the cathode in SOFC. Chromium getter can be looked as a filter layer for Cr species and it can be reloaded before its complete failure. Chromium getter materials are required to possess high reaction activity with Cr species, good chemical stability in operation condition and good chemical and physical compatibility with other components of SOFC system. To date, only $Sr_xNi_yO_z$ has been evaluated as chromium getter in SOFC. But it has been demonstrated that $Sr_xNi_yO_z$ decomposes into SrO and NiO at temperatures higher than 1223 K [40]. Meanwhile, chemical instability of $Sr_xNi_yO_z$ in H_2O and CO_2 , which could be present in the stream gas of cathode, limits its practical application.

By contrast, $Sr_2Fe_{1.5}Mo_{0.5}O_{6-\delta}$ (SFM) possesses excellent stability in a wide temperature range (up to 1623 K) [67] and has been demonstrated to be stable in an atmosphere containing H_2O and CO_2 in our previous studies [115, 178]. Moreover, the perovskite structure of SFM makes it chemically and physically compatible with most cathode materials also with perovskite structure. Most importantly, according to the thermodynamics ($2SrO + Cr_2O_3 + 1.5O_2 = 2SrCrO_4$, $\Delta G = -310 \text{ kJ mol}^{-1}$ at 1073 K), SFM may have high reactivity with Cr species because of its high content of Sr. Therefore, in the study, SFM is evaluated as a new chromium getter material for SOFC.

6. 2 EXPERIMENTAL

6.2.1 SYNTHESIS AND CHARACTERIZATION OF MATERIALS

The SFM powders were synthesized by a glycine and citric acid assisted combustion method [67].

To evaluate the chemical reaction between Cr₂O₃ (Alfa Aesar 99%) and SFM, X-ray diffraction (Rigaku MiniFlex II, with Cu K α radiation and a D/teX silicon strip detector) was used to identify the crystal structures of sample after treatment.

The SFM getter before and after test was analyzed by X-ray Photoelectron Spectrometer (XPS) (Kratos Axis Ultra) and the spectra were calibrated by C 1 at 284.5 eV.

5.2.2 FABRICATION OF SYMMETRICAL CELLS AND SFM POROUS PELLETS

Dense electrolyte support was prepared by pressing GDC10 (Fuel Cell Materials, USA) powders into pellets and then sintering at 1723 K for 5 h. After sintering, the GDC pellet is 16.8 mm in diameter and 0.63 mm in thickness. The LSCF electrode ink (Fuel Cell Materials, USA) was screen-printed on both sides of the GDC10 electrolyte and then fired at 1273 K for 2 h. The effective electrode area was about 0.33 cm². Ag paste was used as the current collector.

SFM, as synthesized above, and carbon black are mixed with weight ratio of 5:1. The mixed powder is pressed into pellets. After sintering at 1373 K for 2 h, porous SFM pellets are obtained.

5.2.3 ELECTROCHEMICAL TEST OF THE SYMMETRICAL CELLS

The prepared single cells were attached onto the end of an alumina tube using high temperature ceramic adhesives (552-1105, Aremco, USA) as sealing material. Cr₂O₃ and SFM getter were put inside the alumina tube as shown in Fig. 6.01. During test, 50 ml min⁻¹ dry O₂ was fed to electrode side with Cr₂O₃ and SFM. The flow rate was controlled by mass flow controllers (APEX, Schoonover, USA). Impedance spectra measurements for the symmetrical cells were conducted on an electrochemical test

system (IM6, Zahner-elektrik, Kronach, Germany). The frequency range was from 1 MHz to 0.01 Hz with the AC amplitude of 30 mV. Z-view was used to simulate the impedance spectra.

Microstructures of the single cells before and after the electrochemical test were examined by scanning electron microscope (SEM, Zeiss Ultra Plus FESEM).

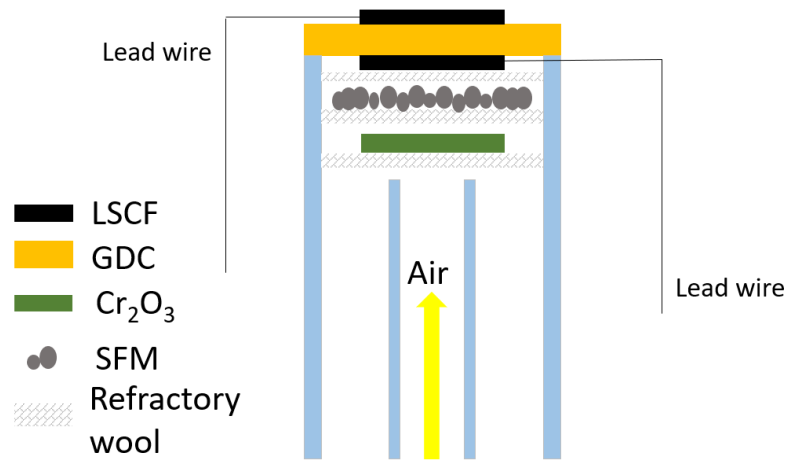


Figure 6.01 The schematic of test setup.

6.3 RESULT AND DISCUSSIONS

SFM and Cr₂O₃ are characterized by XRD, as shown in Fig. 6.02. The XRD pattern of SFM reveals perovskite structure without any secondary phase, suggesting that single phase SFM has been synthesized successfully. Meanwhile, the XRD pattern of Cr₂O₃ shows hexagonal structure without any secondary phase.

Fig. 6.03 displays the XRD patterns of SFM before and after different treatment. It can be found that the XRD patterns of SFM do not change after treatment in CO₂ or 20% H₂O-air at 1073 K, indicating that SFM is chemically stable in an atmosphere containing CO₂ or H₂O. These results are consistent with literatures [25, 79, 178].

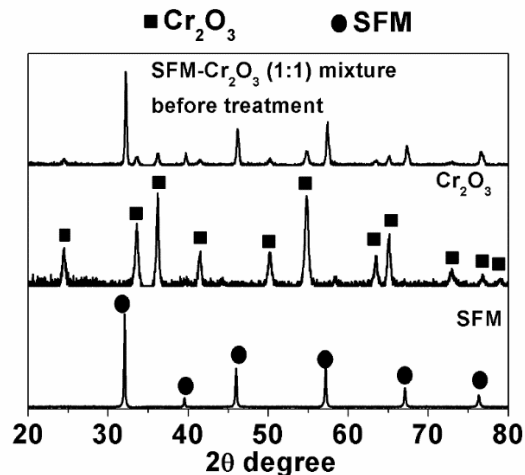


Figure 6.02 The XRD patterns of SFM, Cr₂O₃ and mixture (1:1) before treatment.

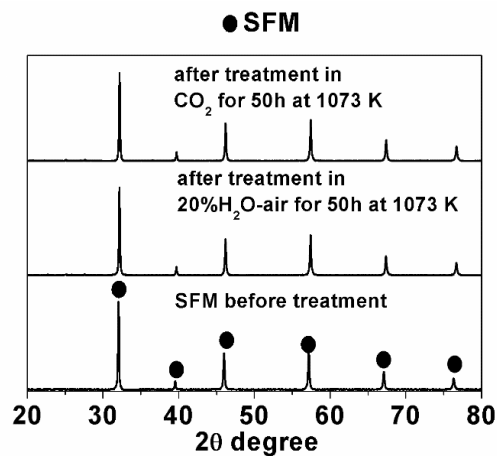


Figure 6.03 The XRD patterns of SFM after CO₂ and H₂O treatment.

To evaluate the reaction activity between SFM and Cr₂O₃, SFM and Cr₂O₃ are mixed with a weight ratio of 1:1 and 10:1. In the cases of weight ratios of 1:1, since the mole of SFM (402.98 g mol⁻¹) is smaller than that of Cr₂O₃ (151.99 g mol⁻¹), there is extra Cr₂O₃ in the mixture. The XRD patterns of mixture with a weight ratio of 1:1 are shown in Fig. 6.04. In Fig. 6.04 (a), after treatment at 1223 K for 20 h, SFM phase disappears and the peaks corresponding to SrCrO₄ are obvious, indicating that SFM completely decomposes and reacts with Cr₂O₃ thoroughly. Besides SrCrO₄ and Cr₂O₃ phase, it is hard to accurately

figure out the phase of other products, because the XRD pattern is complicated and peaks are overlapped. When the temperature of treatment is reduced by 100 K, the XRD pattern of 1123 K is similar to that of 1223 K. Figure 6.04 (b) shows that even the temperature of treatment drops to 923 K, SFM phase cannot be found and peaks belonging to SrCrO₄ is still obvious. These XRD results indicate that SFM has high reaction activity with Cr species in this temperate range, implying that SFM may be a good potential chromium getter material.

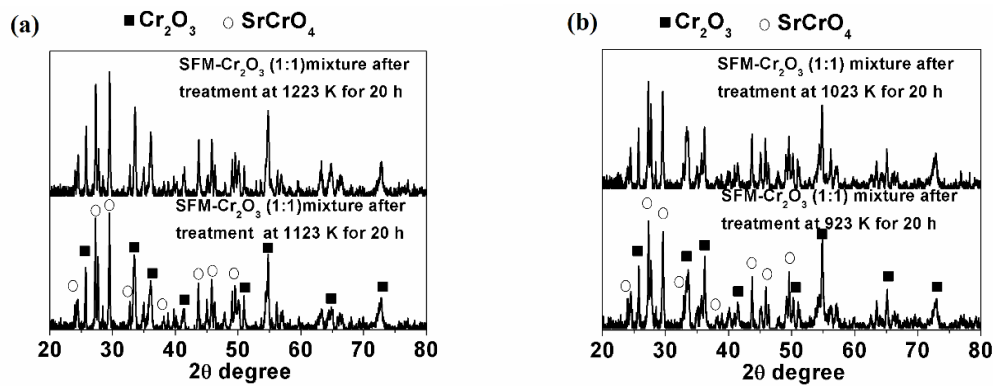


Figure 6.04 The XRD patterns of SFM-Cr₂O₃ mixture (1:1) after treatment (a) at 1223 K and 1123 K; (b) at 1023 K and 923 K.

In practical application, to avoid the failure of Cr species capturing, the amount of getter is usually beyond that of Cr species, especially at the beginning of operation. So, the reaction activity test is also conducted when SFM and Cr₂O₃ are mixed with weight ratio of 10:1, as shown in Fig. 6.05. It can be seen that at 973 K and 1073 K, SFM and SrCrO₄ phases can be observed, demonstrating that when the amount of Cr species is tiny, SFM can still efficiently capture Cr species.

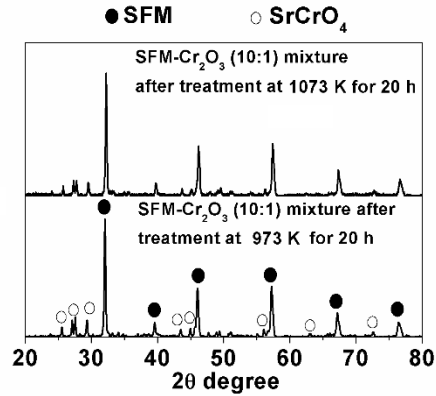


Figure 6.05 The XRD patterns of SFM-Cr₂O₃ mixture (10:1) after treatment at 973 K and 1073K.

To demonstrate the feasibility of SFM as chromium getter for SOFC, electrochemical performance of symmetrical cells in different test conditions is investigated as shown in Fig. 6.01. The results of impedance spectra are shown in Fig.6.06. The intercept of the real axis corresponds to ohmic resistance of the cell, while the real axis range covered by the arc region represents the overall electrode polarization resistance (R_p). In Fig. 6.06 (a), it can be seen that the polarization resistance is stable and it is just increased from $0.055 \Omega \text{ cm}^2$ to $0.060 \Omega \text{ cm}^2$ in 50 h. This slow degradation may be due to the evaporation of silver current collector or the Sr segregation on the surface [156, 179].

When Cr source (Cr₂O₃) is introduced to one side of the symmetrical cells, the impedance spectra are shown in Fig. 6.06 (b). The impedance spectrum at 0 h is not identical with that in the case without Cr sources (Fig. 6.06 (a)), which can be explained by the fact that the volatilization of Cr source and Cr poisoning already occurs during the slow heating process (the heating rate is 2 K min^{-1}). At 50 h, significant increase of polarization resistance is found. It increases from $0.083 \Omega \text{ cm}^2$ at 0 h to $0.218 \Omega \text{ cm}^2$ at 50

h. In other words, LSCF cathode suffers serious performance degradation due to Cr poisoning at 1073 K, which is consistent with those in literatures[172, 180].

To mitigate the effect of Cr poisoning, a layer of SFM as Chromium getter is placed between the Cr source and the symmetrical cell, as shown in Fig. 6.01. The results of impedance spectra with Cr source and SFM layer are shown in Fig. 6.06 (c). It is obvious that the degradation of performance is significantly reduced with the introduction of SFM layer, compared with that without SFM layer. The polarization resistance is only increased from $0.055 \Omega \text{ cm}^2$ at 0 h to $0.070 \Omega \text{ cm}^2$ at 50 h. The degradation rate in the case with Cr source and SFM layer is a bit larger than that without Cr source, which may be due to the incomplete absorption of gaseous Cr species by SFM layer.

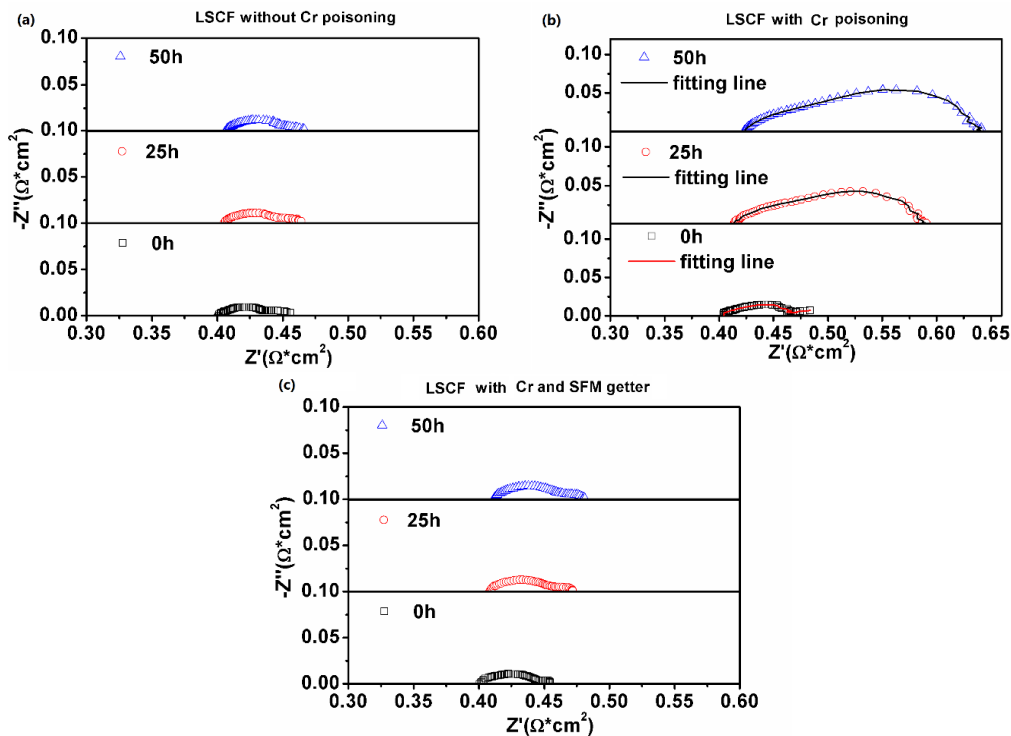


Figure 6.06 Impedance spectra of LSCF at 1073 K (a) Blank; (b) with Cr_2O_3 ; (c) with Cr_2O_3 and SFM getter.

Furthermore, to study how the Cr poisoning influences the performance of LSCF cathode, Zview program is used to fit the spectra in Fig. 6.06 (b) and the fitting results are

shown in Fig. 6.07. When equivalent circuit of $R_1(R_H QPE_H)(R_L QPE_L)$ is applied to fit the spectra, a good agreement is obtained between the fitting lines and the experimental data, where R represents the resistance, QPE is the constant phase element and the subscripts H and L correspond to the high and low-frequency arc, respectively. Two RQPE elements are used in equivalent circuit, implying that there are at least two rate-limiting steps. The fitting results of R_H and R_L at different time are summarized in Fig. 6.07.

It has been reported that oxygen ion transfer and oxygen dissociation-absorption processes are the two main rate-limiting factors for the oxygen reduction reaction (ORR) in LSCF. Moreover, the oxygen-ion transfer process generally corresponds to the $(R_H QPE_H)$ component in impedance spectra, while the oxygen dissociation-absorption process normally corresponds to the $(R_L QPE_L)$ component [181, 182].

From Fig. 6.07, it can be observed that the R_H and R_L are increased with time. The R_H is increased by 60.2% (from $0.0705 \Omega \text{ cm}^2$ to $0.113 \Omega \text{ cm}^2$) in 50 h, while the R_L is significantly increased by more than 700% (from $0.0131 \Omega \text{ cm}^2$ to $0.153 \Omega \text{ cm}^2$), suggesting that the Cr poisoning slows down both the oxygen-ion transfer and oxygen dissociation-absorption processes of LSCF, especially the latter. Atkinson *et al.* [183] have reported Cr poisoning reduces oxygen self-diffusion (D_o) and surface exchange (k_o) parameters, the latter being more affected. As k_o is highly related to the oxygen dissociation-absorption process in the LSCF electrode, the significant increase of R_L in this study could be blamed for the reduction of k_o caused by Cr poisoning.

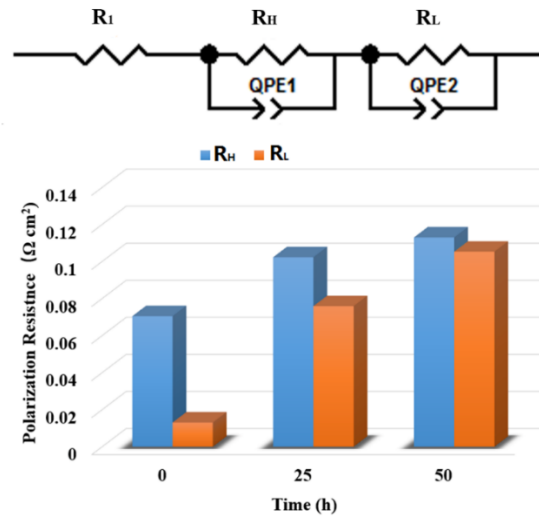


Figure 6.07 Equilibrium circuit and fitting results of impedance spectra in Fig. 6.06(b).

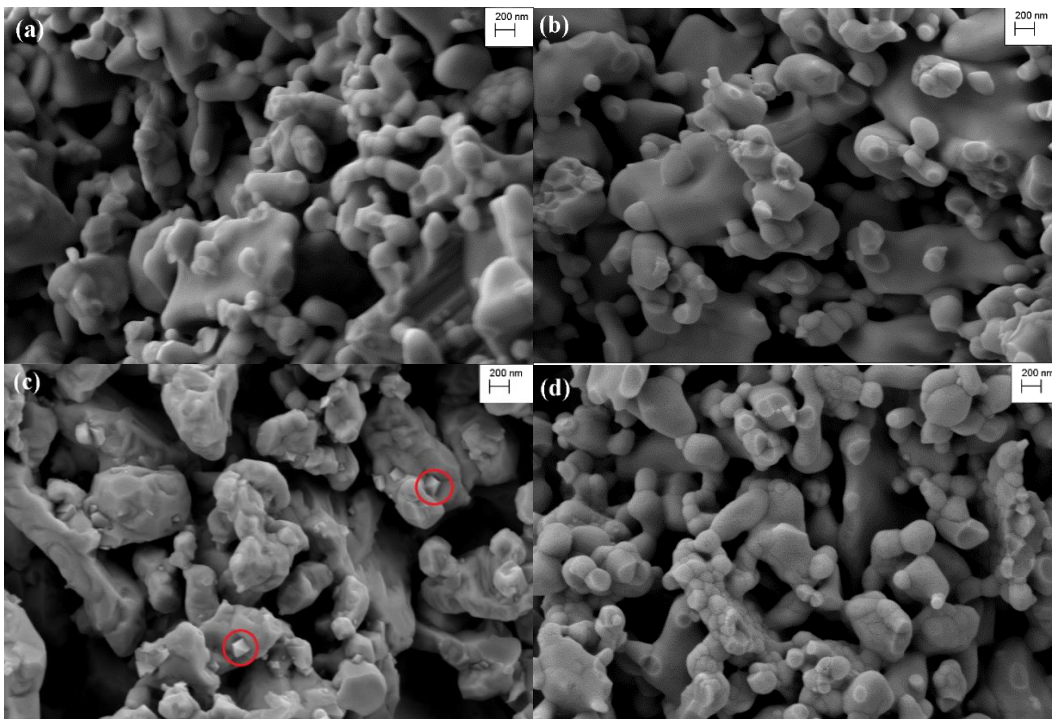


Figure 6.08 Microstructure characterization of LSCF (a) blank before test; (b) blank after test; (c) with Cr source; (d) with Cr source and SFM getter.

Moreover, the microstructures of LSCF electrode in different conditions are characterized by SEM, as shown in Fig. 6.08. Fig. 6.08(a) shows the microstructure of blank LSCF electrode before the test. The LSCF electrode before the test shows porous

structure and the size of the particles ranges from 100 nm to 500 nm, which are the typical features of LSCF electrode. The microstructure of blank LSCF electrode after 50 h test is shown in Fig. 6.08 (b). Compared with blank LSCF before the test (Fig. 6.08 (a)), there is no obvious change after the test, indicating that the LSCF electrode is stable in microstructure during the test, which is consistent with impedance spectra in Fig. 6.06 (a).

Fig. 6.08 (c) shows the morphology of LSCF electrode with Cr source in the test. It is observable that some new crystals, highlighted by the red circles, are formed on the surface of particles. These new crystals are octahedral-type particles, similar to the SrCrO_4 phase observed in other literatures [175], indicating the Cr poisoning in LSCF. The formation of SrCrO_4 on the LSCF surface could greatly reduce reaction sites, leading to reduction of the kinetics of oxygen dissociation-absorption process. Furthermore, the extraction of Sr from LSCF by SrCrO_4 could destroy the crystal structure of LSCF, resulting in reduction of ion and electronic conductivity. Overall, the performance degradation caused by Cr poisoning can be explained by the change of microstructure. By contrast, when SFM layer is introduced between Cr source and symmetrical cells, these new crystals cannot be found in the LSCF electrode, as shown in Fig. 8 (d). Moreover, the microstructure in Fig. 6.08 (d) is similar to those in Fig. 6.08 (a) and (b), demonstrating that the SFM layer can efficiently mitigate the Cr poisoning in LSCF electrode. These microstructure characterizations are consistent with the results of electrochemical performance in Fig. 6.06.

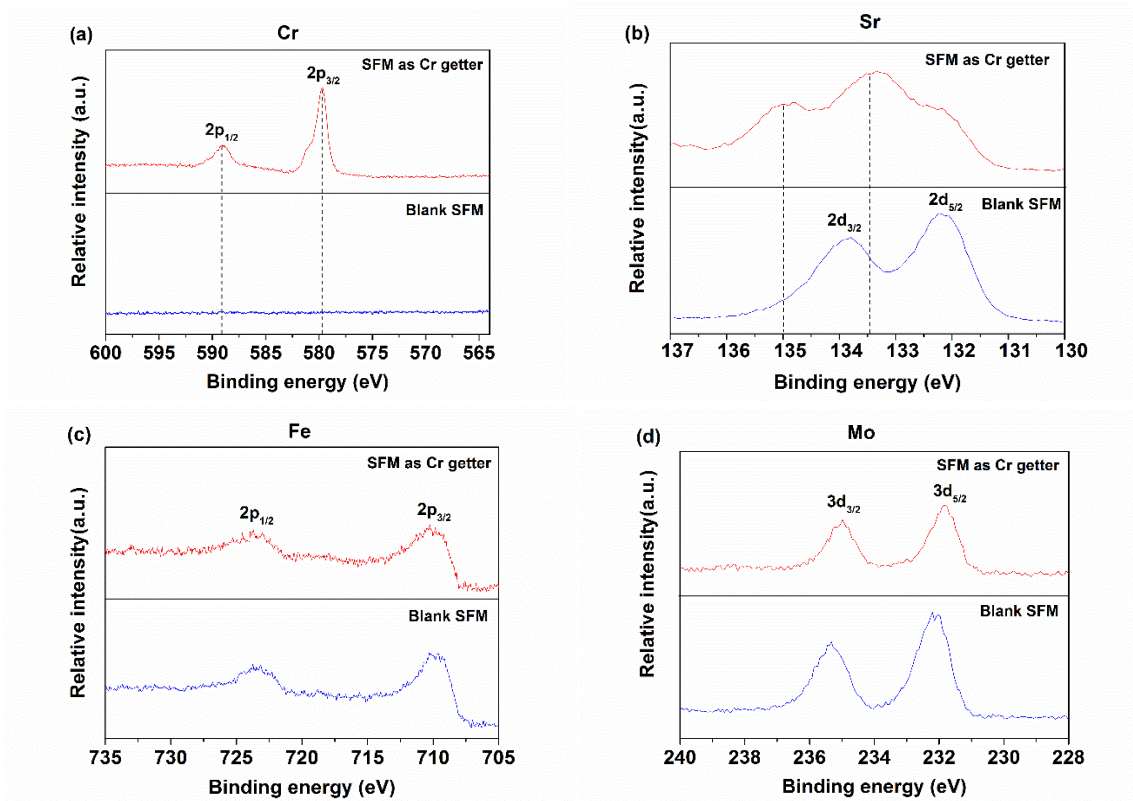


Figure 6.09 XPS spectra (a) Cr 2p; (b) Sr 3d; (c) Fe 2p; (d) Mo 3d.

To analyze the working mechanism of the SFM layer as Cr getter, the SFM layer after test (in Fig. 6.06 (c)) is analyzed by XPS, as shown in Fig. 6.09. Fig. 6.09 (a) shows the XPS spectra of Cr. It is clear that there is no Cr in the blank SFM sample. By contrast, peaks corresponding to Cr 2p can be found in the SFM layer as Cr getter. The binding energies of Cr 2p_{3/2} and 2p_{1/2} are about 580 eV and 589 eV respectively, which are similar to the typical binding energies of Cr in SrCrO₄ [184]. XPS spectra of Sr before and after test are compared in Fig. 6.09 (b) and significant changes can be found after test. After stability test, the XPS spectrum of Sr become complex, which is due to the existence of more than one phase on the surface of sample. Besides the original two peaks at 132 eV and 133.8 eV, two new peaks at about 133.5 eV and 135 eV can be observed after test. The binding energies of these two new peaks are close to those of Sr in SrCrO₄ reported in the

literature [184]. Fig. 6.09 (c) displays the XPS spectra of Fe before and after test. The spectra of Fe before and after test are similar and there are only slight shifts of the peaks. These slight shifts of peaks are probably due to the slight change of chemical environment of Fe, which can be explained by the partial separation of Sr from the crystal structure of SFM. The XPS spectra of Mo in Fig. 6.09 (d) have the similar changes with those of Fe, which can be explained by the same reason. Compared the significant change of XPS spectra of Sr, the unobvious changes of XPS spectra of Fe and Mo suggest that Fe and Mo have less reactivity with Cr species than Sr. This is consistent with result of XRD test in Fig. 6.05. The above results of XPS indicate that the working mechanism of SFM as Cr getter is primarily due to the high reactivity between Sr and Cr. This can be explained by the very negative Gibbs free energy of reaction between SrO and Cr₂O₃ ($O_2+2SrO+Cr_2O_3=2SrCrO_4$, $\Delta G=-310$ KJ at 1073 K).

6.4 CONCLUSIONS

In this work, a new Chromium getter material, SFM, is proposed and evaluated. The XRD results demonstrate that SFM, which is stable in an atmosphere containing CO₂ and H₂O, possesses high reaction activity with Cr species in temperature range from 923 K to 1223 K, suggesting its high reaction selectivity with Cr species. Then the results of electrochemical tests and microstructure characterizations show that the introduction of SFM layer can efficiently mitigate the performance degradation of LSCF caused by Cr poisoning. The function of SFM layer is sufficient absorption of gaseous Cr species to avoid the direct contact of LSCF and Cr species, which is demonstrated by the XPS test.

FUTURE WORK

1. Development of air electrode materials without alkaline earth elements

The volatilization of gaseous Cr-species from Cr containing interconnect materials leads to drastic degradation of the air electrode performance which becomes a serious issue in SOFC development. The perovskite-type air electrode materials usually contain alkaline earth elements which are thermodynamically favorable to react to Cr-species, leading to Cr poisoning of air electrode. Therefore, in my future work, air electrode materials without alkaline earth elements will be developed. The Cr-tolerance and electrochemical performance of them will be evaluated.

2. Development of high performance H-SOECs

In Chapter 4, H-SOECs with robust electrolyte and air electrode have been fabricated successfully. However, the electrolysis performance is still not satisfactory for practical applications. The ohmic resistance from the electrolyte layer and the polarization resistance from the air electrode are the limiting factors of the electrolysis performance. The ohmic resistance from electrolyte layer is closely related to the composition, microstructure and thickness of electrolyte material. The polarization resistance from air electrode is greatly affected by the electro-catalytic activity of electrode material, especially at low temperature (below 923 K). Therefore, in the future study, the electrolysis performance of H-SOECs will be improved by optimizing the electrolyte layer and developing high performance and stable air electrode with nano-scaled structure.

Moreover, the faradaic efficiency of H-SOECs is still a problem. Electrochemical model will be developed to study the mechanism of electronic leakage in the electrolyte layer. After well understanding the mechanism, various methods will be applied to increase the faradaic efficiency.

REFERENCES

- [1] Fu Q, Mabilat C, Zahid M, Brisse A, Gautier L. Syngas production via high-temperature steam/CO₂ co-electrolysis: an economic assessment. *Energy & Environmental Science*. 2010;3:1382-97.
- [2] Chen Y, Lin Y, Zhang Y, Wang S, Su D, Yang Z, et al. Low temperature solid oxide fuel Cells with hierarchically porous cathode nano-network. *Nano Energy*. 2014.
- [3] Cinti G, Baldinelli A, Di Michele A, Desideri U. Integration of solid oxide electrolyzer and Fischer-Tropsch: A sustainable pathway for synthetic fuel. *Applied Energy*. 2016;162:308-20.
- [4] Xie Y, Xiao J, Liu D, Liu J, Yang C. Electrolysis of carbon dioxide in a solid oxide electrolyzer with silver-gadolinium-doped ceria cathode. *Journal of The Electrochemical Society*. 2015;162:F397-F402.
- [5] Tao G, Sridhar K, Chan C. Study of carbon dioxide electrolysis at electrode/electrolyte interface: Part I. Pt/YSZ interface. *Solid state ionics*. 2004;175:615-9.
- [6] Stoots CM, Hartvigsen JJ, O'Brien JE, Herring JS. Syngas production via high-temperature coelectrolysis of steam and carbon dioxide. *Journal of fuel cell science and technology*. 2009;6:011014.
- [7] Ni M, Leung MK, Leung DY. Technological development of hydrogen production by solid oxide electrolyzer cell (SOEC). *International Journal of Hydrogen Energy*. 2008;33:2337-54.

- [8] Laguna-Bercero M. Recent advances in high temperature electrolysis using solid oxide fuel cells: A review. *Journal of Power sources*. 2012;203:4-16.
- [9] Ebbesen SD, Jensen SH, Hauch A, Mogensen MB. High temperature electrolysis in alkaline cells, solid proton conducting cells, and solid oxide cells. *Chemical reviews*. 2014;114:10697-734.
- [10] Lyagaeva J, Danilov N, Vdovin G, Bu J, Medvedev D, Demin A, et al. A new Dy-doped BaCeO₃-BaZrO₃ proton-conducting material as a promising electrolyte for reversible solid oxide fuel cells. *Journal of Materials Chemistry A*. 2016;4:15390-9.
- [11] Wang S, Kobayashi T, Dokiya M, Hashimoto T. Electrical and ionic conductivity of Gd-doped ceria. *Journal of the Electrochemical Society*. 2000;147:3606-9.
- [12] Eguchi K, Hatagishi T, Arai H. Power generation and steam electrolysis characteristics of an electrochemical cell with a zirconia-or ceria-based electrolyte. *Solid State Ionics*. 1996;86:1245-9.
- [13] Tanner CW, Virkar AV. Instability of BaCeO₃ in H₂O-containing atmospheres. *Journal of The Electrochemical Society*. 1996;143:1386-9.
- [14] Fabbri E, Pergolesi D, Traversa E. Materials challenges toward proton-conducting oxide fuel cells: a critical review. *Chem Soc Rev*. 2010;39:4355-69.
- [15] Yoo Y, Lim N. Performance and stability of proton conducting solid oxide fuel cells based on yttrium-doped barium cerate-zirconate thin-film electrolyte. *Journal of Power Sources*. 2013;229:48-57.
- [16] Duan C, Tong J, Shang M, Nikodemski S, Sanders M, Ricote S, et al. Readily processed protonic ceramic fuel cells with high performance at low temperatures. *Science*. 2015;349:1321-6.

- [17] Bi L, Shafi SP, Traversa E. Y-doped BaZrO₃ as a chemically stable electrolyte for proton-conducting solid oxide electrolysis cells (SOECs). *Journal of Materials Chemistry A*. 2015;3:5815-9.
- [18] Bi L, Boulfrad S, Traversa E. Steam electrolysis by solid oxide electrolysis cells (SOECs) with proton-conducting oxides. *Chem Soc Rev*. 2014;43:8255-70.
- [19] Liang M, Yu B, Wen M, Chen J, Xu J, Zhai Y. Preparation of LSM–YSZ composite powder for anode of solid oxide electrolysis cell and its activation mechanism. *Journal of Power Sources*. 2009;190:341-5.
- [20] Yang C, Jin C, Coffin A, Chen F. Characterization of infiltrated (La_{0.75}Sr_{0.25})_{0.95}MnO₃ as oxygen electrode for solid oxide electrolysis cells. *International Journal of Hydrogen Energy*. 2010;35:5187-93.
- [21] Keane M, Mahapatra MK, Verma A, Singh P. LSM–YSZ interactions and anode delamination in solid oxide electrolysis cells. *International Journal of Hydrogen Energy*. 2012;37:16776-85.
- [22] Graves C, Ebbesen SD, Jensen SH, Simonsen SB, Mogensen MB. Eliminating degradation in solid oxide electrochemical cells by reversible operation. *Nature Materials*. 2014.
- [23] Fan H, Keane M, Singh P, Han M. Electrochemical performance and stability of lanthanum strontium cobalt ferrite oxygen electrode with gadolinia doped ceria barrier layer for reversible solid oxide fuel cell. *Journal of Power Sources*. 2014.
- [24] Marina OA, Pederson LR, Williams MC, Coffey GW, Meinhardt KD, Nguyen CD, et al. Electrode performance in reversible solid oxide fuel cells. *Journal of the Electrochemical Society*. 2007;154:B452-B9.

- [25] Wang Y, Liu T, Fang S, Chen F. Syngas production on a symmetrical solid oxide H₂O/CO₂ co-electrolysis cell with Sr₂Fe_{1.5}Mo_{0.5}O₆-Sm_{0.2}Ce_{0.8}O_{1.9} electrodes. *Journal of Power Sources*. 2016;305:240-8.
- [26] Liu R, Kim S, Taniguchi S, Oshima T, Shiratori Y, Ito K, et al. Influence of water vapor on long-term performance and accelerated degradation of solid oxide fuel cell cathodes. *Journal of Power Sources*. 2011;196:7090-6.
- [27] Zhao L, Amarasinghe S, Jiang SP. Enhanced chromium tolerance of La_{0.6}Sr_{0.4}Co_{0.2}Fe_{0.8}O_{3-δ} electrode of solid oxide fuel cells by Gd_{0.1}Ce_{0.9}O_{1.95} impregnation. *Electrochemistry Communications*. 2013;37:84-7.
- [28] Stoots C, O'Brien J, Hartvigsen J. Results of recent high temperature coelectrolysis studies at the Idaho National Laboratory. *International Journal of Hydrogen Energy*. 2009;34:4208-15.
- [29] Yang C, Li J, Newkirk J, Baish V, Hu R, Chen Y, et al. Co-electrolysis of H₂O and CO₂ in a solid oxide electrolysis cell with hierarchically structured porous electrodes. *Journal of Materials Chemistry A*. 2015;3:15913-9.
- [30] Jensen SH, Larsen PH, Mogensen M. Hydrogen and synthetic fuel production from renewable energy sources. *International Journal of Hydrogen Energy*. 2007;32:3253-7.
- [31] Xing R, Wang Y, Zhu Y, Liu S, Jin C. Co-electrolysis of steam and CO₂ in a solid oxide electrolysis cell with La_{0.75}Sr_{0.25}Cr_{0.5}Mn_{0.5}O_{3-δ}-Cu ceramic composite electrode. *Journal of Power Sources*. 2015;274:260-4.
- [32] Zhu WZ, Deevi S. Development of interconnect materials for solid oxide fuel cells. *Materials Science and Engineering: A*. 2003;348:227-43.

- [33] Primdahl S, Hansen J, Grahl-Madsen L, Larsen P. Sr-doped LaCrO_3 anode for solid oxide fuel cells. *Journal of the Electrochemical Society*. 2001;148:A74-A81.
- [34] Li Y, Gan Y, Wang Y, Xie K, Wu Y. Composite cathode based on Ni-loaded $\text{La}_{0.75}\text{Sr}_{0.25}\text{Cr}_{0.5}\text{Mn}_{0.5}\text{O}_{3-\delta}$ for direct steam electrolysis in an oxide-ion-conducting solid oxide electrolyzer. *International Journal of Hydrogen Energy*. 2013;38:10196-207.
- [35] Canales-Vázquez J, Smith MJ, Irvine JT, Zhou W. Studies on the Reorganization of Extended Defects with Increasing n in the Perovskite-Based $\text{La}_4\text{Sr}_{n-4}\text{Ti}_n\text{O}_{3n+2}$ Series. *Advanced Functional Materials*. 2005;15:1000-8.
- [36] Xie K, Zhang Y, Meng G, Irvine JT. Direct synthesis of methane from $\text{CO}_2/\text{H}_2\text{O}$ in an oxygen-ion conducting solid oxide electrolyser. *Energy & Environmental Science*. 2011;4:2218-22.
- [37] Yoon S-E, Song S-H, Choi J, Ahn J-Y, Kim B-K, Park J-S. Coelectrolysis of steam and CO_2 in a solid oxide electrolysis cell with ceramic composite electrodes. *International Journal of Hydrogen Energy*. 2014;39:5497-504.
- [38] Jiang SP, Chen X. Chromium deposition and poisoning of cathodes of solid oxide fuel cells – A review. *International Journal of Hydrogen Energy*. 2014;39:505-31.
- [39] Chen X, Zhen Y, Li J, Jiang SP. Chromium deposition and poisoning in dry and humidified air at $(\text{La}_{0.8}\text{Sr}_{0.2})_{0.9}\text{MnO}_{3+\delta}$ cathodes of solid oxide fuel cells. *International Journal of Hydrogen Energy*. 2010;35:2477-85.
- [40] Aphale AN, Uddin MA, Hu B, Liang C, Webster J, Singh P. Chemical and structural stability of $\text{Sr}_x\text{Ni}_y\text{O}_z$ Chromium getter for application in SOFC systems. *ECS Transactions*. 2017;78:1073-81.

- [41] Uddin MA, Aphale A, Hu B, Heo SJ, Pasaogullari U, Singh P. Electrochemical validation of In-cell chromium getters to mitigate chromium poisoning in SOFC stack. *Journal of The Electrochemical Society*. 2017;164:F1342-F7.
- [42] Kim-Lohsoontorn P, Bae J. Electrochemical performance of solid oxide electrolysis cell electrodes under high-temperature coelectrolysis of steam and carbon dioxide. *Journal of Power Sources*. 2011;196:7161-8.
- [43] Zhan Z, Kobsiriphat W, Wilson JR, Pillai M, Kim I, Barnett SA. Syngas production by coelectrolysis of CO₂/H₂O: the basis for a renewable energy cycle. *Energy & Fuels*. 2009;23:3089-96.
- [44] Martinez-Frias J, Pham A-Q, M Aceves S. A natural gas-assisted steam electrolyzer for high-efficiency production of hydrogen. *International Journal of Hydrogen Energy*. 2003;28:483-90.
- [45] Wang W, Vohs JM, Gorte RJ. Hydrogen production via CH₄ and CO assisted steam electrolysis. *Topics in Catalysis*. 2007;46:380-5.
- [46] Wang W, Gorte RJ, Vohs JM. Analysis of the performance of the electrodes in a natural gas assisted steam electrolysis cell. *Chemical Engineering Science*. 2008;63:765-9.
- [47] Fang S, Wang S, Brinkman KS, Su Q, Wang H, Chen F. Relationship between fabrication method and chemical stability of Ni–BaZr_{0.8}Y_{0.2}O_{3-δ} membrane. *Journal of Power Sources*. 2015;278:614-22.
- [48] Molina A, Mondragon F. Reactivity of coal gasification with steam and CO₂. *Fuel*. 1998;77:1831-9.
- [49] Irfan MF, Usman MR, Kusakabe K. Coal gasification in CO₂ atmosphere and its kinetics since 1948: A brief review. *Energy*. 2011;36:12-40.

- [50] Gong Y, Huang K. Study of a renewable biomass fueled SOFC: The effect of catalysts. *International Journal of Hydrogen Energy*. 2013;38:16518-23.
- [51] Kaklidis N, Kyriakou V, Garagounis I, Arenillas A, Menéndez J, Marnellos G, et al. Effect of carbon type on the performance of a direct or hybrid carbon solid oxide fuel cell. *RSC Advances*. 2014;4:18792-800.
- [52] Lee AC, Mitchell RE, Gür TM. Thermodynamic analysis of gasification-driven direct carbon fuel cells. *Journal of Power Sources*. 2009;194:774-85.
- [53] Li S, Lee AC, Mitchell RE, Gür TM. Direct carbon conversion in a helium fluidized bed fuel cell. *Solid State Ionics*. 2008;179:1549-52.
- [54] Liu R, Zhao C, Li J, Zeng F, Wang S, Wen T, et al. A novel direct carbon fuel cell by approach of tubular solid oxide fuel cells. *Journal of Power Sources*. 2010;195:480-2.
- [55] Tang Y, Liu J. Effect of anode and Boudouard reaction catalysts on the performance of direct carbon solid oxide fuel cells. *International Journal of Hydrogen Energy*. 2010;35:11188-93.
- [56] Wu Y, Su C, Zhang C, Ran R, Shao Z. A new carbon fuel cell with high power output by integrating with in situ catalytic reverse Boudouard reaction. *Electrochemistry Communications*. 2009;11:1265-8.
- [57] Xie Y, Cai W, Xiao J, Tang Y, Liu J, Liu M. Electrochemical gas–electricity cogeneration through direct carbon solid oxide fuel cells. *Journal of Power Sources*. 2015;277:1-8.
- [58] Xie Y, Tang Y, Liu J. A verification of the reaction mechanism of direct carbon solid oxide fuel cells. *Journal of Solid State Electrochemistry*. 2013;17:121-7.

- [59] Zhang L, Xiao J, Xie Y, Tang Y, Liu J, Liu M. Behavior of strontium-and magnesium-doped gallate electrolyte in direct carbon solid oxide fuel cells. *Journal of Alloys and Compounds*. 2014;608:272-7.
- [60] Gür TM. Critical review of carbon conversion in “carbon fuel cells”. *Chem Rev*. 2013;113:6179-206.
- [61] Jiao Y, Tian W, Chen H, Shi H, Yang B, Li C, et al. In situ catalyzed Boudouard reaction of coal char for solid oxide-based carbon fuel cells with improved performance. *Applied Energy*. 2015;141:200-8.
- [62] Duan N-Q, Tan Y, Yan D, Jia L, Chi B, Pu J, et al. Biomass carbon fueled tubular solid oxide fuel cells with molten antimony anode. *Applied Energy*. 2016;165:983-9.
- [63] Gopalan S, Ye G, Pal UB. Regenerative, coal-based solid oxide fuel cell-electrolyzers. *Journal of Power Sources*. 2006;162:74-80.
- [64] Alexander BR, Mitchell RE, Gür TM. Steam-carbon fuel cell concept for cogeneration of hydrogen and electrical power. *Journal of The Electrochemical Society*. 2011;158:B505-B13.
- [65] Lee AC, Mitchell RE, Gür TM. Feasibility of hydrogen production in a steam-carbon electrochemical cell. *Solid State Ionics*. 2011;192:607-10.
- [66] Ewan BC, Adeniyi OD. A Demonstration of Carbon-Assisted Water Electrolysis. *Energies*. 2013;6:1657-68.
- [67] Liu Q, Dong X, Xiao G, Zhao F, Chen F. A novel electrode material for symmetrical SOFCs. *Advanced Materials*. 2010;22:5478-82.

- [68] Chen Y, Zhang Y, Xiao G, Yang Z, Han M, Chen F. Sulfur-Tolerant Hierarchically Porous Ceramic Anode-Supported Solid-Oxide Fuel Cells with Self-Precipitated Nanocatalyst. *ChemElectroChem*. 2015;2:672-8.
- [69] Liu Q, Bugaris DE, Xiao G, Chmara M, Ma S, zur Loye H-C, et al. $\text{Sr}_2\text{Fe}_{1.5}\text{Mo}_{0.5}\text{O}_{6-\delta}$ as a regenerative anode for solid oxide fuel cells. *Journal of Power Sources*. 2011;196:9148-53.
- [70] Xiao G, Liu Q, Zhao F, Zhang L, Xia C, Chen F. $\text{Sr}_2\text{Fe}_{1.5}\text{Mo}_{0.5}\text{O}_6$ as cathodes for intermediate-temperature solid oxide fuel cells with $\text{La}_{0.8}\text{Sr}_{0.2}\text{Ga}_{0.87}\text{Mg}_{0.13}\text{O}_3$ electrolyte. *Journal of The Electrochemical Society*. 2011;158:B455-B60.
- [71] He B, Zhao L, Song S, Liu T, Chen F, Xia C. $\text{Sr}_2\text{Fe}_{1.5}\text{Mo}_{0.5}\text{O}_{6-\delta}\text{-Sm}_{0.2}\text{Ce}_{0.8}\text{O}_{1.9}$ Composite Anodes for Intermediate-Temperature Solid Oxide Fuel Cells. *Journal of The Electrochemical Society*. 2012;159:B619-B26.
- [72] Zhang L, Liu Y, Zhang Y, Xiao G, Chen F, Xia C. Enhancement in surface exchange coefficient and electrochemical performance of $\text{Sr}_2\text{Fe}_{1.5}\text{Mo}_{0.5}\text{O}_6$ electrodes by $\text{Ce}_{0.8}\text{Sm}_{0.2}\text{O}_{1.9}$ nanoparticles. *Electrochemistry communications*. 2011;13:711-3.
- [73] Ni M, Leung MK, Leung DY. Energy and exergy analysis of hydrogen production by solid oxide steam electrolyzer plant. *International Journal of Hydrogen Energy*. 2007;32:4648-60.
- [74] Zhang H, Lin G, Chen J. Evaluation and calculation on the efficiency of a water electrolysis system for hydrogen production. *International Journal of Hydrogen Energy*. 2010;35:10851-8.

- [75] Luo Y, Shi Y, Li W, Ni M, Cai N. Elementary reaction modeling and experimental characterization of solid oxide fuel-assisted steam electrolysis cells. *International Journal of Hydrogen Energy*. 2014;39:10359-73.
- [76] Cheng Z, Zha S, Liu M. Stability of materials as candidates for sulfur-resistant anodes of solid oxide fuel cells. *Journal of The Electrochemical Society*. 2006;153:A1302-A9.
- [77] Gan Y, Zhang J, Li Y, Li S, Xie K, Irvine JTS. Composite Oxygen Electrode Based on LSCM for Steam Electrolysis in a Proton Conducting Solid Oxide Electrolyzer. *Journal of the Electrochemical Society*. 2012;159:F763-F7.
- [78] Im H-N, Jeon S-Y, Lim D-K, Singh B, Choi M, Yoo Y-S, et al. Steam/CO₂ Co-Electrolysis Performance of Reversible Solid Oxide Cell with La_{0.6}Sr_{0.4}Co_{0.2}Fe_{0.8}O_{3-δ}-Gd_{0.1}Ce_{0.9}O_{2-δ} Oxygen Electrode. *Journal of The Electrochemical Society*. 2015;162:F54-F9.
- [79] Li Y, Li P, Hu B, Xia C. A nanostructured ceramic fuel electrode for efficient CO₂/H₂O electrolysis without safe gas. *Journal of Materials Chemistry A*. 2016;4:9236-43.
- [80] Bidrawn F, Kim G, Corre G, Irvine J, Vohs JM, Gorte RJ. Efficient reduction of CO₂ in a solid oxide electrolyzer. *Electrochemical and Solid-State Letters*. 2008;11:B167-B70.
- [81] Graves C, Ebbesen SD, Mogensen M, Lackner KS. Sustainable hydrocarbon fuels by recycling CO₂ and H₂O with renewable or nuclear energy. *Renewable and Sustainable Energy Reviews*. 2011;15:1-23.
- [82] Becker W, Braun R, Penev M, Melaina M. Production of Fischer–Tropsch liquid fuels from high temperature solid oxide co-electrolysis units. *Energy*. 2012;47:99-115.

- [83] Wang Z, Mori M, Araki T. Steam electrolysis performance of intermediate-temperature solid oxide electrolysis cell and efficiency of hydrogen production system at 300 Nm 3 h⁻¹. *International Journal of Hydrogen Energy*. 2010;35:4451-8.
- [84] Enger BC, Holmen A. Nickel and Fischer-Tropsch Synthesis. *Catalysis Reviews*. 2012;54:437-88.
- [85] Li W, Wang H, Shi Y, Cai N. Performance and methane production characteristics of H₂O–CO₂ co-electrolysis in solid oxide electrolysis cells. *International Journal of Hydrogen Energy*. 2013;38:11104-9.
- [86] Chen L, Chen F, Xia C. Direct synthesis of methane from CO₂–H₂O co-electrolysis in tubular solid oxide electrolysis cells. *Energy & Environmental Science*. 2014;7:4018-22.
- [87] Moyer CJ, Sullivan NP, Zhu H, Kee RJ. Polarization characteristics and chemistry in reversible tubular solid-oxide cells operating on mixtures of H₂, CO, H₂O, and CO₂. *Journal of The Electrochemical Society*. 2011;158:B117-B31.
- [88] Yang C, Jin C, Chen F. Performances of micro-tubular solid oxide cell with novel asymmetric porous hydrogen electrode. *Electrochimica Acta*. 2010;56:80-4.
- [89] Kleiminger L, Li T, Li K, Kelsall G. CO₂ splitting into CO and O₂ in micro-tubular solid oxide electrolyzers. *RSC Advances*. 2014;4:50003-16.
- [90] Shi Y, Luo Y, Cai N, Qian J, Wang S, Li W, et al. Experimental characterization and modeling of the electrochemical reduction of CO₂ in solid oxide electrolysis cells. *Electrochimica acta*. 2013;88:644-53.

- [91] Kleiminger L, Li T, Li K, Kelsall G. Syngas (CO-H₂) production using high temperature micro-tubular solid oxide electrolyzers. *Electrochimica Acta*. 2015;179:565-77.
- [92] Li Y, Chen L, Zhang L, Xia C. Millimeter tubular solid oxide electrolysis cells with modified asymmetric hydrogen electrode. *International Journal of Hydrogen Energy*. 2016;41:5209-14.
- [93] Liu T, Ren C, Fang S, Wang Y, Chen F. Microstructure Tailoring of the Nickel Oxide–Yttria-Stabilized Zirconia Hollow Fibers toward High-Performance Microtubular Solid Oxide Fuel Cells. *ACS applied materials & interfaces*. 2014;6:18853-60.
- [94] Liu T, Wang Y, Ren C, Fang S, Mao Y, Chen F. Novel light-weight, high-performance anode-supported microtubular solid oxide fuel cells with an active anode functional layer. *Journal of Power Sources*. 2015;293:852-8.
- [95] Lei L, Bai Y, Liu Y, Liu J. An investigation on dip-coating technique for fabricating anode-supported solid oxide fuel cells. *Int J Appl Ceram Tech*. 2015;12:351-7.
- [96] Yue X, Irvine JT. Alternative cathode material for CO₂ reduction by high temperature solid oxide electrolysis cells. *Journal of The Electrochemical Society*. 2012;159:F442-F8.
- [97] Ebbesen SD, Graves C, Mogensen M. Production of synthetic fuels by co-electrolysis of steam and carbon dioxide. *International Journal of Green Energy*. 2009;6:646-60.
- [98] Menon V, Fu Q, Janardhanan VM, Deutschmann O. A model-based understanding of solid-oxide electrolysis cells (SOECs) for syngas production by H₂O/CO₂ co-electrolysis. *Journal of Power Sources*. 2015;274:768-81.

- [99] Li W, Shi Y, Luo Y, Cai N. Elementary reaction modeling of CO₂/H₂O co-electrolysis cell considering effects of cathode thickness. *Journal of Power Sources*. 2013;243:118-30.
- [100] Chen B, Xu H, Chen L, Li Y, Xia C, Ni M. Modelling of One-Step Methanation Process Combining SOECs and Fischer-Tropsch-like Reactor. *Journal of The Electrochemical Society*. 2016;163:F3001-F8.
- [101] Chen L, Chen F, Xia C. Direct synthesis of methane from CO₂-H₂O co-electrolysis in tubular solid oxide electrolysis cells. *Energy & Environmental Science*. 2014;7:4018-22.
- [102] Wang Y, Liu T, Lei L, Chen F. High temperature solid oxide H₂O/CO₂ co-electrolysis for syngas production. *Fuel Processing Technology*. 2017;161:248-58.
- [103] Lei L, Liu T, Fang S, Lemmon JP, Chen F. The co-electrolysis of CO₂-H₂O to methane via a novel micro-tubular electrochemical reactor. *Journal of Materials Chemistry A*. 2017;5:2904-10.
- [104] Liu T, Wang Y, Zhang Y, Fang S, Lei L, Ren C, et al. Steam electrolysis in a solid oxide electrolysis cell fabricated by the phase-inversion tape casting method. *Electrochemistry Communications*. 2015;61:106-9.
- [105] Yang X, Irvine JT. (La_{0.75} Sr_{0.25})_{0.95} Mn_{0.5} Cr_{0.5} O₃ as the cathode of solid oxide electrolysis cells for high temperature hydrogen production from steam. *Journal of Materials Chemistry*. 2008;18:2349-54.
- [106] Matsui T, Kishida R, Kim J-Y, Muroyama H, Eguchi K. Performance deterioration of Ni-YSZ anode induced by electrochemically generated steam in solid oxide fuel cells. *Journal of The Electrochemical Society*. 2010;157:B776-B81.

- [107] Fabbri E, Pergolesi D, Traversa E. Electrode materials: a challenge for the exploitation of protonic solid oxide fuel cells. *Science and technology of advanced materials*. 2010;11:044301.
- [108] Wachsman ED, Lee KT. Lowering the temperature of solid oxide fuel cells. *Science*. 2011;334:935-9.
- [109] Bi L, Boulfrad S, Traversa E. Reversible solid oxide fuel cells (R-SOFCs) with chemically stable proton-conducting oxides. *Solid State Ionics*. 2015;275:101-5.
- [110] Bi L, Fabbri E, Sun Z, Traversa E. Sinteractive anodic powders improve densification and electrochemical properties of BaZr_{0.8}Y_{0.2}O_{3-δ} electrolyte films for anode-supported solid oxide fuel cells. *Energy & Environmental Science*. 2011;4:1352-7.
- [111] Sun W, Yan L, Shi Z, Zhu Z, Liu W. Fabrication and performance of a proton-conducting solid oxide fuel cell based on a thin BaZr_{0.8}Y_{0.2}O_{3-δ} electrolyte membrane. *Journal of Power Sources*. 2010;195:4727-30.
- [112] Ricote S, Bonanos N, Manerbino A, Sullivan NP, Coors W. Effects of the fabrication process on the grain-boundary resistance in BaZr_{0.9}Y_{0.1}O_{3-δ}. *Journal of Materials Chemistry A*. 2014;2:16107-15.
- [113] Tong J, Clark D, Bernau L, Sanders M, O'Hayre R. Solid-state reactive sintering mechanism for large-grained yttrium-doped barium zirconate proton conducting ceramics. *Journal of Materials Chemistry*. 2010;20:6333.
- [114] Liu RR, Kim SH, Taniguchi S, Oshima T, Shiratori Y, Ito K, et al. Influence of water vapor on long-term performance and accelerated degradation of solid oxide fuel cell cathodes. *Journal of Power Sources*. 2011;196:7090-6.

- [115] Wang Y, Liu T, Fang S, Xiao G, Wang H, Chen F. A novel clean and effective syngas production system based on partial oxidation of methane assisted solid oxide co-electrolysis process. *Journal of Power Sources*. 2015;277:261-7.
- [116] Fang S, Wang S, Brinkman KS, Chen F. A sinteractive Ni–BaZr_{0.8}Y_{0.2}O_{3–δ} composite membrane for hydrogen separation. *Journal of Materials Chemistry A*. 2014;2:5825.
- [117] Lei L, Bai Y, Liu J. Ni-based anode-supported Al₂O₃-doped-Y₂O₃-stabilized ZrO₂ thin electrolyte solid oxide fuel cells with Y₂O₃-stabilized ZrO₂ buffer layer. *Journal of Power Sources*. 2014;248:1312-9.
- [118] Lei L, Bai Y, Liu Y, Liu J. An Investigation on Dip-Coating Technique for Fabricating Anode-Supported Solid Oxide Fuel Cells. *International Journal of Applied Ceramic Technology*. 2013;12:351-7.
- [119] Lei L, Wang Y, Fang S, Ren C, Liu T, Chen F. Efficient syngas generation for electricity storage through carbon gasification assisted solid oxide co-electrolysis. *Applied Energy*. 2016;173:52-8.
- [120] Zhao F, Wang S, Brinkman K, Chen F. Layered perovskite PrBa_{0.5}Sr_{0.5}Co₂O_{5+δ} as high performance cathode for solid oxide fuel cells using oxide proton-conducting electrolyte. *Journal of Power Sources*. 2010;195:5468-73.
- [121] Wu T, Peng R, Xia C. Sm_{0.5}Sr_{0.5}CoO_{3–δ}–BaCe_{0.8}Sm_{0.2}O_{3–δ} composite cathodes for proton-conducting solid oxide fuel cells. *Solid State Ionics*. 2008;179:1505-8.
- [122] Xiao J, Sun W, Zhu Z, Tao Z, Liu W. Fabrication and characterization of anode-supported dense BaZr_{0.8}Y_{0.2}O_{3–δ} electrolyte membranes by a dip-coating process. *Materials Letters*. 2012;73:198-201.

- [123] Tao Z, Wang B, Hou G, Xu N. Preparation of $\text{BaZr}_{0.1}\text{Ce}_{0.7}\text{Y}_{0.2}\text{O}_{3-\delta}$ thin membrane based on a novel method-drop coating. *International Journal of Hydrogen Energy*. 2014;39:16020-4.
- [124] Tong J, Clark D, Hoban M, O'Hayre R. Cost-effective solid-state reactive sintering method for high conductivity proton conducting yttrium-doped barium zirconium ceramics. *Solid State Ionics*. 2010;181:496-503.
- [125] Ricote S, Bonanos N, Manerbino A, Coors W. Conductivity study of dense $\text{BaCe}_x\text{Zr}_{(0.9-x)}\text{Y}_{0.1}\text{O}_{(3-\delta)}$ prepared by solid state reactive sintering at 1500 C. *International Journal of Hydrogen Energy*. 2012;37:7954-61.
- [126] Stuart PA, Unno T, Kilner JA, Skinner SJ. Solid oxide proton conducting steam electrolyzers. *Solid State Ionics*. 2008;179:1120-4.
- [127] Bae H, Choi J, Kim KJ, Park D, Choi GM. Low-temperature fabrication of protonic ceramic fuel cells with $\text{BaZr}_{0.8}\text{Y}_{0.2}\text{O}_{3-\delta}$ electrolytes coated by aerosol deposition method. *International Journal of Hydrogen Energy*. 2015;40:2775-84.
- [128] Bi L, Fabbri E, Sun Z, Traversa E. Sinteractive anodic powders improve densification and electrochemical properties of $\text{BaZr}_{0.8}\text{Y}_{0.2}\text{O}_{3-\delta}$ electrolyte films for anode-supported solid oxide fuel cells. *Energy & Environmental Science*. 2011;4:1352.
- [129] Iwahara H, Uchida H, Yamasaki I. High-temperature steam electrolysis using SrCeO_3 -based proton conductive solid electrolyte. *International Journal of Hydrogen Energy*. 1987;12:73-7.
- [130] Iwahara H, Uchida H, Maeda N. High temperature fuel and steam electrolysis cells using proton conductive solid electrolytes. *Journal of Power Sources*. 1982;7:293-301.

- [131] Iwahara H, Esaka T, Uchida H, Maeda N. Proton conduction in sintered oxides and its application to steam electrolysis for hydrogen production. *Solid State Ionics*. 1981;3:359-63.
- [132] Stuart PA, Unno T, Kilner JA, Skinner SJ. Solid oxide proton conducting steam electrolyzers. *Solid State Ionics*. 2008;179:1120-4.
- [133] He F, Song D, Peng R, Meng G, Yang S. Electrode performance and analysis of reversible solid oxide fuel cells with proton conducting electrolyte of $\text{BaCe}_{0.5}\text{Zr}_{0.3}\text{Y}_{0.2}\text{O}_{3-\delta}$. *Journal of Power Sources*. 2010;195:3359-64.
- [134] Azimova MA, McIntosh S. On the reversibility of anode supported proton conducting solid oxide cells. *Solid State Ionics*. 2011;203:57-61.
- [135] Li S, Xie K. Composite Oxygen Electrode Based on LSCF and BSCF for Steam Electrolysis in a Proton-Conducting Solid Oxide Electrolyzer. *Journal of the Electrochemical Society*. 2013;160:F224-F33.
- [136] Sutija DP, Norby T, Björnbom P. Transport number determination by the concentration-cell/open-circuit voltage method for oxides with mixed electronic, ionic and protonic conductivity. *Solid State Ionics*. 1995;77:167-74.
- [137] Minh NQ. Solid oxide fuel cell technology—features and applications. *Solid State Ionics*. 2004;174:271-7.
- [138] Gao Z, Mogni LV, Miller EC, Railsback JG, Barnett SA. A perspective on low-temperature solid oxide fuel cells. *Energy Environ Sci*. 2016;9:1602-44.
- [139] Chen Y, Lin Y, Zhang Y, Wang S, Su D, Yang Z, et al. Low temperature solid oxide fuel cells with hierarchically porous cathode nano-network. *Nano Energy*. 2014;8:25-33.

- [140] Chen Y, Zhang Y, Baker J, Majumdar P, Yang Z, Han M, et al. Hierarchically Oriented Macroporous Anode-Supported Solid Oxide Fuel Cell with Thin Ceria Electrolyte Film. *ACS Applied Materials & Interfaces*. 2014;6:5130-6.
- [141] Singh B, Ghosh S, Aich S, Roy B. Low temperature solid oxide electrolytes (LT-SOE): A review. *Journal of Power Sources*. 2017;339:103-35.
- [142] Fabbri E, Bi L, Pergolesi D, Traversa E. Towards the next generation of solid oxide fuel cells operating below 600 degrees c with chemically stable proton-conducting electrolytes. *Advance Materials*. 2012;24:195-208.
- [143] Li M, Hua B, Luo J-l, Jiang SP, Pu J, Chi B, et al. Carbon-tolerant Ni-based cermet anodes modified by proton conducting yttrium- and ytterbium-doped barium cerates for direct methane solid oxide fuel cells. *Journal of Materials Chemistry A*. 2015;3:21609-17.
- [144] Zhao L, Li G, Chen K, Ling Y, Cui Y, Gui L, et al. $\text{Sm}_{0.5}\text{Sr}_{0.5}\text{CoO}_{3-\delta}$ infiltrated $\text{Ce}_{0.9}\text{Gd}_{0.1}\text{O}_{2-\delta}$ composite cathodes for high performance protonic ceramic fuel cells. *Journal of Power Sources*. 2016;333:24-9.
- [145] Li G, Jin H, Cui Y, Gui L, He B, Zhao L. Application of a novel $(\text{Pr}_{0.9}\text{La}_{0.1})_2(\text{Ni}_{0.74}\text{Cu}_{0.21}\text{Nb}_{0.05})\text{O}_{4+\delta}$ -infiltrated $\text{BaZr}_{0.1}\text{Ce}_{0.7}\text{Y}_{0.2}\text{O}_{3-\delta}$ cathode for high performance protonic ceramic fuel cells. *Journal of Power Sources*. 2017;341:192-8.
- [146] Tao SW, Irvine JTS. A Stable, Easily Sintered Proton- Conducting Oxide Electrolyte for Moderate-Temperature Fuel Cells and Electrolyzers. *Advanced Materials*. 2006;18:1581-4.
- [147] Yamazaki Y, Hernandez-Sanchez R, Haile SM. High Total Proton Conductivity in Large-Grained Yttrium-Doped Barium Zirconate. *Chemistry of Materials*. 2009;21:2755-62.

- [148] Pergolesi D, Fabbri E, D'Epifanio A, Di Bartolomeo E, Tebano A, Sanna S, et al. High proton conduction in grain-boundary-free yttrium-doped barium zirconate films grown by pulsed laser deposition. *Nature Materials*. 2010;9:846-52.
- [149] Bi L, Shafi SP, Traversa E. Y-doped BaZrO₃ as a chemically stable electrolyte for proton-conducting solid oxide electrolysis cells (SOECs). *Journal of Materials Chemistry A*. 2015;3:5815-9.
- [150] Shang M, Tong J, O'Hayre R. A promising cathode for intermediate temperature protonic ceramic fuel cells: BaCo_{0.4}Fe_{0.4}Zr_{0.2}O_{3-δ}. *RSC Advances*. 2013;3:15769.
- [151] Liu Y, Chen K, Zhao L, Chi B, Pu J, Jiang SP, et al. Performance stability and degradation mechanism of La_{0.6}Sr_{0.4}Co_{0.2}Fe_{0.8}O_{3-δ} cathodes under solid oxide fuel cells operation conditions. *International Journal of Hydrogen Energy*. 2014;39:15868-76.
- [152] Li G, He B, Ling Y, Xu J, Zhao L. Highly active YSB infiltrated LSCF cathode for proton conducting solid oxide fuel cells. *International Journal of Hydrogen Energy*. 2015;40:13576-82.
- [153] Pergolesi D, Fabbri E, Traversa E. Chemically stable anode-supported solid oxide fuel cells based on Y-doped barium zirconate thin films having improved performance. *Electrochemistry Communications*. 2010;12:977-80.
- [154] Ding D, Li X, Lai SY, Gerdes K, Liu M. Enhancing SOFC cathode performance by surface modification through infiltration. *Energy & Environmental Science*. 2014;7:552-75.
- [155] Ding D, Liu M, Liu Z, Li X, Blinn K, Zhu X, et al. Efficient Electro-Catalysts for Enhancing Surface Activity and Stability of SOFC Cathodes. *Advanced Energy Materials*. 2013;3:1149-54.

- [156] Chen Y, Chen Y, Ding D, Ding Y, Choi Y, Zhang L, et al. A robust and active hybrid catalyst for facile oxygen reduction in solid oxide fuel cells. *Energy & Environmental Science*. 2017;10:964-71.
- [157] Peng R, Wu T, Liu W, Liu X, Meng G. Cathode processes and materials for solid oxide fuel cells with proton conductors as electrolytes. *Journal of Materials Chemistry*. 2010;20:6218.
- [158] Zhao L, He B, Gu J, Liu F, Chu X, Xia C. Reaction model for cathodes cooperated with oxygen-ion conductors for solid oxide fuel cells using proton-conducting electrolytes. *International Journal of Hydrogen Energy*. 2012;37:548-54.
- [159] Zhou G, Fu X, Luo J, Chuang K, Sanger A. Ag modified LSCF as cathode material for protonic conducting SOFCs. *Materials Technology*. 2013;28:3-8.
- [160] He B, Zhang L, Zhang Y, Ding D, Xu J, Ling Y, et al. New insight into highly active cathode of proton conducting solid oxide fuel cells by oxygen ionic conductor modification. *Journal of Power Sources*. 2015;287:170-6.
- [161] Xiao J, Sun W, Zhu Z, Tao Z, Liu W. Fabrication and characterization of anode-supported dense $\text{BaZr}_{0.8}\text{Y}_{0.2}\text{O}_{3-\delta}$ electrolyte membranes by a dip-coating process. *Materials Letters*. 2012;73:198-201.
- [162] Lei L, Tao Z, Wang X, Lemmon JP, Chen F. Intermediate-temperature solid oxide electrolysis cells with thin proton-conducting electrolyte and a robust air electrode. *Journal of Materials Chemistry A*. 2017;5:22945-51.
- [163] Hou J, Qian J, Bi L, Gong Z, Peng R, Liu W. The effect of oxygen transfer mechanism on the cathode performance based on proton-conducting solid oxide fuel cells. *Journal of Materials Chemistry A*. 2015;3:2207-15.

- [164] Zhu Z, Sun W, Shi Z, Liu W. Proton-conducting solid oxide fuel cells with yttrium-doped barium zirconate electrolyte films sintered at reduced temperatures. *Journal of Alloys and Compounds*. 2016;658:716-20.
- [165] Bi L, Fabbri E, Sun Z, Traversa E. A novel ionic diffusion strategy to fabricate high-performance anode-supported solid oxide fuel cells (SOFCs) with proton-conducting Y-doped BaZrO₃ films. *Energy Environ Sci*. 2011;4:409-12.
- [166] Joh DW, Park JH, Kim D, Wachsman ED, Lee KT. Functionally Graded Bismuth Oxide/Zirconia Bilayer Electrolytes for High-Performance Intermediate-Temperature Solid Oxide Fuel Cells (IT-SOFCs). *ACS Applied Materials & Interfaces*. 2017;9:8443-9.
- [167] Li M, Zhou W, Zhu Z. Highly CO₂-Tolerant Cathode for Intermediate-Temperature Solid Oxide Fuel Cells: Samarium-Doped Ceria-Protected SrCo_{0.85}Ta_{0.15}O_{3-δ} Hybrid. *ACS Applied Materials & Interfaces*. 2017;9:2326-33.
- [168] Zhao J, Xu X, Zhou W, Blakey I, Liu S, Zhu Z. Proton-Conducting La-Doped Ceria-Based Internal Reforming Layer for Direct Methane Solid Oxide Fuel Cells. *ACS Applied Materials & Interfaces*. 2017;9:33758-65.
- [169] Mah JCW, Muchtar A, Somalu MR, Ghazali MJ. Metallic interconnects for solid oxide fuel cell: A review on protective coating and deposition techniques. *International Journal of Hydrogen Energy*. 2017;42:9219-29.
- [170] Yang Z, Guo M, Wang N, Ma C, Wang J, Han M. A short review of cathode poisoning and corrosion in solid oxide fuel cell. *International Journal of Hydrogen Energy*. 2017;42:24948-59.
- [171] Jiang SP, Zhen Y. Mechanism of Cr deposition and its application in the development of Cr-tolerant cathodes of solid oxide fuel cells. *Solid State Ionics*. 2008;179:1459-64.

- [172] Zhen Y, Jiang SP. Characterization and performance of (La,Ba)(Co,Fe)O₃ cathode for solid oxide fuel cells with iron–chromium metallic interconnect. *Journal of Power Sources*. 2008;180:695-703.
- [173] Kim Y-M, Chen X, Jiang SP, Bae J. Chromium Deposition and Poisoning at Ba_{0.5}Sr_{0.5}Co_{0.8}Fe_{0.2}O_{3-δ} Cathode of Solid Oxide Fuel Cells. *Electrochemical and Solid-State Letters*. 2011;14:B41-B5.
- [174] Komatsu T, Arai H, Chiba R, Nozawa K, Arakawa M, Sato K. Long-Term Chemical Stability of LaNi(Fe)O₃ as a Cathode Material in Solid Oxide Fuel Cells. *Journal of The Electrochemical Society*. 2007;154:B379.
- [175] Chen K, Ai N, O'Donnell KM, Jiang SP. Highly chromium contaminant tolerant BaO infiltrated La_{0.6}Sr_{0.4}Co_{0.2}Fe_{0.8}O_{3-δ} cathodes for solid oxide fuel cells. *Physical chemistry chemical physics : PCCP*. 2015;17:4870-4.
- [176] Shen F, Lu K. Co₃O₄/Sm-Doped CeO₂/Co₃O₄ Trilayer Coating on AISI 441 Interconnect for Solid Oxide Fuel Cells. *ACS Applied Materials & Interfaces*. 2017;9:6022-9.
- [177] Uddin MA, Banas CJ, Liang C, Pasaogullari U, Recknagle KP, Koeppel BJ, et al. Design and Optimization of Chromium Getter for SOFC Systems through Computational Modeling. *ECS Transactions*. 2017;78:1063-72.
- [178] Li Y, Hu B, Xia C, Xu WQ, Lemmon JP, Chen F. A novel fuel electrode enabling direct CO₂ electrolysis with excellent and stable cell performance. *Journal of Materials Chemistry A*. 2017;5:20833-42.

- [179] Li Y, Zhang W, Zheng Y, Chen J, Yu B, Chen Y, et al. Controlling cation segregation in perovskite-based electrodes for high electro-catalytic activity and durability. *Chem Soc Rev.* 2017;46:6345-78.
- [180] Wei B, Chen K, Zhao L, Lu Z, Jiang SP. Chromium deposition and poisoning at $\text{La}_{0.6}\text{Sr}_{0.4}\text{Co}_{0.2}\text{Fe}_{0.8}\text{O}_{(3-\delta)}$ oxygen electrodes of solid oxide electrolysis cells. *Physical chemistry chemical physics : PCCP.* 2015;17:1601-9.
- [181] Fu C, Sun K, Zhang N, Chen X, Zhou D. Electrochemical characteristics of LSCF–SDC composite cathode for intermediate temperature SOFC. *Electrochimica Acta.* 2007;52:4589-94.
- [182] Grunbaum N, Dessemond L, Fouletier J, Prado F, Mogni L, Caneiro A. Rate limiting steps of the porous $\text{La}_{0.6}\text{Sr}_{0.4}\text{Co}_{0.8}\text{Fe}_{0.2}\text{O}_{3-\delta}$ electrode material. *Solid State Ionics.* 2009;180:1448-52.
- [183] Lee SN, Atkinson A, Kilner JA. Effect of chromium on $\text{La}_{0.6}\text{Sr}_{0.4}\text{Co}_{0.2}\text{Fe}_{0.8}\text{O}_3$ - solid oxide fuel Cell cathodes. *Journal of the Electrochemical Society.* 2013;160:F629-F35.
- [184] Baghni IM, Lyon SB, Ding B. The effect of strontium and chromate ions on the inhibition of zinc. *Surface and Coatings Technology.* 2004;185:194-8.